Tampere University

IFTE KHAIRUL ALAM BHUIYAN

Broadband Superluminescent Diodes at 2 µm Wavelength Range for Optical Coherence Tomography

Tampere University Dissertations 1539

Tampere University Dissertations 1539

IFTE KHAIRUL ALAM BHUIYAN

Broadband Superluminescent Diodes at 2 μm Wavelength Range for Optical Coherence Tomography

ACADEMIC DISSERTATION
To be presented, with the permission of
the Faculty of Engineering and Natural Sciences
of Tampere University,
for public discussion in the auditorium TB109
of the Tietotalo, Korkeakoulunkatu 1, Tampere,
on 05 June 2026, at 12 o'clock.

ACADEMIC DISSERTATION
Tampere University, Faculty of Engineering and Natural Sciences
Finland

Responsible supervisor and Custos	Professor Mircea Guina Tampere University Finland	
Supervisor	Associate Professor Jukka Viheriälä Tampere University Finland	
Pre-examiners	Professor Edik Rafailov Aston University United Kingdom	Professor Tapio Fabritius University of Oulu Finland
Opponent	Professor Tapio Fabritius University of Oulu Finland	

The originality of this thesis has been checked using the Turnitin Originality service.

Copyright ©2026 Ifte Khairul Alam Bhuiyan

Cover design: Roihu Inc.

ISBN 978-952-03-4644-7 (print)
ISBN 978-952-03-4645-4 (pdf)
ISSN 2489-9860 (print)
ISSN 2490-0028 (pdf)
http://urn.fi/URN:ISBN:978-952-03-4645-4

PunaMusta Oy – Yliopistopaino
Joensuu 2026

The dissertation is dedicated to my beloved family: my wife, my sons Muhammad and Ahmad, my mother, and to the memory of my father—whose unwavering support and encouragement made this journey possible.

ACKNOWLEDGEMENTS

The research presented in this doctoral dissertation was carried out at the Optoelectronics Research Centre (ORC), Tampere University, Finland. The work was financially supported by the European Commission under the Horizon 2020 program through the project Next Generation of Tunable Lasers for Optical Coherence Tomography (NETLAS, #860807) and Horizon Europe project PhotonMed (#101139777-2), Business Finland (#8294/31/2023) as well as by the Flagship Programme on Photonics Research and Innovation (PREIN, #320168) funded by the Research Council of Finland. Their generous support is gratefully acknowledged.

I would like to express my deepest gratitude to my supervisor, Professor Mircea Guina, for his exceptional guidance, trust, and constant encouragement throughout this journey. His scientific vision and tireless dedication to advancing GaSb-based semiconductor research at ORC have been truly inspiring. It has been a privilege to work under his supervision and to contribute to his group's pioneering efforts in mid-infrared optoelectronics.

I wish to express my heartfelt gratitude to Dr. Jukka Viheriälä for his invaluable mentoring, and encouragement throughout the project. He played a key role in integrating me into the laboratory environment at ORC and continuously guided me through device design, measurements, and project planning. His calm approach, constructive feedback, and genuine support had a strong influence on both the quality of this research and my personal development.

My sincere appreciation goes to Dr. Heidi Tuorila, who first introduced me to the fundamentals of semiconductor wafer processing and ensured that I learned to work safely and confidently in the cleanroom. I am deeply thankful to Ms. Mervi Koskinen for her patience, precision, and extensive technical knowledge in advanced III–V device processing (GaSb, GaAs). Her consistent support helped me develop confidence and independence in cleanroom fabrication.

I would also like to thank Dr. Joonas Hilska, with whom I spent many hours of quality discussion on scientific problems, experimental results, and journal reviews. His deep technical understanding, and willingness to engage in thoughtful discussions greatly enhanced my knowledge. I truly appreciate his support, patience, and the time he devoted to helping me refine ideas and interpret complex results.

I am grateful to Dr. Teemu Hakkarainen for his approachable nature and the insightful conversations we shared on various scientific topics. My thanks to Dr. Topi Uusitalo, whose expertise in theory and simulation strengthened the analytical foundation of this work. I am especially thankful to Dr. Nouman Zia, who taught me my first measurement techniques for *L–I–V* characterization, spectral analysis, and fiber-coupling methods and whose guidance was instrumental during the early stages of experimentation. I also wish to thank Dr. Samu Pekka Ojanen for his valuable help in optical measurements and data acquisition, and Dr. Heikki Virtanen and Dr. Marika Janka for their technical assistance in anti-reflection and high-reflection coating design, which became essential to the success of this work. My sincere appreciation also goes to Markus Peil, a good friend and collaborator, for his insightful discussions on epitaxial structure design. Both, Dr. Joonas and Markus have deep expertise in epitaxial growth and materials optimization contributed significantly to refining the active structures used in this thesis. I also thank to my supportive colleague and friends Dr. Abhiroop, Dr. Philipp, Dr. Hermann, Behzad Namvar, and Helmer Piirilä, whose encouragement, and positive attitude have always been valuable.

I am indebted to all my colleagues and friends at the Optoelectronics Research Centre (ORC) for creating a stimulating and collaborative research environment. The culture of openness, knowledge-sharing, and teamwork within the group made the research process both productive and enjoyable.

Special thanks go to my collaborators at the Applied Optics Group (AOG) in University of Kent, led by Professor Adrian Podoleanu, where I conducted part of this work during my research secondment. Their cooperation and enthusiasm during the integration of the GaSb-based SLDs into an OCT system in validating the results at the system level and expanding the practical reach of this research.

Finally, I express my deepest gratitude to my family. My parents have always believed in the transformative power of education. My heartfelt thanks go to my wife, for her patience, strength, and unwavering support during the most demanding phases of my doctoral studies, and to my sons, whose joy, warmth, and laughter constantly supported me in making balance in this journey. Their love and encouragement always gave me the energy to keep moving forward.

Tampere, April 2026
Ifte Khairul Alam Bhuiyan

ABSTRACT

Optical coherence tomography (OCT) is widely known as a non-invasive optical imaging modality. OCT has made a lasting impact in the field of biomedical diagnostics and is increasingly pursued as an investigation tool for non-biomedical applications, a transition often linked to operation at new wavelength regions. To this end, this doctoral dissertation presents a comprehensive investigation into the design, fabrication, and characterization of broadband gallium antimonide (GaSb)–based superluminescent diodes (SLDs) operating at the 2 μm wavelength band, specifically tailored for OCT. From a broader perspective, the research addresses the growing demand for GaSb-based light sources operating in the short-wave infrared (SWIR) and mid-infrared (mid-IR) range.

The motivation for this work originates from the advantages of OCT imaging at longer wavelengths, where optical scattering is significantly reduced and imaging depth and contrast are improved, particularly in samples with low water content or high refractive indices. Compared to state-of-the-art OCT at longer wavelengths relying on expensive and bulky supercontinuum sources, GaSb-based semiconductor light sources are compact and cost-effective, enabling a larger penetration of OCT technology to new applications.

This thesis introduces a new design strategy based on dimensionally asymmetric quantum wells (QWs) in GaSb-based heterostructures to achieve record-broadband amplified spontaneous emission (ASE) in 2.0 μm wavelength window with high optical power and smooth spectral profiles. Such broadband low coherence sources were employed to perform time-domain OCT imaging. Beyond demonstrating a practical light source, this work advances the understanding of gain engineering in mid-IR III–V semiconductors. It shows that broadband gain can be realized purely through QW thickness and strain optimization, avoiding compositional inhomogeneity and simplifying epitaxial growth for reproducible manufacturing.

The research validates GaSb as a scalable platform for next-generation broadband emitters and amplifiers operating at the 2–3 μm wavelength region, enabling compact and high-performance light sources for OCT, spectroscopy, environmental sensing, and free-space communication.

TIIVISTELMÄ

Optinen koherenssitomografia (OCT) tunnetaan laajasti ei-invasiivisena optisena kuvantamismenetelmänä. OCT on vaikuttanut merkittävästi biolääketieteellisen diagnostiikan alalla, ja sitä hyödynnetään yhä enemmän tutkimustyökaluna myös ei-biolääketieteellisissä sovelluksissa, joissa tarvitaan uusia toiminta-aallonpituuksia. Tässä väitöskirjassa esitetään kattava tutkimus galliumantimonidiin (GaSb) perustuvien laajakaistaisten superluminesenssidiodien (SLD) suunnittelusta, valmistuksesta ja karakterisoinnista 2 µm aallonpituusalueella erityisesti OCT-kuvantamista varten. Laajemmasta näkökulmasta tutkimus vastaa kasvavaan tarpeeseen kehittää GaSb-pohjaisia valonlähteitä, jotka toimivat lyhytaaltoisen infrapunan (SWIR) ja keski-infrapunan (mid-IR) alueilla.

Tämän työn motivaationa ovat OCT-kuvantamisen edut pidemmillä aallonpituuksilla, joilla optinen sironta vähenee merkittävästi ja kuvantamissyvyys sekä kontrasti paranevat, erityisesti näytteissä, joissa on alhainen vesipitoisuus tai korkea taitekerroin. Verrattuna pidemmillä aallonpituuksilla toimiviin nykyisiin huipputason OCT-järjestelmiin, jotka perustuvat kalliisiin ja tilaa vieviin superjatkumolähteisiin, GaSb-pohjaiset puolijohdevalonlähteet ovat kompakteja ja kustannustehokkaita, mahdollistaen OCT-teknologian laajemman käyttöönoton uusissa sovelluksissa.

Tässä väitöskirjassa esitellään uusi suunnittelustrategia, joka perustuu mitoiltaan epäsymmetrisiin kvanttikaivoihin (QW) GaSb-pohjaisissa heterorakenteissa. Strategian avulla saavutetaan ennätyksellisen laajakaistainen vahvistettu spontaani emissio (ASE) 2.0 µm aallonpituusikkunassa, samalla kun optinen teho on korkea ja spektriprofiilit tasaisia. Tällaisia laajakaistaisia matalan koherenssin valonlähteitä käytettiin aikatasossa toimivan OCT-kuvantamisen toteuttamiseen. Käytännöllisen valonlähteen esittämisen lisäksi työ syventää ymmärrystä optisen vahvistuksen suunnittelusta keski-infrapunan III–V-puolijohteissa. Työssä osoitetaan, että laajakaistainen vahvistus voidaan saavuttaa pelkästään kvanttikaivojen paksuuden ja jännityksen optimoinnilla ilman koostumuksellista epähomogeenisuutta, mikä yksinkertaistaa epitaksiaalista kasvatusprosessia ja näin mahdollistaa toistettavan valmistuksen.

Tutkimus vahvistaa GaSb:in skaalautuvaksi alustaksi seuraavan sukupolven laajakaistaisille valonlähettimille ja vahvistimille 2–3 µm aallonpituusalueella, mahdollistaen kompaktit ja korkean suorituskyvyn valonlähteet OCT-kuvantamiseen, spektroskopiaan, ympäristön seurantaan sekä vapaassa tilassa tapahtuvaan tiedonsiirtoon.

CONTENTS

Acknowledgements v

Abstract vii

Tiivistelmä viii

Contents xi

Symbols and Abbreviations xiii

Original Publications xvii

Author's contributions xviii

1 Introduction 21
- 1.1 Background and motivation 21
- 1.2 Optical bandwidth requirements for OCT at 2 μm 24
- 1.3 Research objectives and questions 28
- 1.4 Thesis Structure 29

2 Theoretical background 31
- 2.1 OCT – basic concepts 31
  - 2.1.1 Time-domain OCT (TD-OCT) 32
  - 2.1.2 Fourier-domain OCT (FD-OCT) 34
- 2.2 Superluminescent diode (SLD) 36
  - 2.2.1 Basic operation principles 36
  - 2.2.2 Waveguide design considerations 39
- 2.3 Bandgap engineering in GaSb heterostructure 40

3 Methodology 44
- 3.1 Design approach for GaSb-based broadband heterostructures 44
  - 3.1.1 Validation of "Harold model" simulation 47
  - 3.1.2 Lateral waveguide design of SLD device architecture 48
- 3.2 Fabrication and processing 49
  - 3.2.1 Epitaxial growth 49

3.2.2 SLD device processing 51
3.3 SLD device characterization 54
3.4 SLD integration into a fiber-based interferometer for time-domain OCT imaging 55

4 Summary of Results 59
4.1 Power scaling of GaSb-based SLDs operating at 2 μm 59
4.2 Broadband heterostructures and amplifier devices in 2 μm wavelength with asymmetric quantum wells 66
4.2.1 Broadband SLD emitter using asymmetric double QWs 66
4.2.2 Design of broadband gain in heterostructures using asymmetric multiple QWs 70
4.3 Time-domain OCT imaging using 2 μm GaSb SLDs 75

5 Conclusions and future work 80

6 References 85

SYMBOLS AND ABBREVIATIONS

α	Internal optical loss coefficient [cm^{-1}]
β	Spontaneous emission coupling factor
ε	Dielectric permittivity [F m^{-1}]
η	Quantum efficiency
λ	Wavelength [nm, μm]
$\Delta\lambda$	Spectral bandwidth (FWHM) [nm]
τ	Carrier lifetime (generic) [s]
τ_{e}	Electron lifetime (SRH recombination) [s]
τ_{h}	Hole lifetime (SRH recombination) [s]
τ_{intra}	Intra-band relaxation time [s]
τ_{cap}	Carrier capture time constant [s]
τ_{esc}	Carrier escape time constant [s]
Φ	Photon flux [s^{-1} cm^{-2}]
ψ	Optical mode field distribution
A_{ij}	Dipole moment enhancement factor
c	Speed of light in vacuum [m s^{-1}]
d_{QW}	Quantum well thickness [nm]
E	Energy / photon energy [eV]
E_c, E_v	Conduction and valence band edges [eV]
f_e, f_h	Fermi occupation factors for electrons/holes
$g(E)$	Material gain spectrum [cm^{-1}]
h	Planck constant [J s]
I	Injection current [A]
J	Current density [A cm^{-2}]
k	Boltzmann constant [J K^{-1}]
K_{ij}	Overlap integral of optical transition
L	Device cavity length [μm or mm]

L_c	Coherence length [µm or mm]
m_e, m_h	Effective electron and hole mass [kg]
n	Refractive index
N	Carrier density [cm^{-3}]
q	Elementary charge [C]
R	Facet reflectivity [%]
R_{sp}	Spontaneous emission rate [s^{-1} cm^{-3}]
T	Temperature [K]
V	Voltage [V]
w	Ridge width / waveguide width [µm]
Γ	Quantum well confinement factor
AR	Anti-reflection coating
ASE	Amplified spontaneous emission
CW	Continuous wave
QW	Quantum well
SQW	Single quantum Well
DQW	Double quantum Well
MQW	Multiple quantum Well
FD-OCT	Fourier domain optical coherence tomography
SD-OCT	Spectral domain optical coherence tomography
SS-OCT	Swept source optical coherence tomography
FF-OCT	Full-field optical coherence tomography
FF	Far-field
FP	Fabry–Pérot
FWHM	Full width at half maximum
GaSb	Gallium antimonide
HR	High-reflection coating
IBS	Ion beam sputtering
ICP	Inductively coupled plasma
LD	Laser diode
L-I-V	Light(*L*)-Current(*I*)-Voltage(*V*)
mid-IR	Mid-infrared
MBE	Molecular beam epitaxy
OCT	Optical coherence tomography

PR	Photoresist
PL	Photoluminescence
PECVD	Plasma-enhanced chemical vapor deposition
RIE	Reactive ion etching
RSOA	Reflective semiconductor optical amplifier
RTA	Rapid thermal annealing
RWG	Ridge waveguide
SLD	Superluminescent diode
SWIR	Short-wave infrared
TD-OCT	Time-domain optical coherence tomography

ORIGINAL PUBLICATIONS

Publication I **I. K. A. Bhuiyan**, J. Hilska, M. Peil, J. Viheriälä, M. Guina, “Broadband continuous-wave GaSb-based superluminescent diodes emitting at 2.1 μm,” AIP Advances, 15 (8), 085015 (2025).

Publication II **I. K. A. Bhuiyan**, J. Hilska, M. Peil, J. Viheriälä, M. Guina, “Broadband 2-μm superluminescent diodes with GaSb-based variable-thickness quantum wells,” Applied Physics Letters, 127 (16), 163307 (2025).

Publication III **I. K. A. Bhuiyan**, J. Hilska, M. Peil, J. Viheriälä, M. Guina, “Design of broadband optical gain in GaSb-based heterostructures with asymmetric quantum wells,” Optics Express, 33 (26), 54154-54165 (2025).

Publication IV **I. K. A. Bhuiyan**, A. M. Jimenez, R. Cernat, A. F. Uceda, J. Hilska, M. Peil, M. Marques, G. Dobre, J. Viheriälä, A. Podoleanu, M. Guina, “Time-domain optical coherence tomography at 2 μm using GaSb-based broadband superluminescent diode,” Optics Express, 34 (10), 17833-17846 (2026).

AUTHOR'S CONTRIBUTIONS

The research works and outcomes obtained in this Doctoral thesis were obtained through collaborative work. The detailed contribution of the author is described below:

[P1] The author planned the epitaxial structure design together with Joonas Hilska, and Jukka Viheriälä. The epitaxial structure was grown and characterized by the authors Markus Peil and Joonas Hilska. Semiconductor process flow and mask design was provided by Heidi Tuorila and Jukka Viheriälä. The wafer processing and chip packaging was conducted by the author with the support from both Heidi Tuorila and Mervi Koskinen. Heikki Virtanen and Marika Janka supported in designing AR/HR coatings and ion beam sputtering (IBS) operation. The author performed the SLD device measurements. The author also analyzed the data together with Jukka Viheriälä. The author was responsible for writing the manuscript. Mircea Guina supervised the work and contributed to the manuscript writing process.

[P2] The author planned the epi-structure design and semiconductor process flow with Jukka Viheriälä. The epitaxial structure was grown using MBE by Markus Peil and Joonas Hilska. Semiconductor process flow and mask design was provided by Jukka Viheriälä. The wafer processing and chip packaging was conducted by the author. Marika Janka supported the ion beam sputtering (IBS) operation. The author processed the samples and mounted the chips. The author also built the experimental setup and conducted the characterization measurements. The author analyzed the characterization results with Jukka Viheriälä. The author was responsible for preparing the manuscript. Mircea Guina supervised the work and contributed to the manuscript writing process.

[P3] The author primarily planned the study and performed design and simulation of heterostructures for broadband gain with the guidance from Topi Uusitalo and Jukka Viheriälä. The validation process of the epi-structure was designed by the author. The epitaxial structure was grown and characterized by Markus Peil and Joonas Hilska. The semiconductor processing of the wafer was performed by the author with

guidance from Jukka Viheriälä. The author validated the simulation with the processed laser diode (LD) structure as well as calibrated the simulation and extended the design, and optimization using Harold multi-physics simulator (provided by Photon Design's license). The characterization results were analyzed together with Jukka Viheriälä. The author was responsible for preparing the manuscript. Joonas Hilska provided valuable discussion while preparing the manuscript. Mircea Guina supervised the work and coordinated the manuscript writing process.

[P4] The work was performed in collaboration with external partners. Together with Jukka Viheriälä, the author contributed in the semiconductor process flow and design geometry for making SLD chips that is compatible for Superlum's fiber coupled butterfly package. The wafer heterostructures were MBE grown by Joonas Hilska. The author performed the cleanroom semiconductor processing. The author also prepared AR/HR coatings with support from Marika Janka. The author was involved in chip packaging process with Superlum. The devices and SLD package were primarily characterized by the author with some guidance from Superlum. The Author built the interferometer setup for OCT measurement at the Applied Optics group (AOG) in the University of Kent, UK. Together with Alejandro Martinez, Ramona Carnet prepared samples and performed in OCT measurement. The experimental data were analyzed by the author with guidance from Alejandro Martinez, Manuel Marques and Adrian Podoleanu. The author wrote the manuscript under guidance from both Adrian Podoleanu and Mircea Guina.

1 INTRODUCTION

1.1 Background and motivation

Optical Coherence Tomography (OCT) is a widely recognized non-invasive imaging modality that employs non-ionizing radiation to enable high-resolution, cross-sectional visualization of biological or non-biological tissues. The technique has transformed the way diagnostic imaging is done since it was first introduced in the early 1990s [1]. It is now a standard technique for looking at the cornea and retina structures in ophthalmology [2]. OCT can also be utilized in cardiology [3], dermatology [4, 5], dentistry [6], pharmaceutical [7], and industrial inspection [8], providing non-invasive (for biological) or non-destructive (for non-biological materials) imaging with micrometer-scale resolution [9]. **Fig. 1** illustrates the most common imaging modalities to highlight the unique position of the OCT in terms of imaging resolution and penetration depth.

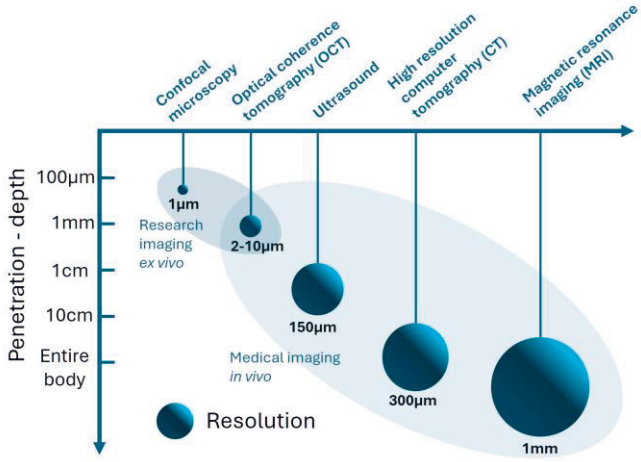


Figure 1. Comparison of OCT with other imaging modalities in terms of resolution and penetration depth; the "pendulum length" represents imaging depth, while the "sphere size" represents resolution (figure adapted from [10]).

In terms of depth and resolution, OCT offers an interesting trade-off: it can reach only a few millimeters beneath the surface, shallower than for example ultrasound,

high resolution computer tomography (CT), or magnetic resonance imaging (MRI), but with much finer detail. The situation is reversed when compared with confocal microscopy, which delivers better resolution but only very close to the surface.

Another strength of OCT is imaging speed (i.e. high acquisition speed) which enables near real-time cross-sectional imaging and can reduce sensitivity to sample motion compared to modalities that typically require longer acquisition time, such as in CT or MRI [11–13]. Moreover, unlike ultrasound, it does not require direct physical contact with the sample, and it can image in air-filled regions of the body. Then from a practical standpoint, OCT is closer in complexity to ultrasound than to CT or MRI, offering implementation possibilities in compact and cost-effective systems. Because technology can be implemented based on fibre optics, it also lends itself naturally to endoscopic and catheter-based applications, expanding its role in both research and clinical practice [14, 15]. Some of the state-of-the-art OCT imaging systems in different applications are shown in **Fig. 2**.

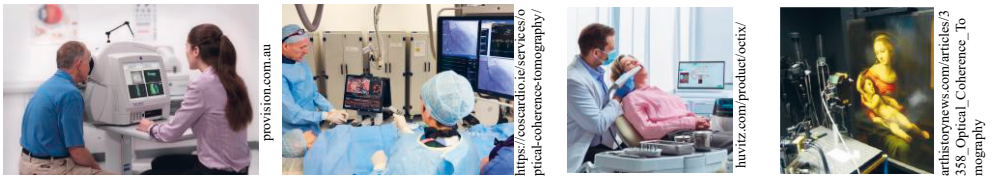


Figure 2. Exemplary applications of state-of-the-art OCT imaging systems in ophthalmology, cardiology, dentistry, and historical painting inspection.

Despite the system configuration, low-coherence interferometry is the primary concept behind OCT. Coherence length, central wavelength, and emission bandwidth of the light source set the imaging system's axial resolution. The coherence length and the spectral bandwidth of the source are connected in the opposite way and thus broadband light sources are instrumental for attaining good axial resolution in OCT devices. Then, to change the depth and contrast of an image, it is crucial to select the proper wavelength. Wavelengths that are shorter (i.e. 800 nm) provide good resolution, but they experience stronger scattering, leading to faster signal decay in tissues with depth [16]. Endoscopic and intravascular imaging modalities frequently use longer wavelengths (~1300–1550 nm) due to benefit from reduced scattering and therefore enable deeper penetration depth [17, 18].

In recent years, there has been more interest in expanding OCT to inspect nonbiological and industrial materials using 2 μm wavelength region [19–22]. One of the main reasons is that living tissues scatter less light at longer wavelengths,

allowing them to see deeper into the tissue. Moreover, water absorption is stronger around the 2 μm window, which makes contrast mechanisms work especially well for imaging tissues that are high in water, like blood vessels, cartilage, and muscle. On the other hand, development of OCT at 2 μm window has been scarce, only recently capturing a somewhat higher level of attention. For instance, 2 μm OCT shows potential in dental imaging, where better penetration is needed to discover cavities and other structural abnormalities. **Fig. 3** shows some of the recent OCT inspection practices in non-biological and industrial materials [23] at different wavelengths (from visible to mid-IR: ~850 nm [24–27], 930 nm [28, 29], 1260–1550 nm [30–35], 2000–4000 nm [36, 37]).

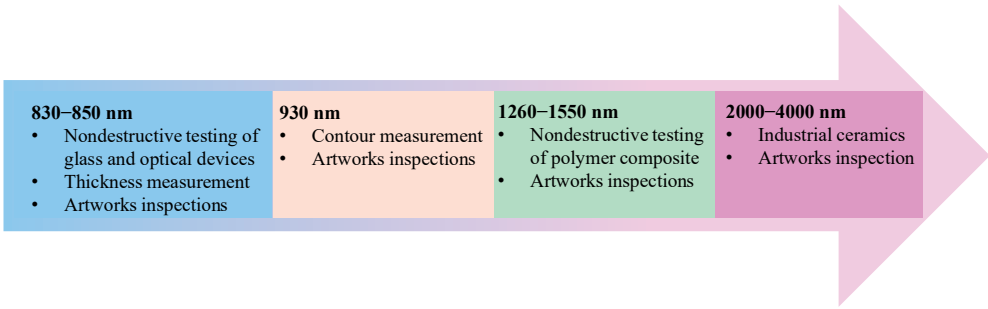


Figure 3. Visible to mid-IR OCT application in non-biological and industrial materials.

Even though 2 μm OCT has clear applications, concrete developments have been hampered by the lack of adequate light sources. Superluminescent diodes (SLDs) are particularly well-suited for OCT because they offer low coherence length, high enough power spectral density, stable spectral profiles, and are compact and cost-effective. The challenge lies in designing SLDs that can simultaneously achieve broad spectral bandwidth and sufficient output power, especially at longer wavelengths where material losses and thermal effects become significant. When it comes to the development of semiconductor-based light sources, InP and GaAs are the most established material platforms utilized to make SLDs and wavelength-swept laser sources [38]. These materials work well for generating light, for example, GaAs-based devices typically support emission from approximately 630 nm to ~1.2 μm [39, 40], while InP-based systems extend operation across the 1.1–2.4 μm [41, 42] spectral region.

Moving to 2 μm wavelength range and beyond has been addressed with GaSb-based optoelectronic compounds, which on the other hand is much less available as a technology platform. The GaSb material system offers access to a wide range of AlGaInAsSb alloys enabling bandgap and strain engineering of type-I quantum-well

(QW) hetero-structures with versatile emission in the 1.8–3.4 μm range [43–53]. Moreover, GaSb-based lasers have already demonstrated mid-infrared (mid-IR) applications, especially in spectroscopic sensing. However, the development of GaSb-based SLDs, the devices that combine the broadband nature of LEDs with the high brightness feature of laser diodes, remains relatively unexplored.

To this end, the thesis work aimed at the development of compact, efficient, and broadband GaSb-based SLDs operating around 2 μm, specifically designed for OCT applications. The objective was to overcome some of the constraints of existing light sources and investigate the capabilities of GaSb-based SLDs in improving OCT imaging system complexity, size and efficacy. This research was targeted to enhance short-wave and mid-infrared photonics and broaden the applications of OCT in industrial contexts by utilizing the distinctive characteristics of the GaSb material system.

This effort was motivated not only by scientific considerations advancing the development of GaSb-based optoelectronics technology, but also by an overarching application goal to demonstrate high-resolution imaging at 2 μm using OCT. Summarizing the motivation aspects, the doctoral research work was motivated by the convergence of three principal factors:

(i) the increasing demand for OCT imaging in nonbiological and industrial materials,
(ii) the constraints of current light sources in the 2 μm wavelength window,
(iii) the unexploited state of GaSb-based broadband light sources for OCT system.

The thesis addressed these deficiencies following a comprehensive approach starting with the designing of new SLD heterostructures, followed by advanced fabrication, characterization and ultimately demonstrating applicability in OCT imaging at 2 μm.

1.2 Optical bandwidth requirements for OCT at 2 μm

Before we summarize the research questions, let's generally discuss the background defying the main technical assumption impacting the definitions of the targets. The performance of an OCT system is intrinsically connected to the properties of its light source. Axial resolution is one of the most important factors that affect OCT image quality, and it is directly related to the coherence length of the source, which is

inversely related to its spectral bandwidth [16, 54]. For a light source with Gaussian spectrum, axial resolution Δz in a medium of refractive index n is defined as follows:

$$\Delta z = \frac{2ln2}{\pi} \cdot \frac{\lambda_0^2}{n \cdot \Delta\lambda} \quad (1)$$

where λ_0 represents the central wavelength and $\Delta\lambda$ is the FWHM spectral bandwidth of the source. This inverse relationship highlights the necessity of using broadband light sources to achieve higher axial resolution.

Fig. 4 illustrates the theoretical axial resolution in air medium for OCT sources centered at 2 μm as a function of spectral bandwidth (maximum $\Delta\lambda$ = 300 nm) based on equation (1) for refractive indices ranging from air (n = 1.0) to higher-index media (n = 3.0). The figure also showcases the degree of axial resolution for our intended OCT spectral range applicable for non-biological samples (denser media) such as paint-coatings, polymers, ceramics, or industrial materials where refractive index often ranges from ~1.3 to above ~2.5. The figure also shows an exponentially decayed trend where the axial resolution improves (i.e., Δz becomes smaller) with increasing spectral bandwidth. The axial resolution is further improved in higher refractive index media for the same bandwidth. For example, at a bandwidth of 100 nm, the axial resolution is ~18 μm in air, ~12 μm in n = 1.5 media, and ~6 μm in n = 3.0. This means that dense medium with higher refractive index "n" scales down with effective axial resolution ($\Delta z_n = \Delta z/n$).

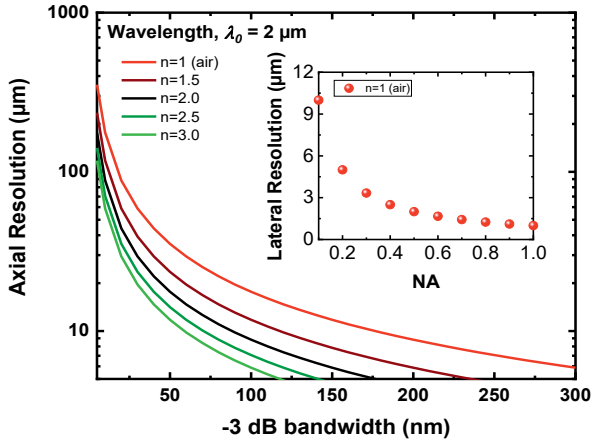


Figure 4. Theoretical axial resolution (μm) for 2 μm wavelength light sources for different FWHM media. Inset shows the lateral resolution (μm) of the in an OCT system for different numerical apertures (NA). Reproduced from [P4].

The lateral resolution of such optical system is determined by the focusing optics design as well as the operating wavelength, and can be approximated in the diffraction-limited case following Abbe criterion [55, 56]

$$r \approx \frac{\lambda_0}{2\, n \sin\theta} = \frac{\lambda_0}{2\, NA} \tag{2}$$

where r represents approximate lateral resolution limit rather than physical beam diameter, n is the refractive index of the media ($n = 1$, for simplicity), and θ is the half-angle of the focused light beam that enters the objective lens. The **Fig. 4** inset shows the dependence of lateral resolution on the numerical aperture ($NA = n\, Sin\theta$) of the focusing optics for operation at 2 μm wavelength. The lateral resolution improves with increasing NA at the expense of depth of focus (DOF) – the axial range over which the beam remains tightly focused, so a trade-off must be considered depending on the imaging requirements. For example, doubling NA improves the lateral resolution but the DOF is approximately four times reduced. At 2 μm wavelength, diffraction-limited DOF is larger than 1.3 μm for the same NA, however scattering media can still limit the useful imaging depth. Overall, **Fig. 4** predicts that broadband sources at 2 μm can achieve axial resolutions well below 10 μm in practical refractive index ranges, provided that a source with an emission bandwidth (>100 nm) is available.

Unlike biological tissues, where high water content dominates absorption at 2 μm and limits penetration, synthetic materials generally contain little to no water. Their optical performance is instead governed by scattering and refractive index contrast. Scattering strength depends on the relative size of scattering features to wavelength, being a combination of Rayleigh scattering for sizes smaller than wavelength (decreasing roughly with λ^{-4} [57]) and Mie scattering for larger features than the wavelength, where scattering maybe independent of wavelength or decreases only slightly with wavelength.

Over the past two decades, several types of light sources have been employed in OCT systems, including SLDs, broadband LEDs, supercontinuum lasers, femtosecond lasers, and swept-source lasers. Each of these sources exhibits a unique combination of spectral bandwidth, output power, coherence properties, and system complexity.

Broadband LEDs were among the earliest sources used in time-domain OCT systems. While they offer wide spectral bandwidths, their low output power and poor spatial coherence limit their applicability in high-speed or deep-tissue

imaging. Supercontinuum sources, on the other hand, provide extremely broad spectra and high output power, but they are bulky, expensive, and require complex setup. These limitations have restricted their use to specialized research applications.

Swept-source lasers have gained popularity in recent years due to real-time OCT imaging, leading to own category of swept-source OCT (SS-OCT) systems. These lasers rapidly tune their emission wavelength over a spectral range, enabling high-speed imaging with about ~40 MHz sweep rate [58].

In contrast, SLDs offer an optimal balance between bandwidth, power, and system integration. SLDs combine the broad emission spectrum of LEDs with the high brightness and spatial coherence of laser diodes (LDs). They are compact, electrically pumped, and can have single transversal mode profile enabling efficient coupling to fiber-optic systems – these are essential features for achieving advanced functionality in compact and practical systems. Moreover, SLDs exhibit low temporal coherence that minimizes speckle noise and coherence artifacts in OCT images [59].

The design of an SLD involves suppressing optical feedback and cavity modes to prevent lasing while maintaining high spontaneous emission and optical gain. This is typically achieved by using tilted or anti-reflection-coated facets, angled waveguides, or integrating optical isolators. The resulting emission spectrum is smooth and broadband, with a coherence length suitable for high-resolution OCT. **Table 1** listed recent records on OCT inspections in the SWIR and mid-IR range based on different types of light sources (i.e. SC source, SLD, quantum cascade laser (QCL), optical parametric oscillator(OPO)), modalities, and applications, including our work [P4].

Table 1. OCT operations, modalities and types of light sources used in SWIR and mid-IR range

Operating wavelength	Type of light source	OCT imaging object	OCT modality	References
1.96 μm	SC	Paint layer	TD-OCT	Cheung *et al,* 2014 [22]
2.0 μm	SC	High-opacity paint layer	FD-OCT	Cheung *et al,* 2015 [21]
2.0 μm	SLD	Paint coating	TD-OCT	Bhuiyan *et al,* 2026 [P4]
2.2 μm	SC	Rodent brain	SD-OCT	Zhu *et al,* 2019 [19]
3.1-4.2 μm	SC	Porous ceramic	Time-encoded FD-OCT	Zorin *et al,* 2021 [60]
3.58-4.63 μm	SC	Layered ceramic, credit card	SD-OCT	Israelsen *et al,* 2019 [36]
6-8 μm	QCL	Biochemical composition, tissue structure	TD-OCT	Colley *et al,* 2007 [61]
5-11 μm	OPO	Volumetric imaging of bank card	TD-OCT	Charsley *et al,* 2024 [62]

1.3 Research objectives and questions

The overarching aim of this research is to develop and evaluate a broadband GaSb-based superluminescent diode (SLD) operating near the 2 µm wavelength, specifically tailored for OCT applications. This goal is driven by the need for compact, efficient, and high-performance light sources that can enhance imaging depth and resolution in OCT systems operating in the 2 µm spectral region. To achieve this aim, the research is structured around several key objectives:

- Develop advanced GaSb-based SLD designs addressing the need for broadband emission centered around 2 µm. This includes establishing self-consistent modelling tools, optimizing the QW compositions and waveguide configurations, and simulating component performance.

- Devising tailored fabrication processes and characterization routines enabling the development of SLD components with improved functionality. This includes developing ridge-waveguide (RWG) waveguide architectures, tailored facets coatings, full set of electrical and spectral measurements including coherence length. Establishing the interdependences between the fabrication processes and components performance is the ultimate goal for this category.

- Integration of the SLD into a fiber-based OCT system and demonstration of its imaging capabilities. This involves packaging the SLD component and fiber-coupling it to an interferometric setup, optimizing system parameters, and acquiring images of test samples. Analysis of the OCT imaging including evaluation of axial resolution, and imaging depth. The results will be compared with existing sources to highlight the advantages and limitations of the GaSb-based SLD.

Based on these objectives, the research seeks to answer the following questions:

- How to optimize the light-emitting heterostructures of GaSb-based SLD to push the performance limits for high power and broadband operation at around 2 µm?

- What are the practical considerations for integrating such a source into an OCT system?

- What future improvements can be made to enhance the device's performance and expand its applicability in OCT imaging and other interesting applications?

1.4 Thesis Structure

This thesis is composed of five chapters designed to guide the reader through the background, methodology, and main research results resulting in state-of-the-art performance for broadband GaSb-based SLDs, and the first implementation of such devices in a 2 μm OCT system.

Chapter 1 Started with presenting the background, and motivation for developing the OCT at longer wavelength, and included the generic objectives, main research questions, and the overview of the thesis structure.

Chapter 2 Reviews state-of-the art OCT modalities and available light sources and discusses potential OCT applications at long-wavelengths (SWIR, mid-IR). Then it discusses the role of semiconductor light sources including SLDs, and their working principles. Additional focus is given on the recent works on GaSb-based broadband SLDs around 2 μm wavelength region. Finally, the chapter surveys the existing OCT works in 2 μm and beyond, identifies gaps in recent research, and scope of bandgap engineering in GaSb-based III-V semiconductor heterostructure to implement broadband emission.

Chapter 3 Presents the design of broadband quantum-well heterostructures, waveguide geometry, and emission characteristics for gain structures, particularly for SLD and amplifier devices. Next, the detailed methodology and fabrication process of the SLD gain chips using in-house grown epitaxial wafers are discussed. It includes photolithography, plasma etching, metallization, and thin-film deposition steps etc. The chapter also describes experimental characterization techniques including *L-I-V* characteristics, spectral measurements in free-space, chip packaging in fiber coupled butterfly module and fiber-interferometer based OCT measurement.

Chapter 4 Showcases the main experimental results that are related to the papers forming the core of the thesis. First, the performance and development of broadband 2 μm SLDs reported in [P1] and [P2] are summarized. The chapter also presents the design optimization of broadband heterostructure based amplifiers in 2 μm using asymmetric quantum wells reported in [P3]. Then results of the first reported implementation of a 2 μm fiber-coupled SLD into a TD-OCT set-up is discussed. Details on the interferometer setup and OCT characterization of a paint-coated sample/object are presented.

Chapter 5 Summarizes the key findings of the experiments, including the limitations, and proposes directions for future research direction.

2 THEORETICAL BACKGROUND

This chapter provides an overview of OCT concepts. The discussion begins from the fundamental principles of the OCT, followed by an introduction of the major OCT modalities. The second part of the chapter transitions into the current state-of-the-art in light source technologies for OCT. Our particular emphasis will be given to the role of broadband low coherence sources operating in the short-wave infrared (SWIR) and mid-infrared (mid-IR) wavelength region. Finally, a highlight will be presented on the III-V SLDs operating around the 2 μm wavelength region and their potentials in OCT imaging.

2.1 OCT – basic concepts

OCT was first demonstrated by Huang *et al.* in 1991 [1] and is widely recognized as a leading non-invasive, high-resolution imaging modality. The first depth-resolved images were obtained using an 830 nm near-infrared (NIR) source, achieving an axial resolution of ~15 μm. In most practical applications, OCT light sources operate in the NIR wavelength region between 750 and 1500 nm [5, 23, 56].

The technique employs non-ionizing optical radiation and has had a significant impact in clinical disciplines, particularly in ophthalmology and angiography. OCT operates on the principle of low-coherence interferometry, detecting reflected or backscattered light from within a sample, which is then compared to a reference beam to produce an interference signal. Analysis of this interference pattern enables the reconstruction of real-time, cross-sectional (2D), and sub-surface volumetric (3D) images of the sample's microstructural features. The position of OCT among other imaging techniques is typically evaluated based on several key parameters, including axial resolution, penetration depth, imaging speed, system complexity, and the type of sample.

To obtain a 1D depth scan at one specific lateral position, often called an *A-Scan*, the light emitted by the OCT light source is focused to a small diameter spot, positioned on the specimen, and held stationary. The backscattered light and a reference light beam form an interference pattern that is Fourier transformed to

produce a 1D depth profile. A stack of adjacent A-scans produces a cross-section or *B-scan*. With the optical path fixed, rapid lateral scanning at a constant depth yields an "*en face"* or *C-scan*.

Modern OCT systems follow two main techniques: time-domain (TD-OCT) and Fourier-domain (FD-OCT) [2]. In TD-OCT, depth scanning is performed by mechanically stepping the reference delay. FD-OCT, by contrast, derives depth from the interferogram's spectrum, eliminating the need for a mechanical depth scan and allowing much faster acquisition speeds. FD-OCT is implemented in two forms: (i) spectral-domain (SD-OCT), which records the spectrum with a broadband source and a spectrometer, and (ii) swept-source (SS-OCT), which replaces the spectrometer with a tunable laser and a single detector, which favors long imaging ranges and very high A-scan rates. Although each modality has its own practical trade-offs, but the axial (depth) resolution is fundamentally determined by the optical bandwidth of the light source in TD-OCT and SD-OCT, and by the tuning bandwidth of the laser in case of SS-OCT.

2.1.1 Time-domain OCT (TD-OCT)

A TD-OCT system comprises a broadband optical source and a two-arm interferometer (typically a Michelson), microscope-class optics, and a detection/processing unit, as schematically shown in **Fig 5**.

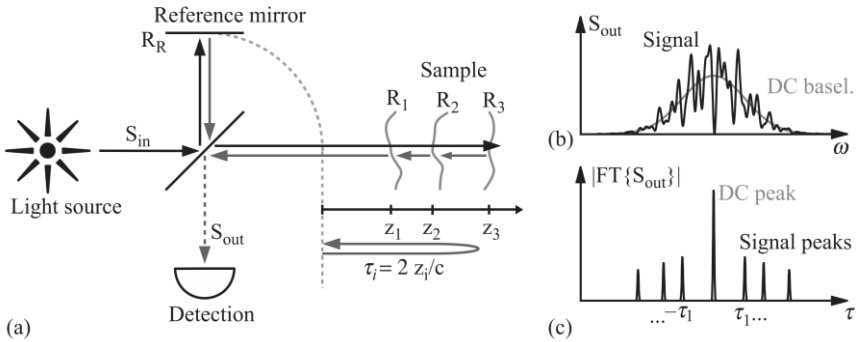


Figure 5. A broadband source feeds into the two-arms of a Michelson interferometer; the OCT system determines time delay, τ_i, between the light reflected from different depth, z_i, (b) Interference between the sample and the reference beam leads to a modulation of the output spectrum, S_{out}, and (c) the contributions with different delays τ_i, can be separated by applying a Fourier transform (FT) to the spectrum (figure adapted from [63]).

The beamsplitter divides the incident light into a reference arm, terminated by a mirror whose position is scanned to select depth, and a sample arm, which delivers and collects light from the object. The path length from the beamsplitter to the sample and back defines the sample path; the path to the reference mirror and back defines the reference path. Their difference defines the optical path difference (OPD).

TD-OCT typically employs a broadband superluminescent diode (SLD) and detects the interferometric signal with a photodetector. Signal acquisition principle can be understood using the schematic of Michelson interferometer setup shown in **Fig 5(a)**. The light source with the power spectral density $S_{in}(\omega)$ is split equally between the reference mirror with reflectivity R_R and a weakly reflecting sample with reflectivity, R_i. The light reflected from the sample encounters a time delay, τ_i, relative to the reference roundtrip time in the reference path. The power spectrum at the interferometer exit port is then [63]:

$$S_{out}(\omega) = \frac{1}{4}S_{in}(\omega) + \left(R_R + \sum_i R_i\right) + \frac{1}{4}S_{in}(\omega)\sum_{i\neq j}\sqrt{R_i R_j}\,cos\big(\omega[\tau_i - \tau_j]\big) \pm \frac{1}{2}S_{in}(\omega)\sum_i \sqrt{R_R R_i}\,cos(\omega\tau_i) \quad (2.1)$$

where ω denotes the angular optical frequency. The right-hand side of power spectrum output in equation (1) consists of three contributions:

- a “DC baseline” from the summed powers;
- an “autocorrelation” originates from the interference of the reflections from all sample layers with each other (usually negligible because $R_i \ll R_R$); and
- the desired “cross-correlation” between the reference beam and each sample reflection.

The interference signal in equation (1) is the sum of the oscillating term $cos(\omega\tau_i)$ originated from each reflection. Thereby, longer delay produces higher fringe frequency of the corresponding spectral interference pattern (Fig 4(b)). By Fourier transforming these components get separated by different time delays (Fig 4(c)). Because the amplitude terms are scaled with $\sqrt{R_i}$, the depth resolved reflectivity profile of the sample along the probing beam axis is obtained by squaring the magnitude of the Fourier-transformed signal. Since the detected signal also scales with $\sqrt{R_R}$, the weak reflections from the sample are amplified by the strong reference beam. This coherent detection scheme therefore makes OCT a sensitive imaging technique, enabling even detection of a weak sample reflection. The ± sign of the interference term represents the complementary intensity distribution between the

signals obtained from both output ports of the interferometer. We note that, in a Michelson interferometer, the input port is at the same time an output port. This can be exploited in an OCT system with dual balanced detection [64, 65]. By measuring the differential intensity between both output ports, the baseline and auto-correlation terms cancel out, yielding ideally the pure OCT signal.

In a TD-OCT system, in addition to the axial scan, a 2D transverse scan, and additional scan are required to acquire complete 3D OCT image data. Conversely, full-field OCT (FF-OCT) employs a broad-spectrum optical source with reduced spatial coherence to uniformly illuminate complete targeted samples and uses a complementary metal-oxide semiconductor (CMOS) or charge-coupled device (CCD) camera to capture an *en-face* image. Consequently, a single axial scan can yield a 3D OCT image, and no lateral scanning is necessary. FF-OCT usually uses lenses with high numerical apertures (NAs) for sample imaging, providing high resolution at the sub-micrometer level. In addition, FF-OCT has also been found to be effective in suppressing stray light using the coherent gate. Based on these advantages, FF-OCT has carried out a wide range of research applications in biomedical fields and nondestructive inspection of a large variety of samples [66].

2.1.2 Fourier-domain OCT (FD-OCT)

FD-OCT has emerged as a solution to overcome the slow imaging speed of conventional TD-OCT. This is achieved by eliminating the need to adjust the optical path length between the sample arm and the reference arm. Instead, the interference signals are obtained from a spectrometer, with the interferometric spectrum $I(\lambda)$ being defined by the following equation:

$$I(\lambda) = S(\lambda)\left\langle E_R ex\,p\left(i\frac{2\pi}{\lambda}2r\right) + \int_{-\infty}^{+\infty} a(z)\,exp\left\{i\frac{2\pi}{\lambda}2(r+nz)\right\}dz\right\rangle \qquad (2.2)$$

In Eq. 2.2, $S(\lambda)$ represents the spectral density function of the light source, E_R signifies the reference light amplitude, $a(z)$ denotes the amplitude of the backscattered light at a specific depth z in sample, n represents the refractive index of the sample, $2r$ is the optical path length of the reference arm, and $2(r + nz)$ denotes the corresponding optical range length at sample depth z. The second term represents the coherent spectrum, while the first terms are considered as noise and are eliminated, as shown in Eq. 2.3:

$$I(z) \propto F(S(\lambda)) \otimes [a(z) + a^*(z)] \tag{2.3}$$

We recall that FD-OCT can be categorized into two main types: SD-OCT and swept-source SS-OCT, each based on distinct implementation approaches. **Fig. 6** illustrates the schematic diagram of a typical SD-OCT system that uses a wideband optical source for illuminating the sample and a spectrometer for measuring the interference spectrum. The imaging process of SD-OCT closely resembles that of TD-OCT, except that SD-OCT no longer requires the motion of the reference arm to scan sample for depth position information. On the contrary, SS–OCT system probes sample with a swept light source, while a rapid detector is used to capture the interference spectrum.

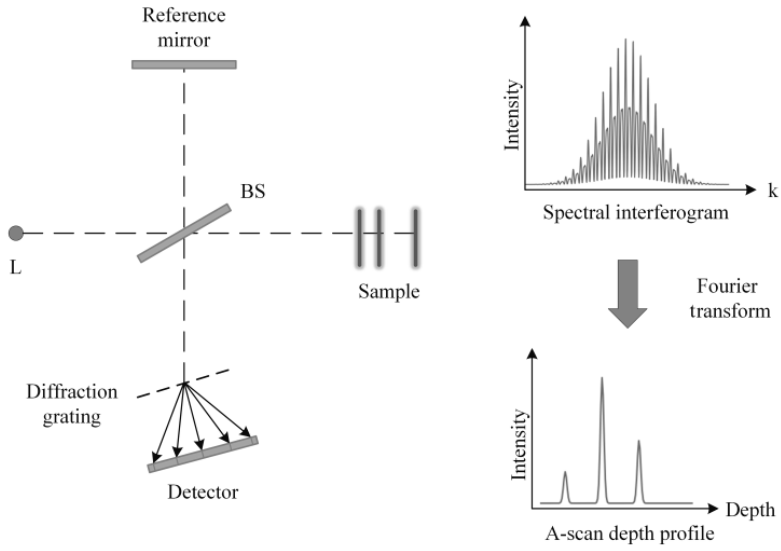


Figure 6. Schematic of a spectral domain OCT system (figure adapted from [23]).

2.2 Superluminescent diode (SLD)

2.2.1 Basic operation principles

An SLD is a low coherence source that governed by the mechanism of amplified spontaneous emission (ASE). In the active region of SLD, injected carriers recombine radiatively, by spontaneous emission. Unlike a standard LED, where emission is isotropic and broadband, in an SLD the optical waveguide confines the photons, enabling stimulated amplification as they propagate along the cavity. The result is a highly directional output beam, like that of an LD, but with a spectrally broadened emission resembling an LED. Unlike LDs, SLDs are specifically designed to suppress resonant optical feedback within the cavity, which prevents lasing. This is commonly achieved by minimizing facet reflectivities and tailoring the waveguide to reduce longitudinal mode formation [67, 68]. The absence of lasing ensures that the ASE process dominates, yielding broadband emission with smooth spectral characteristics. For an SLD (edge-emitting traveling-wave amplifier) with negligible cavity reflections, the output power is expressed as:

$$P_{out} = P_{spon} \cdot G_s \tag{2.4}$$

where P_{spon} is the power generated by spontaneous emission and G_s is the single-pass optical gain, given by:

$$G_s = \exp[(\Gamma g_0 - \alpha_{abs})L] \tag{2.5}$$

Here, Γ is the optical confinement factor, g_0 is the material gain coefficient, α_{abs} is the absorption coefficient, and L is the length of the cavity.

In practice, residual facet reflections (R_1, R_2) cannot be fully eliminated. The interference between forward- and backward-propagating waves introduces Fabry–Pérot (FP) modulations in the emission spectrum. Under these conditions, the effective cavity gain is:

$$G(\lambda) = \frac{H\ G_s}{(1 + K^2 - 2K\cos[\beta(\lambda)L])} \tag{2.6}$$

where,

- $H = \left(1 - \sqrt{R_1}\right)\left(1 + \sqrt{R_2}\right)^2$
- $K = \sqrt{R_1 R_2} \cdot G_s$
- $\beta(\lambda) = \frac{(2\pi\, n_{eff})}{\lambda}$ is the propagation constant, with n_{eff} the effective index of the guided mode.

The spectral modulation depth (*SM*), which quantifies ripples in the emission spectrum, is written as:

$$SM = \frac{(G_{max} - G_{min})}{(G_{max} + G_{min})} = \frac{2K}{(1 + K^2)} \tag{2.7}$$

Minimizing *SM* is critical for broadband applications, where smooth spectra are required. The output power of an SLD with finite facet reflectivities is expressed as [147]:

$$P_{out} = P_{spon}(G_s - 1)\, \frac{[(1 - R_1)(R_2 G_s + 1)]}{[1 + (R_1 R_2 G_s^2) - 2R_1 R_2 G_s\, cos(\beta(\lambda)L)]} \tag{2.8}$$

From these equations, several key observations can be made followingly:

- In the limit of negligible facet reflectivity (R_1, $R_2 \rightarrow 0$), the device behaves as an ideal traveling-wave amplifier with smooth broadband output.
- Increasing cavity length enhances output power but deepens FP modulation.
- The spectral smoothness depends strongly on facet reflectivities and internal losses.
- Output power increases super-linearly with injection current until gain saturation is reached.

Depending on the effective reflectivity of the device facets, two distinct ASE propagation regimes can be identified: single-pass and double-pass amplification. If the back facet reflectivity is low, light propagating toward the rear facet exits or is absorbed, while light moving toward the front facet experiences amplification over a single pass length L. The single-pass output power (P_{SP}) is:

$$P_{SP} = P_{spon} \cdot G_s \tag{2.9}$$

If the back facet reflectivity is relatively high, part of the backward-propagating light is reflected and undergoes a second amplification pass before emerging from the front facet. In this case, the effective amplification length is doubled, and the output power is approximately:

$$P_{DP} \approx P_{spon} \cdot R_2 \cdot G_s^2 \tag{2.10}$$

Double-pass amplification is therefore more power-efficient than single-pass operation, enabling higher output at shorter cavity length and/or lower drive currents. As a drawback, however, it introduces stronger FP spectral modulations, compromising spectral smoothness.

The maximum achievable output power of a superluminescent diode (SLD) is fundamentally limited by gain saturation in the active region. Under increasing injection current, the carrier density initially rises, allowing the stimulated emission process to dominate and the optical output to grow super-linearly. However, at sufficiently high injection levels, the carrier density reaches a point where the available carriers cannot sustain exponential photon amplification along with the device length. This condition, known as gain saturation, results in a reduction of differential gain, spectral narrowing, and eventual power clamping.

Several factors contribute to this limitation, QW confinement factor (Γ) is one of them. The confinement factor defines the overlap between the optical mode and the active quantum wells. A higher confinement factor enhances light–matter interaction, but it also increases the rate at which carriers are depleted by stimulated emission, thereby lowering the saturation power. Conversely, a lower confinement factor can delay the onset of saturation, albeit at the expense of modal gain.

Another important factor determining gain saturation is carrier lifetime and recombination dynamics. At high injection levels, nonradiative recombination processes (such as Auger recombination or carrier leakage into barrier regions) become significant. These processes reduce the effective carrier lifetime, limiting the replenishment rate of carriers available for stimulated emission. As a result, the gain medium is unable to sustain further increases in photon density, leading to saturation.

Moreover, optical losses and waveguide design plays a limiting factor that explain internal losses such as free-carrier absorption, intervalence band absorption, or scattering losses, all of which compete with the net gain. Poorly optimized waveguide structures can exacerbate these losses. At the same time, waveguide geometry (ridge width, confinement, and depth) influences both the spatial distribution of the optical field and the carrier density, directly affecting saturation characteristics.

Hence, SLD design and optimization involve a delicate balance between maximizing output power and maintaining spectral smoothness. In one hand, longer gain sections and higher facet reflectivities allow the optical field to experience stronger amplification and improved output levels, with increased residual cavity effects, which manifest as Fabry–Pérot modulations in the spectrum. On the other hand, shorter cavities and minimized facet reflectivities suppress longitudinal feedback, resulting in smoother, ripple-free spectra. Yet, this reduction in effective amplification length limits the total achievable output power. Thus, there is an inherent trade-off – devices designed for high brightness tend to favor longer cavities and controlled feedback but may suffer degraded spectral uniformity.

Devices optimized for broadband, low-coherence emission (e.g., for optical coherence tomography) favor short cavities with strongly suppressed reflections, but at the cost of lower maximum power. The practical operating point of an SLD is therefore determined by the target application. For instance, OCT imaging applications prioritize spectral smoothness and emission bandwidth, whereas optical communication or pumping applications often prioritize maximum achievable output power.

2.2.2 Waveguide design considerations

Fig. 7 illustrates the principal structural configurations employed in SLDs to suppress optical feedback and prevent lasing. A reference typical edge emitting laser diode (LD) is also displayed at the top of figure. In these SLD waveguide geometries, each approach targets the disruption of the optical cavity resonance, thereby ensuring low temporal coherence while maintaining high spatial coherence. Some significant cavity suppression strategies in the waveguide design are described below:

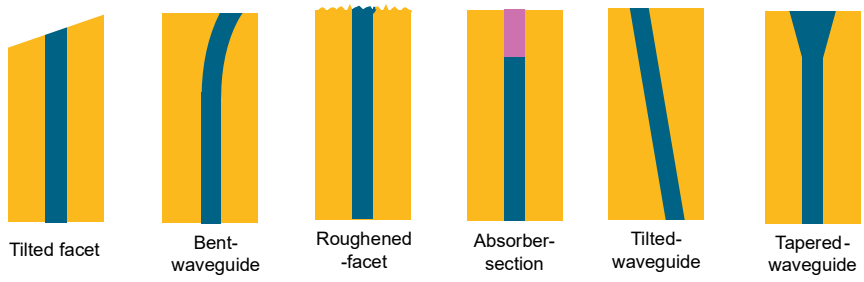


Figure 7. Schematic comparisons of different SLD waveguide configurations. Adapted from [69].

Tilted-facet: In the tilted output facet configuration, the output facet of the ridge waveguide is cut at an angle. This geometric modification minimizes the probability of back-reflection into the active region, breaking the feedback loop that would otherwise sustain lasing. The result is a broadband ASE spectrum with reduced coherence length.

Bent waveguide: The bent or curved waveguide introduces a gentle curvature into the optical path. This bending prevents reflected photons from efficiently re-entering the gain region, lowering cavity feedback. The design is simple but effective in suppressing resonance, particularly when combined with anti-reflection coatings.

Roughened facet: Finally, the roughened facet method intentionally roughens one output facet. Instead of reflecting light back into the cavity, the roughened surface scatters it away, effectively destroying standing wave formation. This approach ensures that resonance is fully suppressed and contributes to maintaining a broad emission spectrum.

Absorber incorporation: The incorporation of absorber sections, either reverse-biased (active) or unpumped (passive), serves as another suppression method. These segments absorb residual back-reflected light within the cavity, thereby eliminating unwanted feedback. This technique is often used in combination with tilted or tapered structures for enhanced suppression.

Tilted-waveguide: The tilted waveguide approach involves tilting the entire ridge relative to the facets, rather than adjusting the facet alone. This deliberate misalignment reduces the formation of longitudinal modes and favors ASE across a broader spectral range. Such a design ensures smooth spectral output suitable for interferometric applications.

Tapered-waveguide: In the tapered active region, the waveguide gradually broadens towards the output facet. This geometry reduces reflections at the interface and allows the device to sustain higher output powers without significant mode competition. The taper provides both stability and efficiency, making it valuable in high-brightness applications.

2.3 Bandgap engineering in GaSb heterostructure

III–V semiconductors consist of crystalline structures wherein group-III and group-V elements are combined. The crystal structure is often the zinc blende lattice with interpenetrating group-III and group-V sub-lattices, where each group's atom is bonded to four neighboring atoms from the other group, and vice versa. By tailoring

the elemental composition in these sublattices, one can tune a band structure and lattice-constant. Given the number of elements to chosen from, this results into broad tunability in the band-gap and capacity to fabricate light emitting or absorbing devices at different wavelengths.

Fig. 8 shows energy bandgaps (and corresponding wavelength) in relation to their lattice constant of some commonly used III-V semiconductor materials at 300 K. The figure also shows how compositional engineering can be done in a heterostructure without a large lattice mismatch, such as two binary III-V compounds (i.e. AlSb and GaSb) having different energy bandgaps E_g are mixed to form a ternary alloy in a crystal structure ($Al_xGa_{1-x}Sb$) which has an intermediate bandgap depending on the mole fraction of each alloyed component "x":

$$E_g(Al_xGa_{1-x}Sb) = (1-x)E_g(GaSb) + xE_g(AlSb) - C(1-x)x$$

where C is the bowing parameter indicating the deviation of the ternary bandgaps between linearly interpolated and experimental values [70]. The above linear interpolation can be extended to quaternary alloys, such as GaInAsSb, using interpolation of ternary parameters [71].

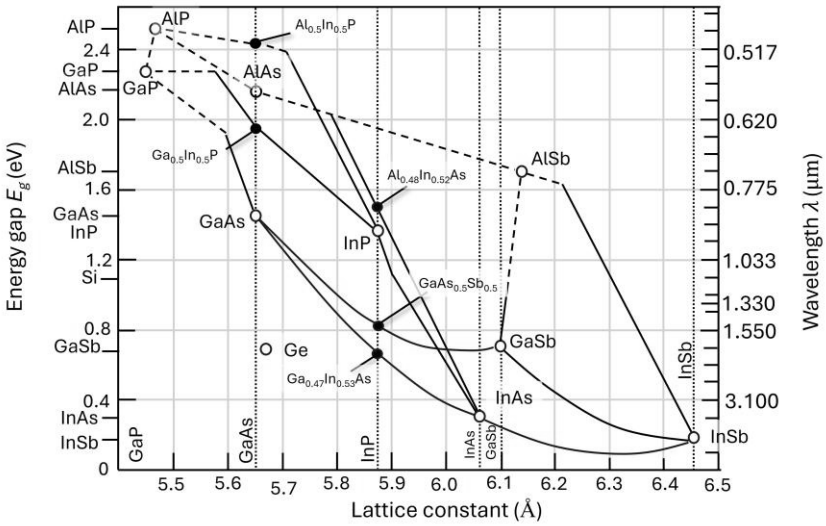


Figure 8. Energy gap (E_g) vs. lattice constant at room temperature for various III-V semiconductors and their alloys. Circles represent binaries, solid and dashed lines ternaries, and areas between them quaternaries. (figure adapted from [72])

Combining different III-V alloys stacked on top of each other, i.e. formation of heterostructures, enables realization of specific functional properties. In these

heterostructures, the band structure engineering is primarily controlled by (i) composition engineering or alloying, (ii) quantum confinement, and (iii) doping. For example, the active region of a typical GaSb type-I laser diode heterostructure contains one or several thin GaInSb QW layers which have a narrow bandgap and are sandwiched between two AlGaAsSb barrier layers with larger bandgap. This creates a confining potential well for the injected carriers in the conduction and valance band and limits their movement.

If the quantum-well thickness "*d*" is comparable to de Broglie wavelength of the carriers, their energies become quantized. For example, the de Broglie wavelength for an electron moving in such well due to free thermal energy can be approximated as $\lambda_{th} \sim h/\sqrt{2\pi m k_B T}$, where h is the Plank's constant, m the carrier effective mass, k_B the Boltzmann constant and T the temperature. For GaSb-based system the estimated well width is of ~20 nm [70] which is readily within the fabrication limits of the epitaxial growth methods. This unlocks the concept of band structure engineering that employs varying the thickness of the QWs, practiced SLD devices in this thesis, to tune wavelength and other emission properties outside of the bulky alloy bandgaps.

In GaSb-based heterostructures, GaInSb wells are compressively strained on GaSb substrates because the incorporation of indium increases its lattice constant. Compressive strain removes the degeneracy between heavy-hole (HH) and light-hole (LH) bands, pushing the HH band upward and the LH band downward. This increases the HH–LH splitting, favoring TE-polarized transitions [73]. However, strain must be carefully controlled. If a strained layer exceeds its critical thickness, relaxation occurs through the formation of misfit dislocations, which introduce deep non-radiative centres that drastically reduce efficiency. Because many mid-IR devices require multiple QWs to achieve sufficient optical gain or ASE power, the cumulative strain budget becomes a limitation. The solution, widely adopted in mid-IR structures is strain balancing, wherein tensile-strained barriers (such as AlGaAsSb) partially compensate the compressive strain of the wells. This enables MQW stacks with much larger total thicknesses to remain fully pseudomorphic while maintaining desired optical properties.

Fig. 9. schematically shows "Type-I band alignment", commonly found in laser diode heterostructures. In this sort of alignment case both electrons and holes are confined within the same QW, leading to efficient radiative recombination. The choice of barrier material is therefore critical. For gain chips operating in the 2–3 μm wavelength region, $Al_xGa_{1-x}As_ySb_{1-y}$ is commonly employed as a lattice-matched waveguide, barrier, and cladding material in the heterostructure. The waveguide is

designed to minimize optical field penetration into the cladding layers (introduces absorption losses) and to maximize overlap with the active QWs, thus improving modal gain. The active region, comprising QWs and barriers, is sandwiched between p- and n-doped cladding layers of $Al_xGa_{1-x}As_ySb_{1-y}$. Typically, the cladding layers contain a higher aluminum fraction than the barrier or waveguide, since increasing Al content raises the bandgap and lowers the refractive index. This refractive index contrast enhances optical confinement in the active region, while the larger bandgap provides strong carrier confinement [74]. In this thesis, arsenic-free GaInSb/AlGaAsSb QW gain structures emitting around 2 µm are presented, with ongoing research directed toward further wavelength extension and emission.

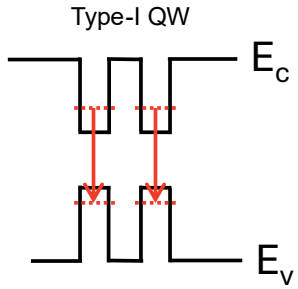


Figure 9. Type-I band alignment of semiconductor heterostructures. E_c and E_v refer to the valence and conduction band edge, respectively. The red arrow in the QWs indicates possible electronic transitions.

3 METHODOLOGY

3.1 Design approach for GaSb-based broadband heterostructures

Advanced simulation tool such as Photon Design's Harold model's [75] simulation framework employs a self-consistent coupled-physics approach, solving Poisson's equation for electrostatic potential, current continuity equations for carrier transport, capture–escape balance equations for QW carrier dynamics, photon rate equations for optical field evolution as well as heat flow equations for thermal effects. The simulation tool computes the optical mode profile by solving the vertical and longitudinal wave equations, while the Schrödinger equation is applied to determine confined states in the QWs. The optical gain is evaluated using parabolic band approximation as described by Asada et al. [76].

The model accounts for carrier transport in MQW systems, resolving the spatial distributions of electron and hole densities for both confined (in QW) and unconfined (barrier/separate confinement heterostructure) carriers. A simplifying assumption is adopted, wherein carrier capture and escape times are treated as constants across all QWs, neglecting potential variations due to local strain or compositional fluctuations. The bandgaps and general material parameters for the $Ga_{1-x}In_xSb$ and $Al_xGa_{1-x}As_ySb_{1-y}$ materials used in the heterostructures were taken from literature [70, 77]. We simulate the gain structure in isothermal operation mode (pulsed mode). The temperature dependency of the compound semiconductor band gaps were interpolated from the binary alloy parameters using the semi-empirical Varshni model [78].

The optical gain spectra of a single QW are evaluated by the simulator following the standard expression:

$$g(E_{phot.}) = \frac{\pi\hbar q^2}{ncm_e\varepsilon_0} M^2 \frac{1}{E} \sum_{j=1} K_{ij} A_{ij}(E_{phot.}) D_{ij}[F_j(E_{phot.}) - F_i(E_{phot.})] \qquad (3.1)$$

where $E_{phot.}$ is the photon energy, K_{ij} is the overlap integral of the transition state *i* and *j*, A_{ij} is the dipole moment enhancement factor, *n* is the real part of the refractive index, *q* is the free electron charge, m_e is the electron mass, $\hbar$ is the plank's constant,

ε_0 is the free space dielectric constant, c is the speed of light, M^2 is the dipole moment of the bulk material, $F_j(E_{phot.})$ and $F_i(E_{phot.})$ are fermi occupation factors, D_{ij} is the reduced density of states for the transition between *j*-th and *i*-th energy levels. Then the spontaneous emission rate is evaluated by

$$r_{sp}(E_{phot.}) = \frac{q^2 n^3 E_{phot.}}{\pi\hbar^2 m_e^2 c^3 \varepsilon_0} M^2 \sum_{j=1} K_{ij} D_{ij} F_j(E_{phot.})[1 - F_i(E_{phot.})] \quad (3.2)$$

and is consistent with the expression of gain model. The summation operation loop flows for all quantum confined states. Thus, the gain and the spontaneous emission spectrum are subsequently calculated using the following expressions:

$$G(\hbar\omega) = \int g(E_{phot.}) L(\hbar\omega - E_{phot.}) dE_{phot.} \quad (3.3)$$

$$R_{QW}^{sp}(\hbar\omega) = \int r_{sp}(E_{phot.}) L(\hbar\omega - E_{phot.}) dE_{phot.} \quad (3.4)$$

where $L(x)$ is the Lorentzian shape function. Broadening in gain and spontaneous emission expressions are based on convolution of gain and spontaneous emission rate with Lorentzian function, respectively.

The numerical parameters used in the simulation are listed in the **Table. 2**.

Table 2. Simulation parameters and their values [P3]

Parameter (symbol)	Value (unit)
Intraband relaxation time (τ_{in})	1e-13 s
Shockley-Read-Hall lifetime of electron (τ_{e-SRH})	1e-07 s
Shockley-Read-Hall lifetime of hole (τ_{h-SRH})	1e-07 s
Capture time constant of electron (τ_e^{cap})	5e-12 s
Capture time constant of hole (τ_h^{cap})	3e-13 s
Gain factor	0.6
Fraction of spontaneous emission coupled into optical mode	0.0001
Mirror reflectivity (both facets)	1e-07
Scattering loss (cm^{-1})	4.5

Initially we designed a set of gain structures based on SQW and DQW. All active region of the gain structures included type-I compressively strained $Ga_{0.73}In_{0.27}Sb$ QWs, separated by 20 nm of $Al_{0.25}Ga_{0.75}As_{0.02}Sb_{0.98}$ barriers lattice matched to GaSb. The QWs were embedded within 130 nm waveguide material from both sides. The

waveguide region was surrounded by ~1 μm thick n- and p-doped cladding layers consisting of higher band gap $Al_{0.5}Ga_{0.5}As_{0.04}Sb_{0.96}$ alloy, which is also lattice matched to GaSb. The epitaxial structure was finalized by a highly doped p-GaSb contact (cap) layer. The generic epitaxial structure is shown in **Fig. 10**; we show here only single QW on the figure. For double or multiple QW cases analyzed in the next sections, we used a 20 nm- $Al_{0.25}Ga_{0.75}As_{0.02}Sb_{0.98}$ barrier between adjacent QWs. The epitaxial structure was processed to define waveguide device configured as a broad-area (BA) laser diode (LD) structure with a stripe width of 80 μm and a cavity length of 2 mm.

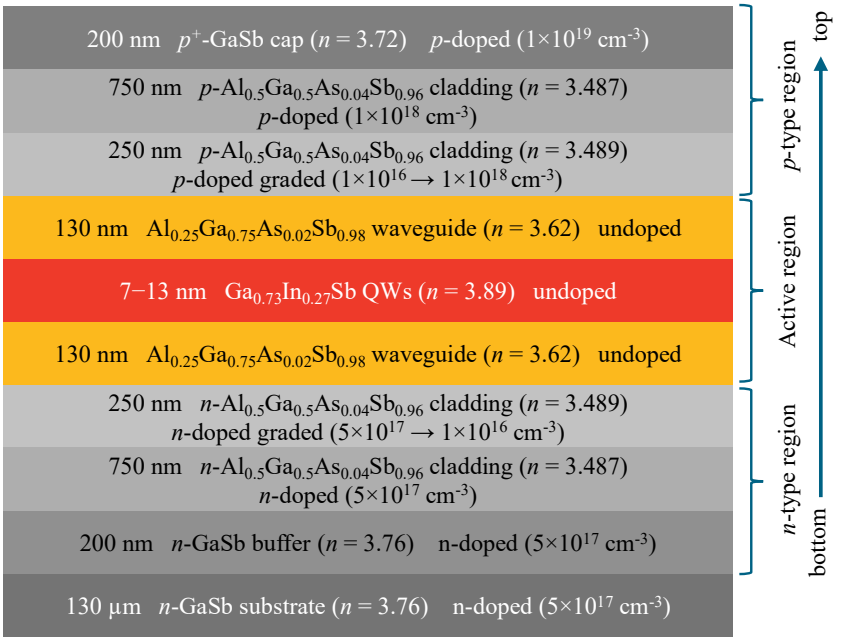


Figure 10. Epitaxial layer structure and the key parameters considered in the simulated gain structures. The QW thickness varied from 7 nm to 13 nm. In case of double or multiple QWs, a 20 nm barrier with similar composition of waveguide was used between two adjacent QWs [P3].

By varying the number of QWs, their thicknesses, and the surrounding barrier layers, it is possible to access various energy levels of confined states in QWs such that multiple energy transitions contribute to broadening the gain spectrum. However, given the large number of degrees of freedom in such structures, the design of broadband gain in heterostructure requires systematic approach to optimize the gain features while considering physical design constraints. The Harold model takes into account carrier transport, and waveguiding optical confinement, provides design flexibility of such gain structures. Similar sort of laser diode simulation were done based on InP at 2 μm [79], and GaSb at 2.3 μm [80, 81].

A simplified schematic of the simulated heterostructures used in the study is shown in **Fig. 11**. We first explore the simulation results with respect to single QW (SQW) structures with different thicknesses to observe basic trends setting the base of comparison with more advanced structures. Then these simulations are extended to double-QW (DQW) and multi-QW (MQW) configurations to evaluate the role of QW thickness variation in broadening the gain profile. Although it is somewhat marginal for the ultimate scope, our choice for engineering the bandgap based on changing the QW thickness instead of alloy composition is motivated by a higher accuracy in fabrication, i.e. higher precision in controlling the thickness.

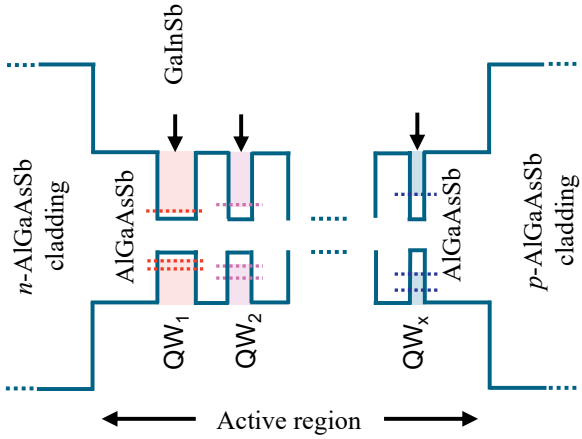


Figure 11. Schematic of GaInSb/AlGaAsSb QW gain structure defining the generic design framework for simulation. The number of QWs and their individual thicknesses are varied during the optimization routine. Reproduced from [P3].

3.1.1 Validation of "Harold model" simulation

In addition to simulating the lasing action, Harold model allows evaluation of QW material gain and spontaneous emission characteristics by setting the reflectivities at both mirror facets close to zero (~10^{-7}). To validate the modeling parameters, we initially simulated the spontaneous emission and lasing characteristics of a structure incorporating a DQW (7 nm, 13 nm) gain region. The selected design was experimentally realized, and its optical properties were characterized through photoluminescence (PL) and LD characteristic measurements, which were then used as benchmark to adjust the key parameters of the simulator.

Fig. 12(a) shows the comparison fit for PL revealing an excellent matching in spontaneous emission peaks at ~1950 nm and ~2090 nm between the simulated and experimental structure. The calculated emission bandwidth is ~300 nm FWHM at a carrier density of ~3e17 cm^{-3}. Intensity mismatch (~25 nm) on the shorter wavelength side is mainly due to atmospheric absorption, while minor discrepancies arise from experimental conditions (532 nm CW excitation at ~90 mW power). To further validate the model, we simulated the performance of a broad-area laser diode (2 mm × 80 µm) incorporating the same DQW active region in heterostructure with slightly thicker cladding. **Fig. 12(b)** compares the simulated and experimental light–current (*L–I*) characteristics under pulsed operation at room temperature. The inset presents the corresponding current–voltage (*I–V*) characteristics. The simulation shows again good agreement with the experimental threshold behavior and output power slope across the full bias range. These results support the validity of the simulation setting the relevant parameters used in simulation.

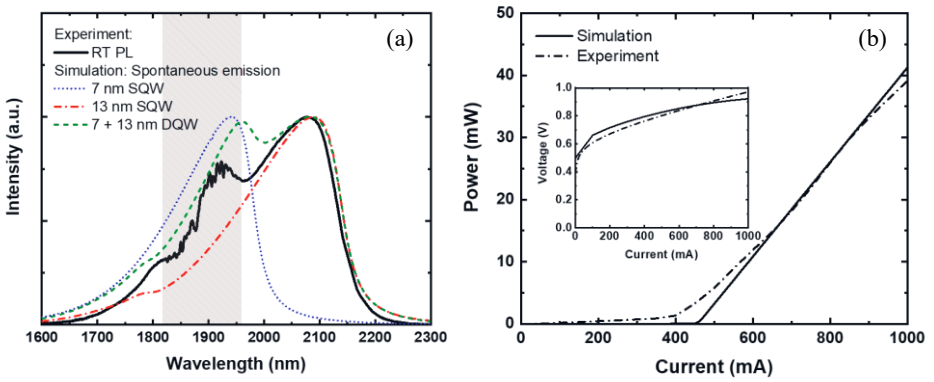


Figure 12. (a) Room-temperature PL spectrum from a DQW gain structure with 7 nm and 13 nm wells. Simulated spontaneous emission spectrum (SQW, DQW) are fitted for carrier density ~3e17 cm^{-3}. (b) Experimental and simulated characteristics for the broad-area laser diode (BA-LD) structure with the same DQW heterostructure. Reproduced from [P3].

3.1.2 Lateral waveguide design of SLD device architecture

The fundamental concept behind designing the SLDs waveguide aims at ensuring a single-mode transverse operation and high output power with efficient ASE, while minimizing the reflection from the facets to avoid lasing and ensure a smooth optical spectrum. To this end, we have chosen a J-shaped ridge waveguide RWG architecture, shown in **Fig. 13**. The front-facet (green) on the right-hand side (used as the main output) had a low reflectivity, while the reflectivity of the back-facet (red)

on the left-hand side was used as a tailoring parameter for controlling the trade-off between the output power and ASE on one side, and the FP-related spectral ripples on the other side.

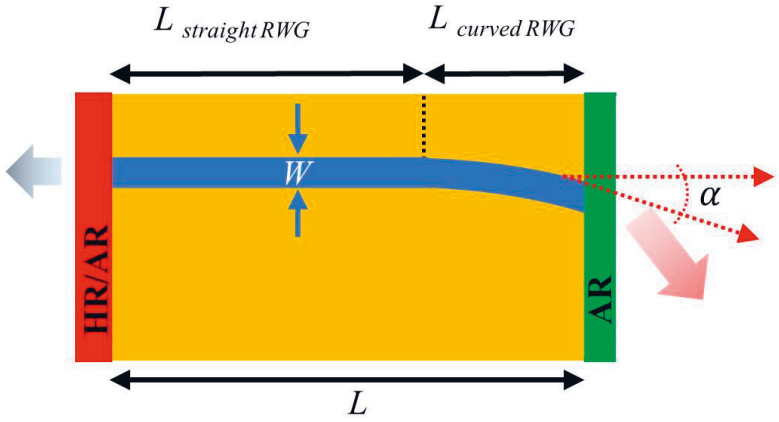


Figure 13. Schematic of J-shaped SLD cavity geometry. The front facet was coated with anti-reflective (AR) and rear facet are coated with high reflective (HR) or anti-reflective (AR) dielectric coatings. Reproduced from [P1].

3.2 Fabrication and processing

3.2.1 Epitaxial growth

Molecular beam epitaxy (MBE) is the most common technique for epitaxial growth of GaSb-based heterostructures. In MBE growth, ultra-pure elements (>99.999%) are heated within an ultra-high vacuum (~10^{-10} mbar) environment in crucibles which forms highly directional atomic or molecular beams. These beams impinge upon a heated single-crystal substrate, where the constituent atoms can adsorb, diffuse, desorb, or incorporate into energetically favorable surface lattice sites, leading to atomic layer-by-layer growth. For the epitaxy of GaSb, the substrate temperature is typically maintained around 500°C to produce high-quality crystalline growth. In the present work, all epitaxial structures were grown on commercially available n-doped GaSb substrates with a (100) surface orientation, a diameter of 2 inches, and an approximate thickness of 500 µm.

Schematic of a typical MBE system is shown in **Fig. 14**. Within the MBE growth chamber, group III elements such as gallium (Ga), indium (In), and aluminum (Al) are thermally evaporated from effusion cells. The beam flux of each element is regulated by precisely controlling the material temperature within each crucible.

The deposition process in MBE is controlled using mechanical shutters positioned in front of the effusion cells, which can rapidly block or let pass the atomic beams directed toward the centrally positioned substrate. To promote lateral uniformity in composition and thickness, the substrate is continuously rotated during the growth process. Group V elements, namely arsenic (As) and antimony (Sb), are introduced from dedicated sources. A needle valve positioned between the bulk zone and the growth chamber allows for precise tuning of group V fluxes.

Doping of the GaSb-based layers is achieved through the introduction of dopant atoms from dedicated effusion cells, operating in the same way as those used for group III species. For n-type doping, tellurium (Te) is supplied, while beryllium (Be) is utilized for p-type doping, sourced from a pure Be effusion cell.

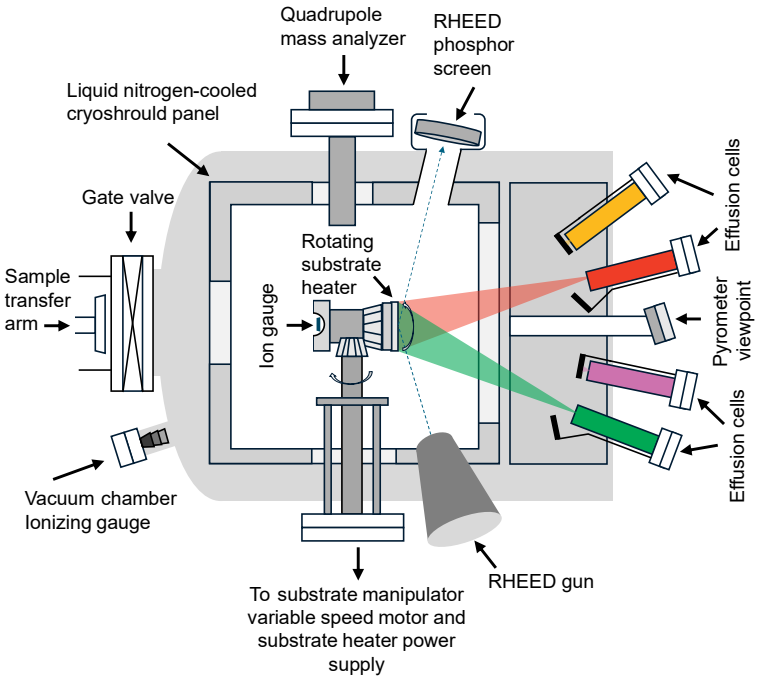


Figure 14. Schematic of the geometry of a typical MBE growth chamber and its key components.

3.2.2 SLD device processing

The fabrication of SLD devices discussed in [P1–P4] are based on ridge waveguide (RWG), which provides lateral optical confinement and enables efficient current injection. The processing sequence involves multiple lithography steps performed on quarter-wafer samples cleaved from 2-inch diameter of GaSb heterostructures grown by MBE. The key fabrication stages are outlined below:

***RWG patterning*:** The first step in a standard RWG laser fabrication flow (see in **Fig. 15**) is the definition of the ridge structure. A 300 nm thick silicon dioxide (SiO_2) layer on the GaSb epi-structure, deposited by plasma-enhanced chemical vapor deposition (PECVD), serves as a hard mask during etching. The SiO_2 is deposited at a rate of ~1.1 nm/s by introducing silane (SiH_4) and nitrous oxide (N_2O) into the PECVD chamber, operating at 300°C and 1000 mTorr pressure. The next step is to perform photolithography. First hexamethyldisilane (HMDS) is evaporated on the sample surface to enhance adhesion of photoresist layer. Positive tone photoresist AZ ECI 3012 is spin-coated on the sample and soft-baked to evaporate out the excess solvent. The resist layer is patterned by exposing ultraviolet (UV) light through a quartz photomask with chromium patterns. In this work, exposure is performed with a SUSS MA6 mask aligner in contact mode. Immediate after UV exposure on the sample, post-exposure bake is followed and then the is developed with AZ 726 MIF developer, leaving a direct replica of the mask pattern on the resist. A post-develop bake (hard bake) at 120°C is applied to improve mechanical stability of the photoresist. The underlying SiO_2 layer is then etched by reactive ion etching (RIE), with the resist serving as the etch mask. In this plasma process, CHF_3 is used as the main etching gas, with O_2 added to optimize etch selectivity and rate. Typical etch rates in this work were about 0.4 nm/s depending on the gas composition. After etching, the resist is stripped with Microposit remover 1165 at 80°C, followed by O_2 plasma cleaning. The RWG pattern is formed in the GaSb-based epitaxial layers using inductively coupled plasma RIE (ICP-RIE) with chlorine (Cl_2) gas together with nitrogen (N_2) gas. Cl_2 provides chemical etching by forming volatile group-V halides, while inert gas like N_2 enhances sidewall passivation and contributes to anisotropic etching. The etch rate and morphology are strongly dependent on process conditions such as ICP power, RF power, and gas composition. The process parameters followed optimized recipes developed at ORC. Following ridge formation, the remaining SiO_2 hard mask is removed by an additional RIE step with CHF_3/O_2.

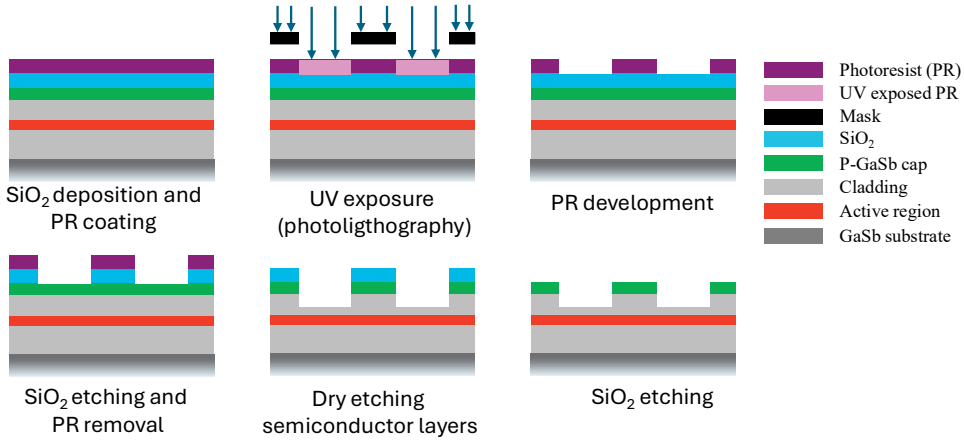


Figure 15. RWG etch processing steps.

RWG contact window formation: After ridge definition, a dielectric layer is deposited to confine current injection to the ridge top. A 100 nm thick silicon nitride (SiN_X) layer is deposited by PECVD from SiH_4 and NH_3 at 300°C. The sample is then spin-coated with AZ ECI 3027 resist, exposed in proximity mode on the SUSS MA6 aligner, and developed in AZ 726 MIF developer. The SiN_x is etched in CHF_3/O_2 plasma at a rate of ~1.0 nm/s, and the resist is subsequently removed by solvent stripping and O_2 plasma. Representative steps are shown in **Fig. 16**.

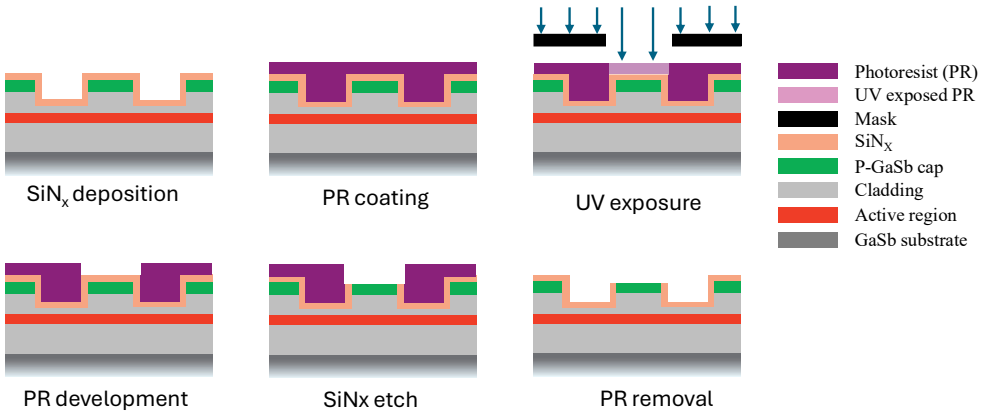


Figure 16. RWG contact opening process steps.

p-contact metallization: Following HCL treatment to remove native oxide from surface, The top electrical contact is deposited on a highly p-doped GaSb cap layer to minimize contact resistance. The process steps are shown in **Fig 17**. A multilayer

of “50 nm Ti / 50 nm Pt / 125 nm Au” stack is deposited by e-beam evaporation. Here Ti improves adhesion, Pt acts as a diffusion barrier against Au penetration into semiconductor. While Au provides low resistance ohmic p-contact, it also serves as a bonding layer for wire bonding or soldering.

The P-metal contacts are patterned using a lift-off process with the image reversal resist AZ 5214E and two-step UV exposure. The resist is first spin-coated and exposed through a p-metal contact mask, baked at the image reversal temperature, then flood-exposed and developed to create an undercut profile. This negative profile ensures clean lift-off during metal deposition, even when sidewalls are coated. After evaporation, the sample is immersed in Microposit Remover 1165 at 80°C to lift off the unwanted metal, leaving the defined contact pattern.

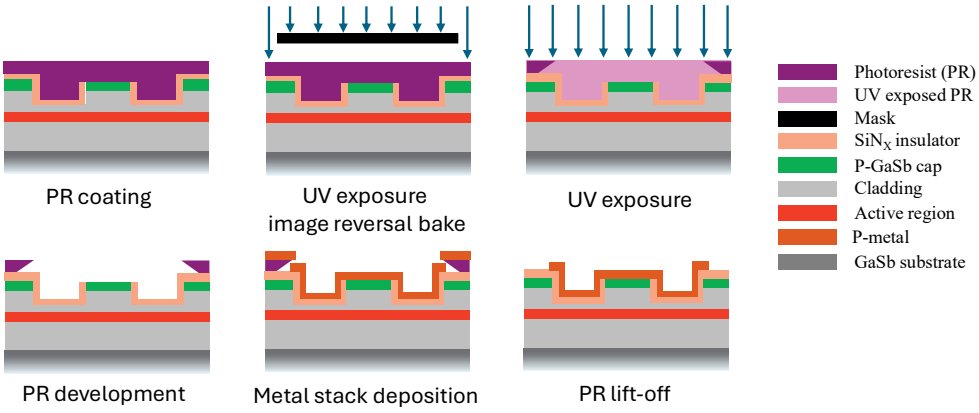


Figure 17. p-metal layer deposition process steps.

Wafer thinning and n-Contact formation: Prior to n-side metallization, the substrate is thinned to ~120 µm to reduce series resistance and facilitate cleaving. Lapping process is performed using chemo-mechanical abrasive, namely aluminum oxide (AlO_x) slurry having 9 µm grain size and then polishing surface with Chemlox.

The n-contact is formed using a Ni/Au/Ge metallization scheme, deposited by electron-beam (E-beam) evaporation. Ni improves adhesion, smoothness, and reproducibility, while Ge diffuses into GaSb during rapid thermal annealing (RTA) to provide doping and reduce contact resistance. In this work, the metal thicknesses are 10 nm Ni / 5 nm Au / 17 nm Ge, followed by an additional 100 nm Au capping layer. The contacts are annealed by rapid thermal annealing at 300°C under N_2 flow.

Dicing bars and AR/HR coating: The sample is cleaved into bars by making small marks (following specific alignment marks) with the diamond tip and applying force using Loomis LSD-100 scriber breaker system. For SLD functionality the bar

facets are AR and HR coated using ion beam sputtering (IBS) system according to the desired functionalities. The coatings are designed using Macleod software utilizing Al_2O_3, SiO_2, and TiO_2 materials. After the designed coatings are deposited at both facets – AR at front and HR at rear, the bars are diced into chips.

Mounting and packaging: For characterization and thermal management, fabricated devices are mounted on aluminum nitride (AlN) submounts. In most cases, chips are bonded to the submount with p-side in the upward direction using silver epoxy. For improved thermal conduction, selected devices are soldered p-side down with indium. Electrical connection to the chip is established by Au wire bonding using a semi-automatic wire bonder. The AlN submount, which acts as a heat spreader, is then attached to a copper heatsink. A thermistor is integrated into the heatsink for temperature monitoring, and the entire assembly is mounted on a thermoelectric Peltier cooler to enable closed-loop temperature control during measurements.

3.3 SLD device characterization

The characterization of SLDs in this research was performed using three principal measurement setups: light–current–voltage (*L–I–V*) characteristics, far-field (FF) emission profiles, and spectral measurements. All measurements were conducted under both CW and pulsed injection conditions at RT, depending on the requirements of the experiment. In the initial stages of this research [P1], SLDs were characterized using a dedicated custom-built platform (“LDC5000”), capable of performing LIV and FF measurements up to emission wavelengths of 2.5 µm.

The system incorporated CW/pulsed current drivers, a calibrated photodetector, and an integrated far-field scanning unit. For subsequent experiments [P2–P3], including RSOAs and gain chips, table-top setups were employed to provide greater flexibility in the measurement configuration. In these setups, devices were mounted on temperature-stabilized submount with thermoelectric (TEC) control, enabling precise thermal regulation during measurements.

The *L–I–V* characterization was used to evaluate the electrical and optical performance of the devices. The diode voltage as a function of injection current provided information on the quality of the heterostructure and metal–semiconductor contacts. To improve accuracy, four-wire sensing was employed for voltage measurements. The optical output power as a function of current provided insight into the internal gain, optical losses, and thermal performance of the active material. For CW injection measurements, a Thorlabs ITC4020 laser diode/TEC controller and a

Keithley 2640B dual-channel source-measure unit were used. Pulsed injection experiments were carried out using a PCX-7410 current driver (Directed Energy, Inc., an IXYS company). Optical power was measured with photodetectors coupled to integrating spheres, with detector selection matching the emission wavelength of the devices under test.

For emission around 2 μm [P1-P2], a Thorlabs InGaAs photodiode (PDA10D2) combined with a Newport diffuse-gold integrating sphere (819C-GL-6) was employed. The far-field (FF) emission profiles were measured by rotating a calibrated detector across the emission cone of the device. These measurements provided information on beam divergence and modal characteristics, which are particularly relevant for SLDs/RSOAs and gain chips where coupling efficiency into external optics is critical. The spectral measurements were performed using optical spectrum analyzers appropriate for the emission wavelength range, enabling the determination of the emission bandwidth, center wavelength, and suppression of longitudinal modes. Temperature stability during all characterization experiments was maintained with a TEC Source meter, which enabled closed-loop control of the submount stage.

3.4 SLD integration into a fiber-based interferometer for time-domain OCT imaging

Fig. 18 shows a 2 μm fiber-based TD-OCT setup based on a Michaelson interferometer configuration employed in non-destructive imaging [P4]. The system utilizes Thorlabs manufactured 50:50 wideband fiber optic coupler (TW2000R5A2B), built for broadband transmission around 2 μm wavelength (2000 ± 200 nm) integrated with SMF-28 Fiber and terminated using FC/APC connector. These couplers are bidirectional and allow any port to be used as an input.

In this setup GaSb-based broadband 2 μm SLD was used as low-coherence light source. The 2 μm broadband SLD device integrated in the setup is 2 mm long and has 5 μm ridge waveguide (with AR/HR coated) and was sub-mounted in epitaxial-layers along upward (p-side-up) configuration while the metallized n-side was bonded to the sub-mount using conductive epoxy-glue, followed by mounting in the butterfly package. The precision lens optics in the 14-pin butterfly package collimates the ASE beam, exiting at the front facet of SLD chip, and guides it into a Corning SMF-28 single mode fiber that has a fiber connector at the other end.

The output of the 2 μm SLD butterfly module injects ASE into one input port of the fiber coupler (FC#1), and the signal splits into two parts: one to the reference arm

and the other to the sample arm. In the sample arm, the light is first collimated towards the scanner via a Thorlabs's RC04APC-P01 protective silver reflective collimator (450 nm – 20 µm) with a focal length of 15 mm. The XY galvo scanners, deflects the beam towards a broadband AR coated (1.65 - 3.0 µm) CaF2 focusing lens L4 (LA5315-D - Ø1/2", plano-convex) with a focal length of 20 mm, which focus the light into the sample. The galvos are positioned in the conjugate plane with the sample. In the reference arm, the 20 mm CaF2 lens L1 collimates the beam, and using the same configuration the light is injected back (through L2) into the fiber. A reference arm translation stage (TSR), movable along Z-axis, in the reference arm path is used with the lens L1 to adjust the optical path difference and axial positioning. The TSR was used to adjust the position by ΔZ to perform B-scans. The light from reference and sample arm is recombined using another 50:50 fiber coupler (FC#2). The TD-OCT configuration employs FC#1 and FC#2 couples to establish a balance detection scheme [64, 82].

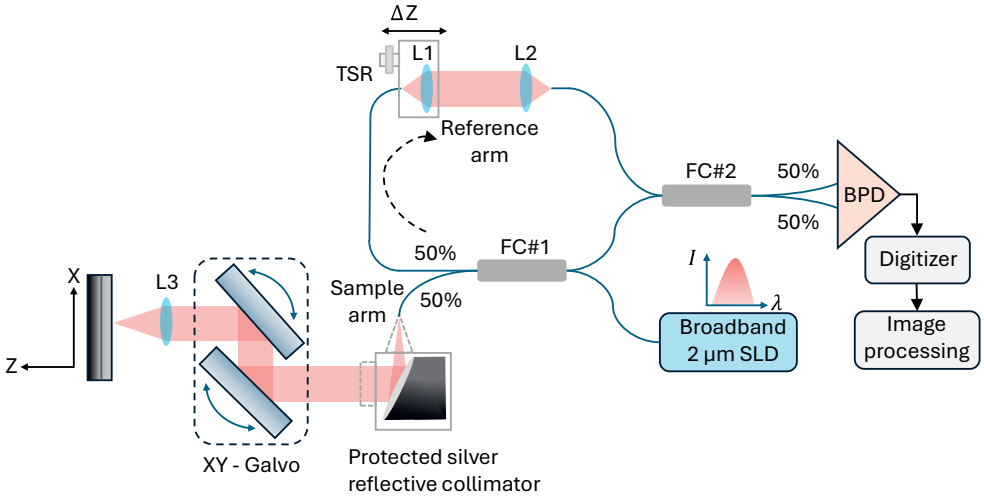


Figure 18. Schematic diagram of TD-OCT setup. Collimating lenses L1–L3 have identical focal lengths of 20 mm, and the protected silver reflective collimator (RC) has a focal length of 15 mm. A translation stage TSR is used in the reference arm path for B-scan. Reproduced from [P4].

The ASE signal is coupled into one arm of the balanced output from the FC#2 are then coupled into the custom-built balanced photodetector (BPD) using Hamamastu G12183-010K extended InGaAs PIN photodiode, with 1 A/W photosensitivity from 1.7 µm to 2.4 µm in wavelength. Length of each fiber arm is approximately 91 cm, in addition to the 50:50 coupler area that contains at least 7.8 cm of the length.

Given the distance between the sample arm terminal to the sample is d, for interference the distance between the launching and injection port in the reference arm should maintain $2d$, and therefore the optical path distance (OPD) in both sample and reference arms is equal. By using the balanced detection scheme, the interferometric signal is enhanced by reducing the common mode noise between the reference and the sample arm [82]. The signal is acquired with a 14-bit digitizer (NI PCI-6132, max 2.5 MS/s per channel) and demodulated to retrieve the fringe envelope.

4 SUMMARY OF RESULTS

This chapter presents the key results obtained from the doctoral research works. The research findings are presented in four peer-reviewed publications. The major focus of the publications has been the development of broadband GaSb-based SLDs operating around 2 μm. First, 2.1 μm broadband SLDs showing the optimization of the device geometry, facet reflectivity, and ASE power were reported in [P1]. The application of dimensionally asymmetric QWs to broaden ASE spectrum bringing specific attention to produce nearly flat gain from the SLD emitter was reported in publication [P2]. Next, in this chapter, the design and optimization of gain in broadband GaSb-based heterostructures operating as an extension of the findings discussed in publication [P3] are presented. Finally, the chapter includes a discussion on experimental demonstrations of fiber interferometer-based OCT imaging at 2 μm wavelength employing our SLDs as broadband light sources [P1]. The work was carried out as a part of the doctoral secondment placed in University of Kent in UK. The OCT imaging results were achieved for the content of publication [P4].

4.1 Power scaling of GaSb-based SLDs operating at 2 μm

In this experiment we have focused on the development of broadband GaSb-based SLDs emitting around 2.1 μm wavelength and explored scaling of power and emission bandwidth for different set of SLD devices. The key focus of this work **[P1]** includes: (i) performing optimization to find trade-offs between emission power in CW mode and corresponding spectral bandwidth, (ii) reducing spectral modulation depth targeting smooth ASE spectra with enhanced performance by optimizing reflectivity of the waveguide facets and the cavity lengths. The active region of the heterostructure employed a pair of QWs which are slightly dimensionally asymmetric while preserving uniform composition.

Fig. 19 shows PL spectra measured from the epitaxial layer structure at low temperature (LT-PL) and near the room temperature. The PL spectra near room temperature (290 K) exhibits a broad emission spectrum with two distinct components at ~2.02 μm and ~2.09 μm with an envelope FWHM of ~140 nm. The

two-component nature of this emission is more distinguishable in LT-PT (~12 K) representing the ground state emission of each of the two QWs at two different wavelength region due to the thickness asymmetry of the wells. The 1.64 μm peak, only visible in LT-PL, originates from the highly tellurium (Te) doped n-GaSb substrate [83].

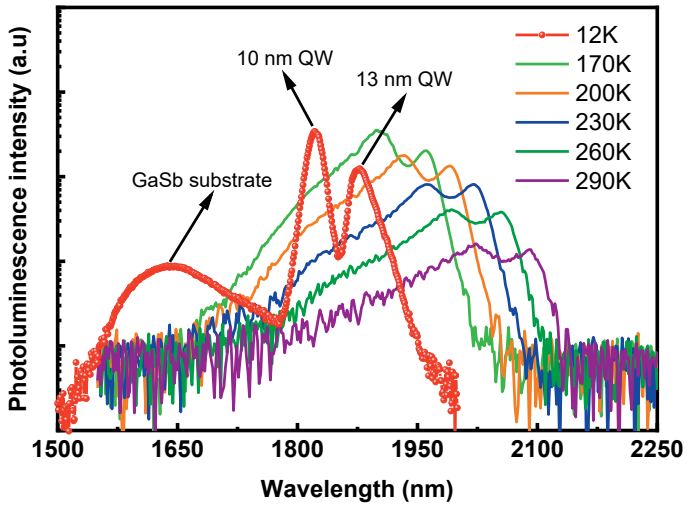


Figure 19. Photoluminescence (PL) spectra of the epitaxial structure from 12 K to 290 K. The measurement was performed after the top clad layer was etched down to ~ 1700 nm [P1].

The wafer was processed into SLD emitters. **Table 3** summarizes the variants of the prepared SLD emitters and their corresponding features. The effective index of fundamental TE mode, n_{eff} was estimated with Harold simulation tool [84] to be ~3.532.

Table 3. SLD types and their design parameters [P1]

SLD types	L (mm)	$L_{straightRWG}$ (mm)	R_{front}(%) / R_{rear}(%)
Type-I	0.8	0	0.01 / As-cleaved (~30)
	1.1	0.15	0.01 / 10
Type-II	2	1.05	0.01 / 0.01
	3	2.05	0.01 / 0.01
Type-III	2	1.05	0.01 / As-cleaved (~30)
	3	2.05	0.5 / 92

Fig. 20 shows the light-current-voltage (*L-I-V*) characteristics of the SLDs measured at RT in CW mode. At low injection current (~100 mA for Type-I and ~200 mA for Type-II and III) the free-space output power slowly increases from the sub-mW to mW-level governed primarily by ASE process. At higher current, gain saturation leads to a sub-linear dependence of the output power with current [85].

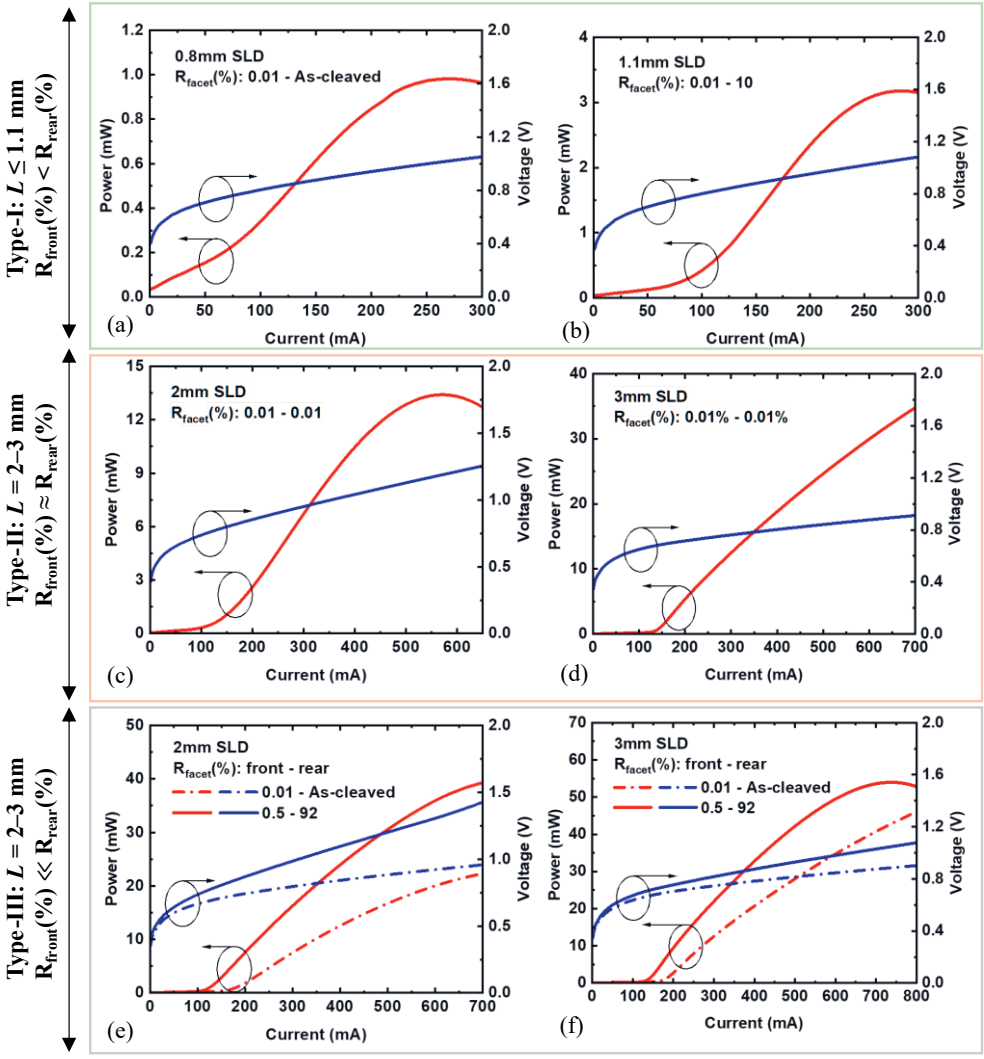


Figure 20. *L-I-V* characteristics of SLDs in CW mode at RT for different facet-reflectivity and cavity lengths: (a, b) Type-I devices (L ≤ 1.1 mm) with AR (~0.01%) front and HR (10%, As-cleaved) rear facets; (c, d) Type-II devices (L = 2-3 mm) with low AR (~0.01%) on both facets; and (e, f) Type-III devices (L = 2-3 mm) with AR (0.01–0.5%) front and HR (As-cleaved or 30%, 92%) rear facets. Reproduced from [P1].

L-I-V characteristics reflect the combined effect of AR coating and 7° tilted ridge near the front facet reduce the modal reflectivity and suppress the cavity resonances. Type-I devices, employing short cavities 0.8-1.1mm with non-identical facet reflectivity (0.01%/10%, As-cleaved) exhibited limited power (~1–3 mW) due to high mirror loss. Type-II devices have identical and low reflectivity (~0.01%) at both facets. However, the curved RWG at front-facet further reduced the effective reflectivity and enabled improved photons out-coupling, yielding ASE power up to ~13 mW and ~35 mW for 2 mm and 3 mm chips, respectively. Type-III devices, combining an AR front-facet and a HR back-facet (≥92%), benefitted from double pass amplification and achieved highest output power of ~56 mW (3mm chip). Inefficient heat sinking due to p-side-up mounting SLD chips and increased non-radiative Auger recombination in shorter cavities have limited power scaling across all the SLD variants.

As shown in **Fig. 21**, increasing the injection current increases the material gain bandwidth and results in broadening ASE spectrum across all SLD devices, with FWHM expanding from ~36 nm to a maximum ~140 nm. The shortest Type-I cavity (L = 0.8 mm), employing its all-curved cavity geometry, delivers the widest ASE bandwidth, exceeding ~114 nm at 150 mA and reaching ~140 nm at 400 mA, with peak emission wavelength shifts from ~2.04 μm to ~2.08 μm. Slightly longer Type-I devices (L = 1.1 mm) exhibit enhanced amplification owing to the increased gain length but accompanied by a reduced spectral bandwidth (~87 nm at 300 mA) as the cavity begins to favor emission near the peak gain region. Type-II devices with AR-coated facets support efficient single-pass ASE with minimal cavity feedback. As a result, 2 mm cavity produces emission bandwidths up to ~108 nm bandwidth while maintaining peak emission between ~2.05–2.1 μm spectral range. In contrast, longer 3 mm cavities favor higher power at the expense of spectral width (~53–64 nm), reflecting stronger gain accumulation. Type-III devices, incorporating HR rear facets, promote double-pass amplification of the ASE signal. While this configuration enhances the optical power, the increased cavity feedback leads to stronger spectral selectivity, resulting in narrower emission bandwidth (~46–70 nm). In these devices, the peak emission wavelength remains injection-tunable from ~2.06 to ~2.12 μm.

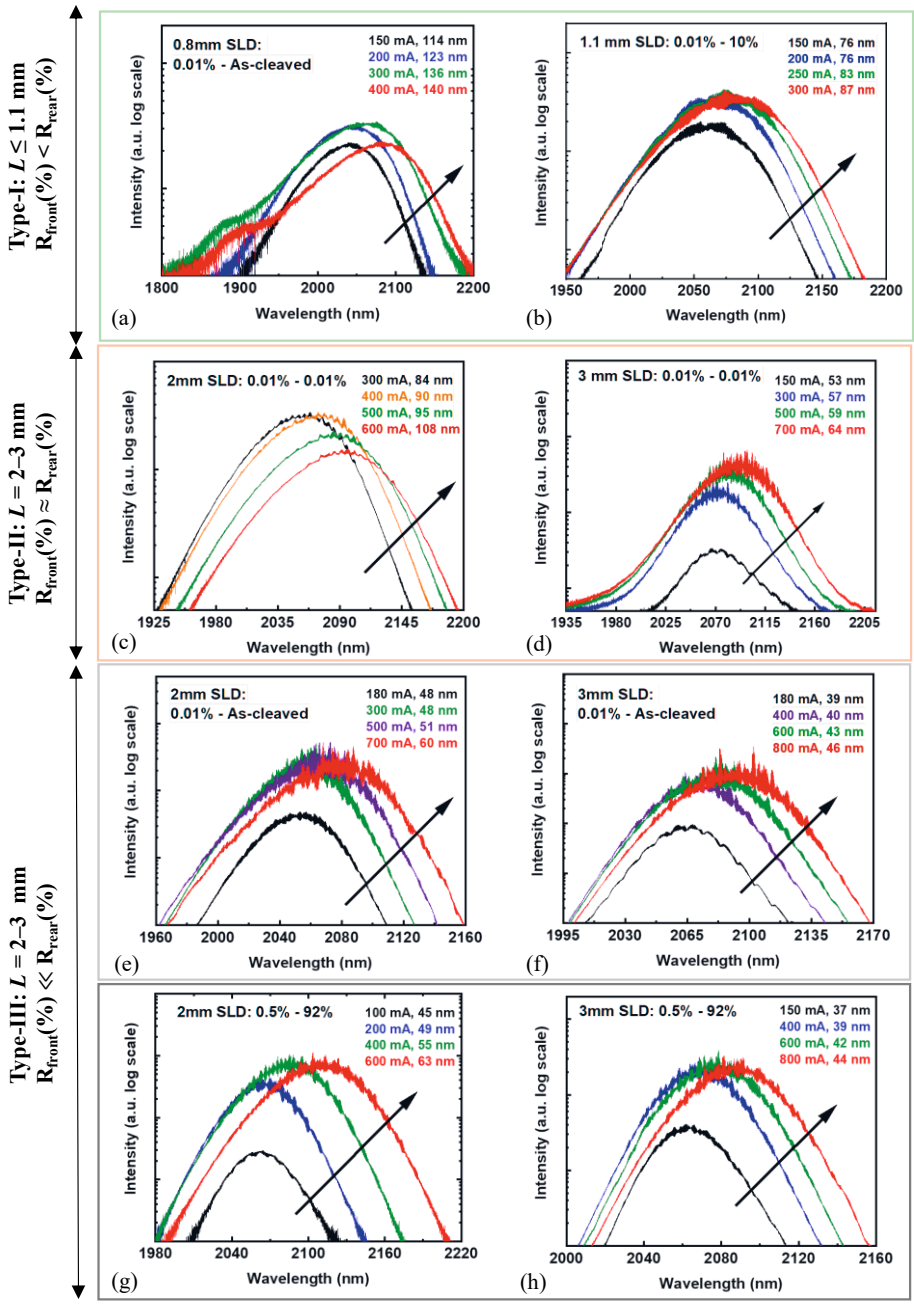


Figure 21. Measured ASE spectra of all types of 2.1 µm SLDs operated at RT in CW mode. Arrows indicate increasing injection current highlighting the current-dependent spectral evolution of the devices. Reproduced from [P1].

The spectral modulation depth (SMD), as shown in **Fig. 22**, reflects the influence of cavity feedback tailored to different levels of facet reflectivity. Type-I short cavities exhibit the lower modulation (~1%), while Type-II devices maintain relatively smooth spectra (~3–7% SMD). In Type-II devices, SMD ranges from ~5% to 25% at drive currents up to ~200 mA but increases rapidly at higher injection current. The observed behavior arises from the combined effect of residual front-facet reflectivity and a highly reflective rear facet. As the modal gain increases with the injection, the effective round-trip amplification enhances the visibility of FP cavity modes within ASE spectrum. This effect is further strengthened by double-pass amplification and becomes more pronounced in longer cavities due to higher accumulations in gain over the propagation length, resulting in increased spectral modulation.

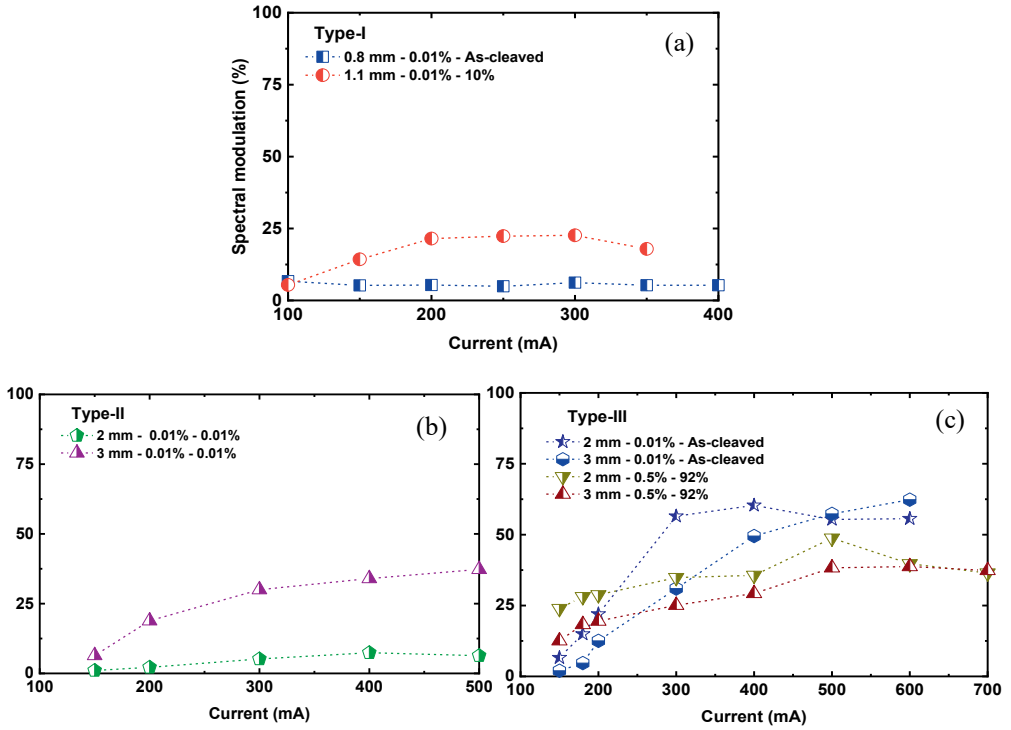


Figure 22. SMD (%) as a function of injection current for (a) Type-I, (b) Type-II, and (c) Type-III SLDs corresponding to emission spectra in Fig. 22. All measurements were conducted at RT in CW mode. Reproduced from [P1].

Fig. 23 shows the key performance trade-off map across the analyzed SLD variants by relating ASE spectral bandwidth (FWHM) recorded at each device's maximum CW output power, with the corresponding injection current and SMD

indicated for each case. The dashed gray curve provides an exponentially decayed trend showing decrease of FWHM with increasing maximum CW power as cavity length and rear-facet reflectivity increased. This turns out SLD chips delivering high output power exhibit narrower emission bandwidths due to longer gain length and reduced mirror loss that increases effective net amplification [68]. Accordingly short-cavity devices (Type-I, $L \leq 1.1$ mm) preserve broader ASE spectra due to reduced gain length and low optical feedback, leaving the broadband emission shaped by asymmetric double QW gain. In contrast, longer cavities (3 mm Type-II, and 2–3 mm Type-III) introduced stronger feedback favoring higher CW power but exhibit narrower spectra consistent with spectral filtering promoting mode selection near the maximum gain region. The accompanying SMD values further confirm the role of cavity feedback. SLD configurations that achieve high-power through longer cavities or higher rear-facet reflectivity consistently exhibit larger spectral modulation. Moreover, the increase in SMD indicates stronger residual cavity effect superimposed on the ASE spectrum.

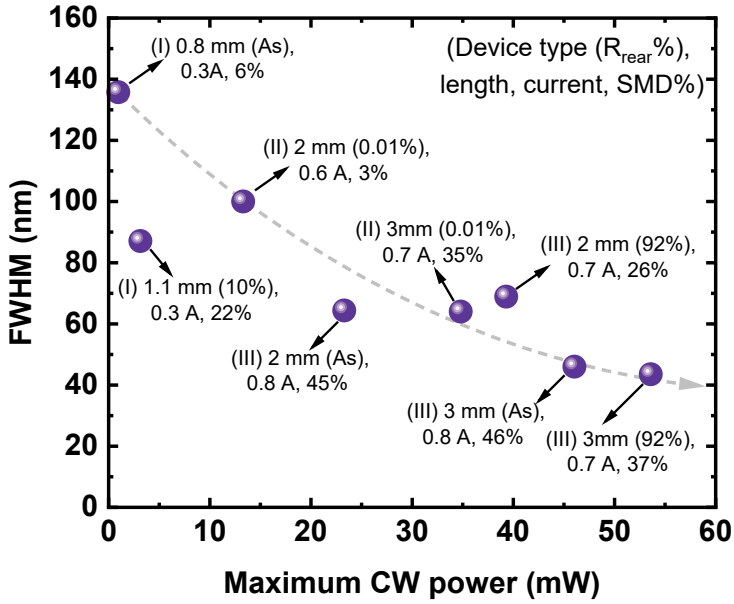


Figure 23. ASE spectral bandwidth (FWHM) at the maximum CW output power for the investigated SLD variants. Each point is annotated with device type, rear-facet reflectivity (R_{rear}%), cavity length, injection current at the maximum-power operating point, and the corresponding spectral modulation depth (SMD). The dashed grey line highlights the overall trade-off between maximum CW power and achievable ASE bandwidth. Reproduced from [P1]

4.2 Broadband heterostructures and amplifier devices in 2 µm wavelength with asymmetric quantum wells

Superluminescent diodes (SLDs) and optical amplifiers operating in 2-3 µm wavelength region demand both: (i) broadband emission and (ii) flat gain, for effective deployment in multi-wavelength spectroscopy [44, 45, 86, 87] and OCT imaging [20, 21, 88]. To this end, we investigated design strategies that exploit dimensionally asymmetric GaInSb/AlGaAsSb quantum wells (QWs) of varying thicknesses. Through careful tailoring of carrier distribution and transition energies across the QWs, we demonstrated broadband optical gain by accessing multiple transitions at specific carrier densities. We have also extensively performed simulations with the Harold multi-physics environment and demonstrated ability to achieve maximum gain bandwidths exceeding 340 nm (FWHM), given the modelling parameters validated against experimental data. The results provide us with a robust framework for the realization of broadband GaSb-based SLDs and amplifiers for SWIR, and mid-IR applications.

4.2.1 Broadband SLD emitter using asymmetric double QWs

In this experiment**,** a GaSb-based SLD emitting around 2 µm wavelength band was realized employing gain engineering in the active region. The key focus of this work [P2] includes: (i) designing a heterostructure with variable-thickness QWs to achieve broadband optical gain through dual energy transitions, (ii) experimentally demonstrating broadband ASE emission with reduced spectral modulation in the 2 µm region, and (iii) investigating the evolution of the emission characteristics at different CW injections and to understand mechanism behind designing a broader gain structure. The active region of the broadband heterostructure employed two $Ga_{0.73}In_{0.27}Sb/Al_{0.27}Ga_{0.73}As_{0.02}Sb_{0.98}$ QWs with identical composition but with a different thickness (7 nm and 13 nm). This design provides two distinct energy transitions within the same active region yielding a broad composite gain spectrum. The QW thicknesses were optimized and selected using Harold laser simulator [75] as a part of engineering the gain bandwidth. Simulation methodology and parameters are already discussed in Ch. 3.

Fig. 24 illustrates the generic bandgap configuration and the computed electronic band structure of the engineered asymmetric DQWs within the gain structure. The band structure displays the conduction (CB) and valence band (VB) profiles, the first

quantized states and their corresponding confined wavefunctions (ψ) for electrons, heavy holes, and light holes (wavefunctions are scaled for visibility). The simulations agree with the transition wavelength and the PL measured data with reasonable accuracy (i.e. E1-HH1 transition) as discussed next.

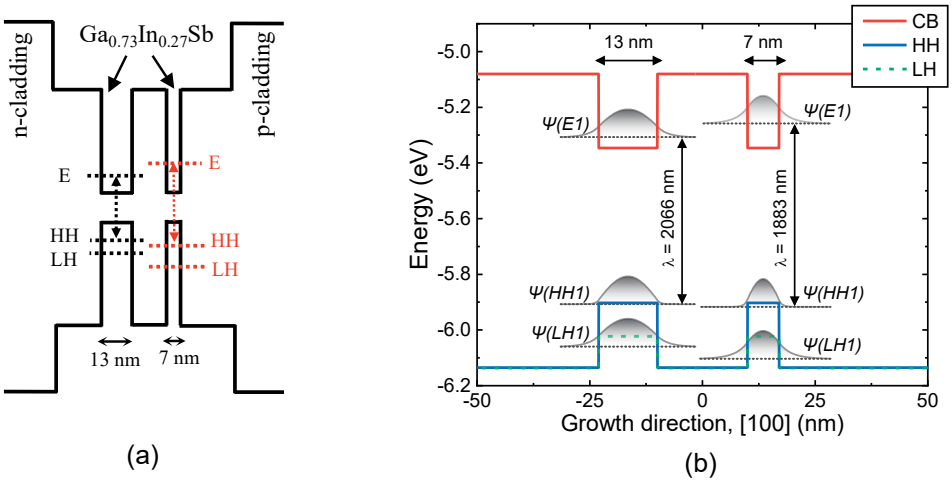


Figure 24. (a) Illustration of the conduction band (top solid black line) and valance band (bottom solid black line) alignment corresponding to the active area (not in scale). The vertical black and red dotted lines in the QWs indicate the lowest energy transition in both QWs. (b) Calculated conduction and valence band profiles of the active region. The first quantized electron $\psi(E1)$, heavy-hole $\psi(HH1)$, and light-hole $\psi(LH1)$ wavefunctions are overlaid. The growth direction axis is centered to the mid-point of the active region between the QWs. Reproduced from [P2].

PL measurements, as shown in **Fig. 25**, were used to confirm that the grown epitaxial design produces two distinct emission components associated with the two QWs. RT-PL from an active-region calibration structure shows a double-peaked spectrum with maxima near ~1923 nm (thinner QW) and ~2078 nm (thicker QW), while the spectrum is partially influenced by atmospheric absorption around ~1.9 µm (greyed-out region). Low-temperature PL (≈12 K) resolves the two contributions more clearly (peaks near ~1713 nm and ~1863 nm) with reduced influence of atmospheric absorption in that measurement condition. In the thesis context, this PL validation provides an experimental anchor for the simulated transition energies discussed in the subsequent section.

The grown epitaxial wafer was processed into 3 mm-long and 5 µm wide RWG devices with a J-shaped geometry (layout and fabrication detailed in Ch. 3). The SLD emitters, in this case, also implemented with 7° curved Euler bend [89] near the front

facet to effectively suppressing the unwanted facet-feedback, and promote ASE dominated operation. The cavity facets were coated to form broadband AR front facet and HR rear facet, supporting enhanced ASE extraction at the AR output while enabling double-pass amplification in the SLD cavity.

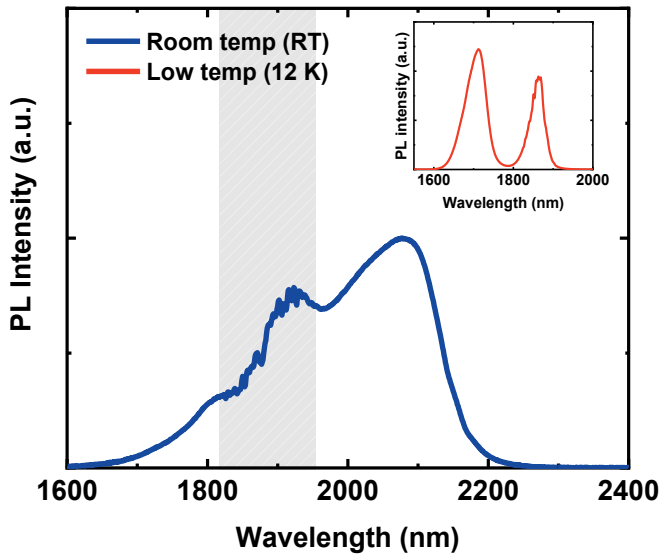


Figure 25. PL spectra of the active region calibration growth structure. The RT-PL spectrum shows two emission components with the thin and thick QWs; the greyed-out portion indicates spectrum influenced by atmospheric absorption near ~1.9 μm. The inset shows the LT-PL (~12 K) spectrum measured from the same heterostructure. Reproduced from [P2].

L-I-V characteristics of the SLD emitter driven in CW mode at RT, are shown in **Fig. 26(a)**. The characteristics indicates three operating regimes: (i) spontaneous emission dominated region up to ~150 mA (CW power ~0.37 mW) with the emission power varies linearly with current, (ii) a rapid power increase between ~150-250 mA associated with switching into linear gain region with output power exponentially increased with current due to stimulated emission, (iii) a more linear dependence above ~250 mA until ~500 mA consistent with onset of gain saturation. Under CW operation at 20°C, the maximum power was ~40 mW at ~900 mA, decreased to ~33 mW at ~50°C. The maximum power level was reduced and shifted to slightly lower current at elevated temperature (consistent with increased carrier leakage and non-radiative recombination and gain saturation at elevated temperature). **Fig. 26(b)** shows the measured *L-I* characteristics under pulsed mode (1% duty cycle, 100 μs).

The measured peak was stable around 70 mW for 1000 mA without any thermal roll-over over the assessed temperature range. The voltage level at a maximum driving current 1000 mA was ~1.08 V and remained stable during all operating temperatures (20°–50°C).

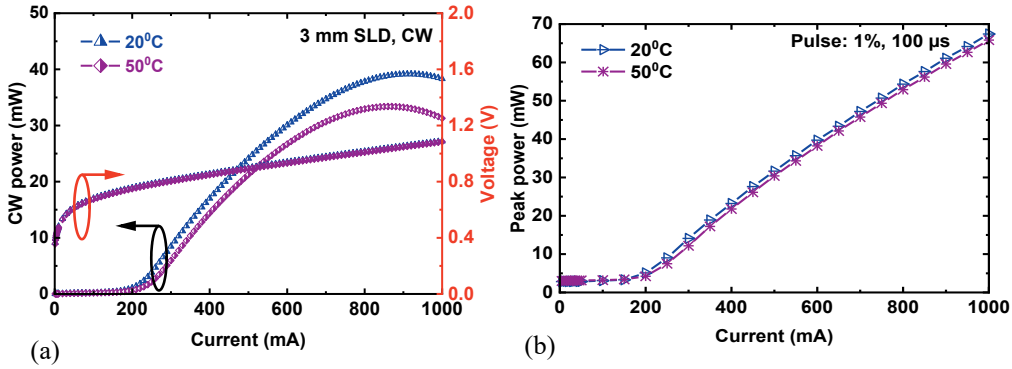


Figure 26. Measured *L–I–V* characteristics of 3 mm J-shaped SLD driven at (a) CW mode, and at (b) Pulse mode (1% duty cycle, 100 µs pulse width) at 20° and 50°C. Reproduced from [P2].

The evolution of SLD emission spectrum with CW injection current is highlighted in **Fig. 27(a).** The measurement was recorded over 150–1000 mA range at RT. Below ASE threshold (<200 mA), emission is dominated at the longer wavelength region (~2.078 µm) corresponds to the ground transition from the 13 nm thick QW. This is due to the carriers initially occupying the lowest-energy states available in the asymmetric double-QW system. At an increased injection level (≥180 mA), carrier population in the thinner 7 nm QW becomes significant, producing emission component at the shorter wavelength region (~1.95 µm). A balanced injection regime is attained at ~200 mA and the magnified view of the corresponding ASE spectrum is shown in **Fig. 27(b)**. At this level, the QWs produces a bimodal emission profile with two dominant peaks near ~1.95 µm and ~2.08 µm, separated by ~130 nm. The peak-to-peak variation between these emission components is approximately ~4 dB. Because the inter-peak dip prevents the use of conventional single-lobe FWHM definition, the emission bandwidth is described by the individual peak widths. FWHM levels of the dominant peaks are ~47 nm (~15 meV) at the shorter-wavelength and ~85 nm (~24 meV) at the longer-wavelength, yields a combined bandwidth of ~132 nm. This situation corresponds to the equalization of the peak gain from both QWs [90]. Within the bias current until ~250 mA, the emission spectra remain bimodal while maintaining several µW/nm spectral power density across ~1920–2120 nm, which is suitable for broadband OCT and spectroscopic sensing

applications [22, 91, 92]. At a higher injection level, the spectral profiles shown in Fig. 29(a) become increasingly dominated by the gain of the thinner QW. The emission therefore narrows and shifts toward shorter wavelengths. For example, at ~400 mA, the dominant emission peak at ~1945 nm exhibits a FWHM of ~38 nm (~12.5 meV) while at 1000 mA the peak slightly red-shifted to ~1970 nm with a FWHM of ~40 nm (~12.8 meV). Despite this narrowing of the main peak, the overall spectral envelope remains relatively broad, with –20 dB bandwidths of ~220 nm at 400 mA and ~152 nm at 1000 mA.

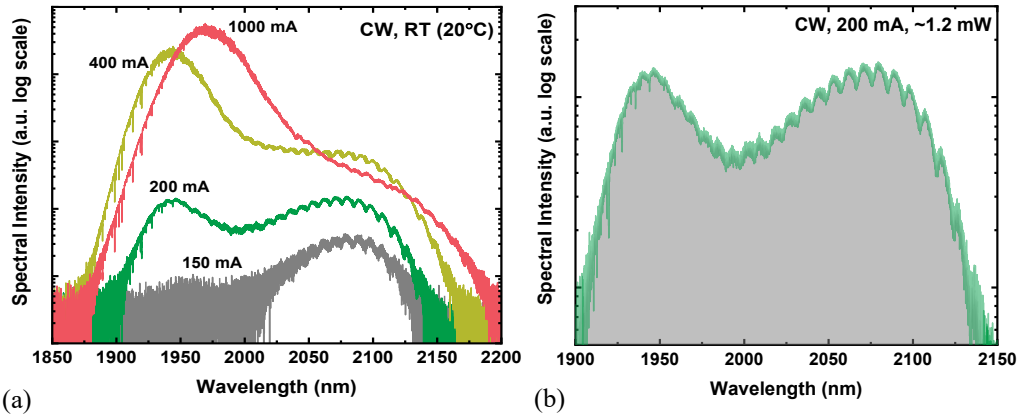


Figure 27. Current dependent SLD's spectra measured at RT in CW mode. (a) ASE spectra for injection currents from 150 mA to 1000 mA; (b) Magnified spectrum at 200 mA highlighting balanced emission from the two QWs and residual Fabry-Pérot modulation. Reproduced from [P2].

4.2.2 Design of broadband gain in heterostructures using asymmetric multiple QWs

In this study [P3], a simulation-validated gain-engineering strategy was exploited to design heterostructures incorporating multiple GaInSb/AlGaAsSb QWs of different thicknesses. The design approach leverages carrier density and transition energy tuning across QWs to access various energy levels tailored to the application of controlled current densities. The validation of the design model is already described in **section 3.1.1**. The study also shows the design and optimization strategy in broadening the emission band by exploiting energy transitions from multiple quantum states. The optimization proceeded in stages to isolate the role of well thickness and to quantify how individual QW contributes to the total gain.

First, single-QW gain structures (see **section 3.1**) were simulated with QW thickness varied from 7 nm to 13 nm with one nm steps. The resulting gain spectra established trends in gain-peak position and bandwidth versus thickness. Then in the second iteration asymmetric DQW structures were simulated with the top QW thickness was fixed to 7 nm and the bottom QW varied in thickness from 7 nm to 13 nm, again with one nm steps, allowing the separate and combined contributions of each well to be evaluated as a function of carrier density. **Fig. 28** showcases the exemplary simulated gain curves at 20°C for SQW and DQW heterostructures. The simulated gain curves showcase distinctive features in the wavelength variation with carrier density, with clear transitions from gain peaks corresponding to E1-HH1 and E1-LH1 transitions in the QWs when carrier density increases.

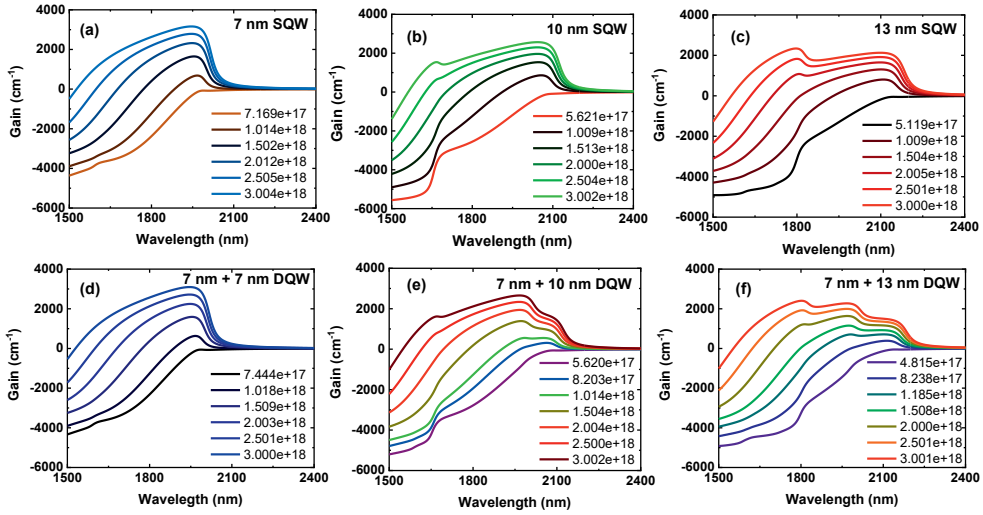


Figure 28. Exemplary gain spectrum of different (a-c) SQWs of thickness 7 nm, 10 nm and 13 nm, and (d-f) DQWs with top QW thickness fixed to 7 nm, and bottom QW thickness of 7 nm, 10 nm, and 13 nm. All legends in the figures show the carrier density level in the QWs. Reproduced from [P3].

Guided by the above discussion, several asymmetric DQW gain responses were further studied to optimize for flat and broad-spectral material gain features at specific carrier densities. **Fig. 29** shows simulated gain spectra having flat gain and wide spectral coverage for a DQW structure with fixed top QW of 7 nm, and bottom QW thickness varied from 9 nm to 13 nm. In all cases, the resulting peak gain associated with the 7 nm QW remains fixed near ~1980 nm, reflecting stronger confinement and higher energy transition from the thinner well. In contrast, the gain peak for second well (thicker) shifts progressively toward longer wavelength as thickness increases,

moving from approximately ~2030 nm to ~2100 nm. When the gain contribution from the two QWs overlaps at an appropriate carrier density, a broad composite gain spectrum was obtained. Simulation showed a maximum gain bandwidth of ~256 nm FWHM was achieved for a combination of 7 nm and 13 nm DQWs at higher carrier density of N=1.2e18 cm^{-3} (corresponds to ~340 mA pulse current injection). Under these conditions, maximum gain of approximately ~710 cm^{-1} is sustained across a wide range from 1953 nm to 2140 nm, while the variation in gain across the overlapping spectral region remains relatively small (~70 cm^{-1}).

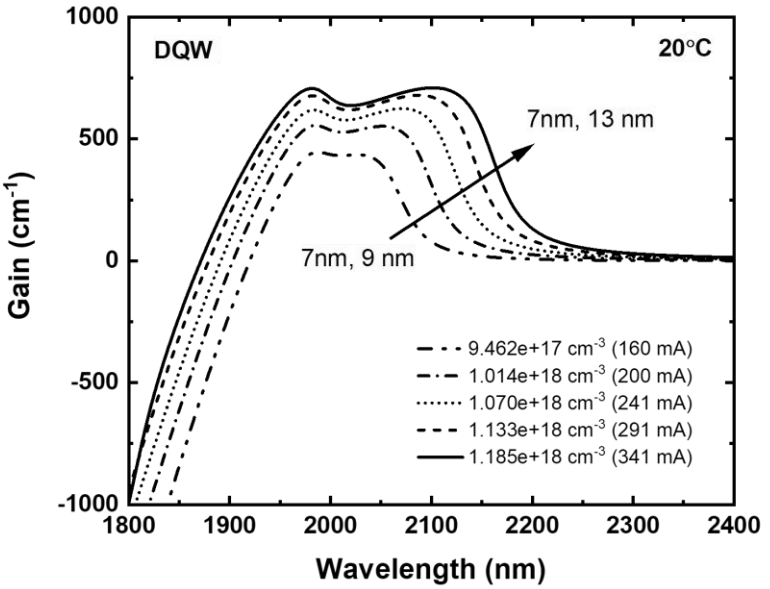


Figure 29. Flat gain spectrum obtained for asymmetric DQW structures with a fixed 7 nm top QW and a bottom QW thickness varied from 9 nm to 13 nm (1 nm increments, indicated by the arrow). The legend denotes the carrier density (cm^{-3}). Reproduced from [P3].

Next, MQW structures employing more than two wells were explored to extend spectral bandwidth and gain beyond the DQW case while constraining the total QW thickness to remain below strain relaxation. In [P3], a particle constrain of about "100% × nm" (total strain-times-thickness) was applied as a rough estimate based on available data for GaInSb [93] and AlGaAsSb [94] strain relaxation when grown on GaSb substrate. MQW designs were then systematically optimized to achieve a balance between spectral flatness and bandwidth (in FWHM) of the gain at high carrier density. Within this framework, **Fig. 30** compares representative designs in terms of flat gain spectra at RT from three different structures: A (reference DQW), B

(A and one additional 13 nm QW), C (one 7 nm and three 13 nm QWs). Compared to structure A, flat gain level was increased in structure B (e.g., from 706 cm^{-1} to 1032 cm^{-1} at elevated carrier density), while structure C produces a broader profile at even higher carrier density level. The maximum material gain level reaches approximately ~1253 cm^{-1}, which is almost two-fold increment compared to reference structure A. For structure C, maximum flat gain level spans approximately ~1950–2135 nm with a gain fluctuation of 73 cm^{-1} in the highlighted flat-gain window. The gain profile also indicates two dominant peaks around ~1987 nm and ~2096 nm and produced a gain profile with maximum ~342 nm FWHM bandwidth (~100 nm broader than structure A) at a carrier density level of ~1.73e18 cm^{-3} (~2.1 A; pulse).

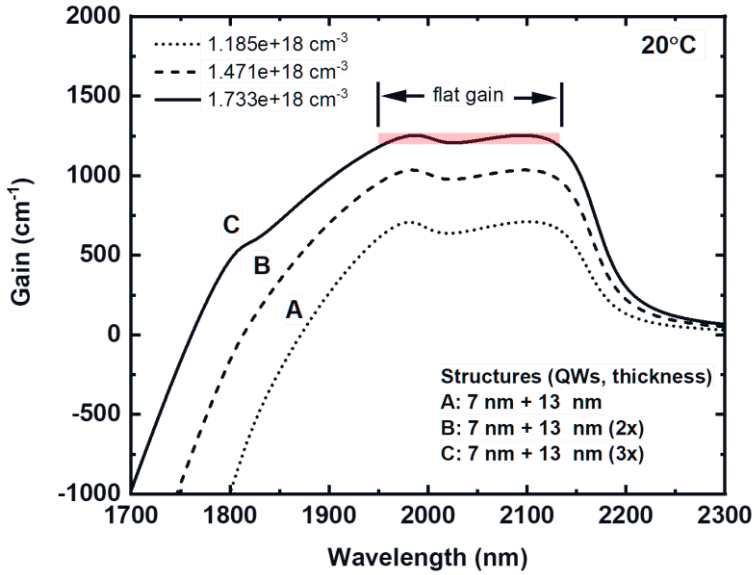


Figure 30. Simulated gain spectra for MQW designs based on two QW thickness classes (7 nm and 13 nm) and uniform composition, illustrating the evolution from the reference DQW design (A) to MQW designs with additional 13 nm QWs (B and C). Reproduced from [P3].

Fig. 31 shows Temperature dependence of the optimized MQW gain profile was also evaluated for structure C between 10°C and 100°C**.** Simulation revealed that increasing temperature modifies the carrier density required to achieve a spectrally flat gain profile. As the temperature increases, the gain peaks exhibited a pronounced red shift. Specifically, the gain peak in the sorter wavelength region shifted from 1970 nm to 2113 nm, while peak corresponding to the longer wavelength region shifted from 2078 nm to 2237 nm. In addition, the FWHM of the gain profile increased from ~335 nm to nearly ~400 nm with increased temperature, indicating spectral

broadening with increased temperature. However, maximum material gain was significantly reduced (~195 cm^{-1}) at higher temperature. This reduction is mainly attributed to increased carrier leakage and reduced carrier confinement in the QWs, commonly observed in semiconductor laser structures at elevated temperatures.

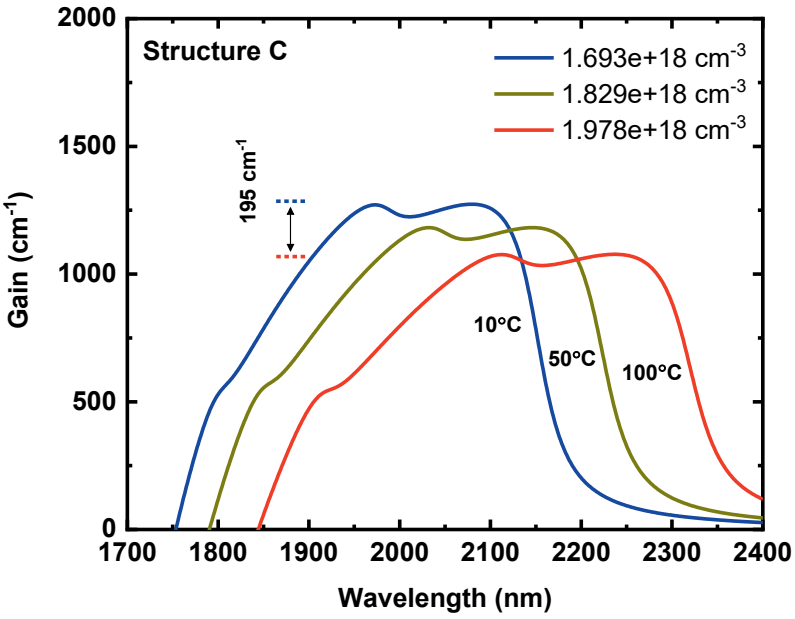


Figure 31. Temperature dependency of the gain spectra for structure C. Reproduced from [P3].

The simulation was also optimized for structure C# (detailed in the main and supplementary section of [P3]) but for a shorter device. Here the length of the active waveguide (current injection region) was reduced from 2 mm to 1775 µm to, while 225 µm of the waveguide end was not pumped to implement a mirror loss of ~95 cm^{-1} without modifying the facet reflectivity. In this case, the gain enhancement is primarily attributed to the contribution of the second quantized state originating from the thicker QW [95], at a carrier density of N=2.412e18 cm^{-3} (~4.4 A in pulse). The fluctuation in gain profile varied approximately ~278 cm^{-1} over a broad spectral window spanning 1760–2150 nm. This optimization yields a gain enhancement of approximately 400–500 cm^{-1} for both thick and thin QWs, respectively.

4.3 Time-domain OCT imaging using 2 μm GaSb SLDs

While most OCT operations are mature and significant advancement has been done for *in vivo* medical diagnosis [5, 56], there is growing interest in imaging non-biological structures exploiting light sources emit at longer wavelengths [23]. OCT in longer spectral region exhibits substantial advantages, as optical scattering coefficients can be assumed to exhibit inverse dependence on wavelength compared to scatterer size in the material media, leading to diminished scattering and enhanced penetration depth compared to shorter wavelengths. SLDs have been extensively used as broadband light source in TD-OCT and SD-OCT systems [56]. Broadband single-mode operation and smoothness in the spectrum of an ASE source are highly desired when integrated into an OCT imaging system.

In this experiment [P4], a GaSb-based SLD light source emitting around 2.05 μm (reported in [P1]) was integrated into a compact, electrically driven, 14-pin fiber-coupled butterfly module. The SLD chip produced a broad ASE spectrum of ~80 nm FWHM bandwidth at 400 mA. *L-I-V* characteristics of the SLD module recorded in CW mode at RT revealed the maximum power at the fiber output was approximately 19.5 mW. In free-space operation, the SLD chip delivered up to ~40 mW of output power, implying an overall coupling efficiency of ~49% in the fiber coupled package. The remaining losses in emission power predicted to multiple factors including artifacts initiating by mode mismatching between the 2 μm ASE beam and the nominal 1.55 μm mode field diameter of the SMF-28 fiber, predicted lens alignment tolerances, and intrinsic losses in the silica-based fiber beyond its optimal transmission window. The SLD's central emission wavelength shifts from ~2065 nm at lower currents (100 mA) to ~2090 nm at higher currents (400 mA), accompanied by a bandwidth (FWHM) increase from ~65 nm to ~83 nm when operating power of minimum ~1 mW to ~10 mW. The measured SMD is limited to ~20% when driven until ~150 mA, however, higher injection yields increased SMD to ~50% at 400 mA.

Fig. 32 shows the coherence features for the Michelson interferometer setup (See **Fig. 18** in section 3.4) when the SLD source is driven at ~150 mA, corresponds to ~2.5 mW power. The coherence envelope's FWHM is approximately ~0.6 mm, implying an axial resolution of about 300 μm in air which is broader than the theoretical axial resolution ~30 μm. This indicates predicted spectral narrowing, side-lobe structure, and fiber-coupling losses influenced the effective coherence function. The side-lobes visible around the main peak are consistent with deviations from an ideal Gaussian source spectrum and lead to secondary maxima in the axial point-spread function (PSF). Despite these effects, the measurement demonstrates the

essential low-coherence operation of the GaSb-based SLD at 2 μm and confirms its suitability as a practical OCT source, where the achievable axial resolution will depend strongly on spectrum shaping and fiber coupling.

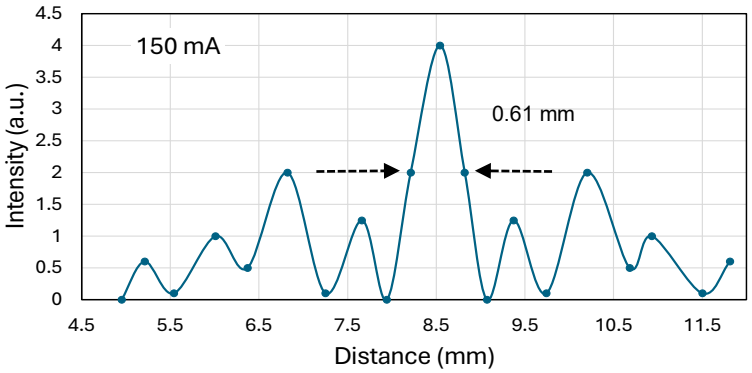


Figure 32. Coherence measurements from the interferometer setup with the SLD biased at 150 mA. Reproduced from [P4].

To demonstrate OCT imaging, a structured test object was prepared with a printed paper containing repeated text “UoK” onto which a thin paint coating (Edding 750 permanent marker) was applied (see **Fig. 33**).

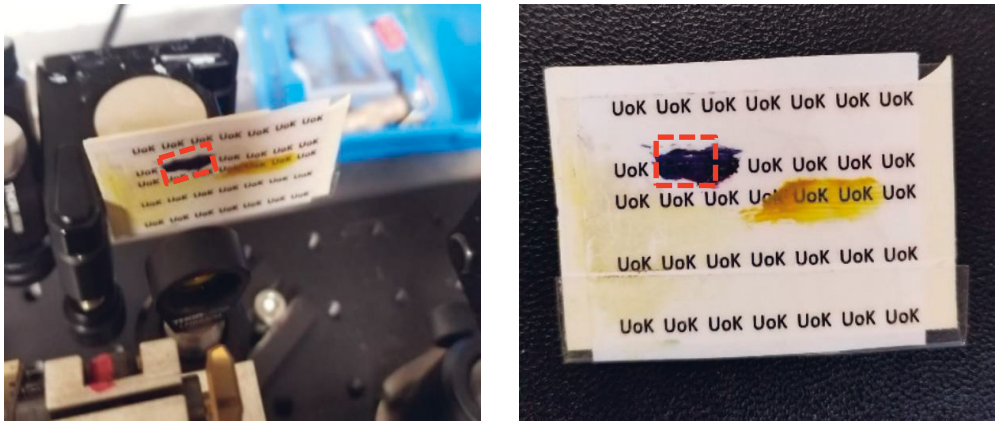


Figure 33. Photograph of the test sample used for OCT scanning. (a) A printed card (4.8 cm x 3.3 cm) with repeated “UoK” text partially covered by a thin paint layer and positioned in the sample arm of the interferometer. (b) Front view photograph of the sample card. The red rectangles in both panels indicate the OCT scanning area. Reproduced from [P4].

The printed pattern provided a high-contrast lateral reference, while the paint introduced scattering and absorption representative of real-world non-biological coatings. The sample was mounted in the dedicated sample arm of the TD-OCT interferometer, positioned on a translation stage to allow controlled alignment and focusing. The probing beam from the fiber collimator was directed onto the card surface (marked with red rectangle) through the microscope objective, ensuring that both the printed features and the overlaying paint were within the optical field of view. This configuration enabled simultaneous evaluation of the system's lateral resolution by imaging the text and its axial sectioning capability by resolving subsurface structures beneath the paint. By combining a structured target with an artificial scattering layer or coatings, the setup offered a controlled yet realistic scenario to benchmark OCT performance before testing on more complex materials.

Fig. 34 (a-b) shows *en-face* OCT slices extracted by fixing the reference delay at two different depths and performing lateral raster-scanning (galvo fast axis, stage slow axis). Fig (a) corresponds to a plane within paint layer, while (b) corresponds to a plane near the printed text (ink/substrate interface). In Fig. (b), the buried printed text appears as bright, high-contrast features against the white paper substrate background due to local refractive-index and absorption differences at the ink–substrate interface. The mottled texture and spatial non-uniformity along the strokes arise from multiple scattering within the pigment coating and small-scale surface roughness introduced during paint application. In longer wavelength, the likelihood of Mie scattering becomes more prominent. Mie scattering has also tendency for forward scattering which reduces the back reflected photons. Thereby, the 2 μm SLD source reduces scattering relative to shorter NIR bands, resulting in improved penetration through the paint coating and enabling clear visualization of the buried print.

Fig. 34(c) shows B-scan image across the same region (see red dashed line in Fig. (b)), and the image is constructed by stitching 200 *en-face* images recorded at successive depths. Axial scanning was performed by translation stage with adjustment of the reference arm accordingly. Two strong reflections from the air/paint and the paint/substrate interfaces are visible. Lateral variations in the spacing between these interfaces indicate non-uniform paint thickness across the scanned area. Below the surface, signal amplitude decays with depth due to combined scattering and material absorption, while shadowing beneath the inked regions further attenuates the backscattered signals.

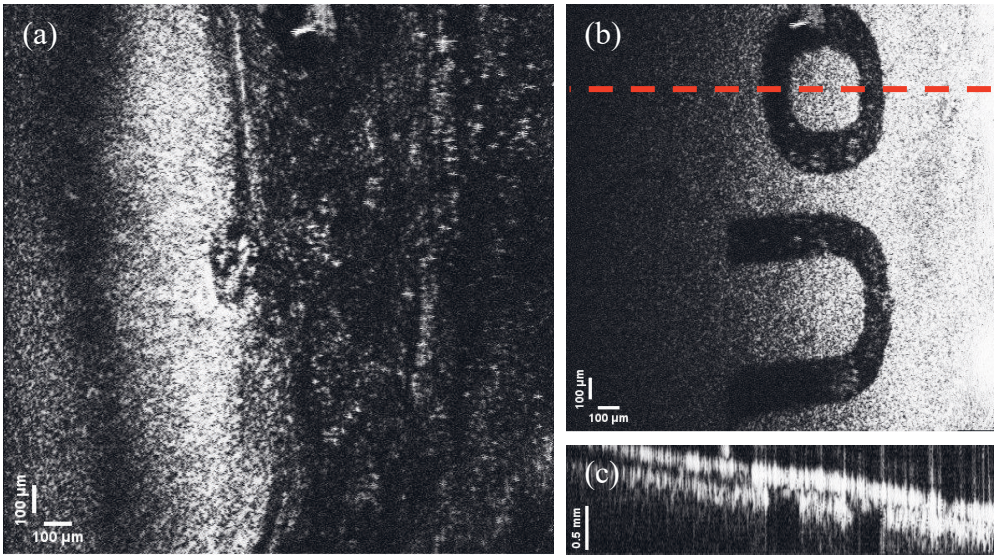


Figure 34. Imaging of "text under paint" by TD-OCT using a ~2.05 µm GaSb SLD source. *En-face* slices at (a) a plane within the paint coating and (b) a plane near the buried print, revealing the "UoK" lettering as bright features beneath the paint. (c) Corresponding B-scan (along the red dashed line in (b)) reveals the air/paint surface and the paint/substrate interface; their varying separation indicates non-uniform paint thickness. Reproduced from [P4].

The *En-face* slices and reconstructed B-scan images together demonstrate the capabilities of TD-OCT imaging at 2 µm. Coherence gating isolates reflections from specific depths, enabling the buried text to be visualized beneath the paint layer. The B-scan provides a geometric representation of the layered structure (surface, paint coating, and substrate) and associated thickness variations. It was predicted that for a paint film with a refractive index of around 1.5–1.6, an air-calibrated resolution of ~29 µm (100 mA, 65 nm FWHM) corresponds to ~19 µm within the material, even improving to ~15 µm when the full spectral bandwidth is utilized (83 nm at 400 mA).

Although experimentally measured resolution did not fully reach these theoretical limits below 150 mA, primarily due to spectral ripple and fiber-coupling effects, the results demonstrate the feasibility of depth-resolved imaging at 2 µm using a GaSb-based SLD module. The reduced scattering facilitates deeper penetration through paint coatings while enabling discrimination of surface and subsurface interfaces. This clearly highlights the potential of semiconductor light sources operating at the SWIR–mid-IR transition (~2 µm) in OCT for non-destructive inspection of multi-layered coatings, polymers and composite materials.

5 CONCLUSIONS AND FUTURE WORK

This doctoral thesis was focused on the development of broadband GaSb-based SLDs operating near the 2 μm wavelength region, targeting advanced Optical Coherence Tomography (OCT). The work addresses a key technological gap between conventional GaAs- and InP-based SLD platforms, which are most mature below 1.7 μm and become increasingly challenging to achieve compact, high-power, broadband emission in the ~2 μm wavelength range. Through a comprehensive approach integrating bandgap engineering, quantum-well design, waveguide optimization, device fabrication, and experimental validation, this work has established a practical and reproducible design pathway for broadband GaSb-based ASE emitters and related photonic devices.

The research began by identifying the limitations of existing OCT light sources and the advantages offered by operating in the 2 μm spectral window. This wavelength regime enables deeper penetration and higher contrast in scattering media, while also opening opportunities in non-biological imaging, polymer inspection, and precision sensing. Despite these advantages, progress in this area has been hampered by the absence of suitable semiconductor sources. The GaSb material system, with its high radiative efficiency and lattice-matched alloy family (GaInSb/AlGaAsSb), provides a versatile foundation for developing broadband devices extending into the mid-IR. This dissertation demonstrates that GaSb, combined with advanced heterostructure design and optimized device geometry, can produce record-broadband and flat-band amplified spontaneous emission (ASE) with high optical power and spectral smoothness.

A major scientific achievement of this work is the introduction of dimensionally asymmetric quantum wells (QWs) as an effective and controllable route to broadband gain engineering. Conventional gain structures often rely on compositional or strain variation to achieve spectral broadening, but such methods can introduce material inhomogeneity and strain relaxation. In this study [P3], broadband heterostructure with one 7 nm thin and three 13 nm thick GaInSb quantum wells, separated by AlGaAsSb barriers, was designed to produce overlapping transitions from distinct confined states. The resulting simulated gain spectra exhibited FWHM values exceeding 340 nm at carrier densities of approximately 1.7×10^{18} cm^{-3}, consistent with

the high-injection regime reached experimentally under pulsed operation, revealing a robust mechanism for spectral flattening and broadening.

This approach offers greater design precision and reproducibility than varying the composition. To this end, we have established a calibrated use of Photon Design's *Harold* model simulation tool for broadband GaSb-based gain structure design. By benchmarking simulated spontaneous emission and gain spectra against experimental photoluminescence and laser-diode data from [P2], the model was validated as an accurate predictive tool within investigated current and temperature ranges. The resulting design framework allows researchers to tune emission characteristics by adjusting QW thicknesses, barrier composition, and cavity geometry before fabrication with reduced experimental iteration and device optimization. The GaSb-based SLD's emission bandwidth [P1-P3] achieved in this dissertation are summarized in **Fig. 35** showing comparison with the representative state-of-the-art results reported in the 1.7–2.6 μm wavelength range.

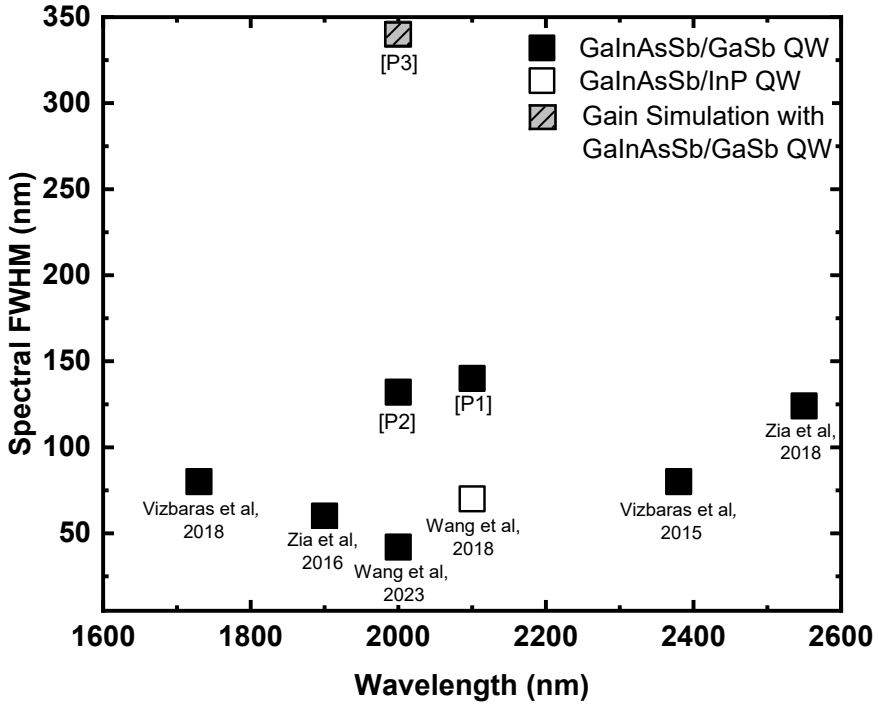


Figure 35. Summary of the SLDs' and simulated gain structure's FWHM bandwidth achieved in this dissertation [P1-P3] together with the state-of-the-art results [45, 86, 96–99] reported in the 1.7–2.6 μm wavelength range. Reproduced from [P2] with additional data from [P1, P3].

The fabricated SLD devices [P1-P2] employed a J-shaped ridge-waveguide geometry, chosen for its ability to minimize optical feedback and suppress lasing while maintaining strong ASE amplification. The curved section disrupts direct reflection into the active region, and facet coatings were tailored to establish asymmetric reflectivity: a broadband AR coating combined with the J-bend reduced effective-reflectivity ($R \approx 10^{-7}$) at the front facet and an HR coating ($R \approx 90$ %) at the rear facet. This configuration supports double-pass ASE without resonant mode formation, thereby combining high optical power with low coherence.

The completed SLDs delivered broadband, high-power emission centered around 2.05 μm. At 200 mA continuous-wave (CW) injection, an ASE bandwidth of approximately 132 nm was obtained (expanding to ~225 nm bandwidth at –20 dB at 1000 mA injection current) which positions it among the widest ASE spectra reported for electrically pumped GaSb-based SLDs near 2 μm. The SLDs achieved CW output powers exceeding 40 mW with a smooth near-Gaussian profile and Fabry–Pérot ripple below 0.2 dB, confirming effective suppression of residual feedback [P2].

The close match between simulated and experimental gain coefficients and internal losses verified the accuracy of the theoretical modeling. Analysis of ASE dependence on cavity length and facet reflectivity established an optimal design trade-off. This synergy between simulation and experiment marks one of the first complete design-to-demonstration validations of a GaSb broadband emitter.

To demonstrate practical utility, the developed SLD was integrated into a fiber-coupled TD-OCT system during the secondment of doctoral research at the University of Kent (UK) [P4]. The GaSb source functioned as a broadband low-coherence emitter in a Michelson interferometer configuration. Regarding the OCT imaging, for a standard paint film with a refractive index of around 1.5–1.6, an air-calibrated resolution of ~29 μm (150 mA, 65 nm FWHM) corresponds to ~19 μm within the material, with further possibility for enhancement to ~15 μm for the wider 83 nm spectrum (400 mA). Despite the fact that these ideal values were not fully attained under the present fiber-coupled implementation at drive currents below 150 mA, the depth-resolved imaging results nonetheless demonstrate the advantages of operating at 2 μm, where reduced scattering supports penetration through paint coatings and coherence gating enables reliable distinction between surface and subsurface interfaces for thickness mapping. The results underscore the significant potential of GaSb broadband emitters for a compact OCT system, with possible extension toward the mid-IR, where deeper penetration and higher contrast are desired.

Overall, this work establishes a complete design-to-demonstration framework encompassing gain engineering, device realization, and system-level validation for GaSb-based broadband emitters. Despite its success, the research also identifies challenges requiring further attention. Power scaling remains constrained by thermal management and gain saturation at high injection currents; improved heat spreading and p-side-down bonding are needed for output levels beyond 100 mW.

Spectral uniformity can be further enhanced through refined AR coatings and possibly through integrated absorber section to suppress residual reflections. Long-term reliability testing over thousands of operating hours is essential to assess device aging, contact diffusion, and oxidation effects.

Concerning packaging, efficient fiber coupling at 2 µm remains non-trivial due to mode-field mismatch and limited component availability, and the effective system bandwidth is therefore reduced compared to the chip-level emission. Addressing these aspects will advance the devices from laboratory prototypes toward deployable modules. The findings open several promising avenues for continued research and technological development:

- Extended wavelength operation: enabling new sensing and spectroscopic applications.
- Advanced cavity engineering: implementation of multiple asymmetric quantum wells may achieve flatter and wider gain spectra.
- High-power and reliability optimization: introducing buried heterostructures, improved thermal paths, and advanced passivation will support long-term stability and higher CW operation levels.
- Packaging and system integration: development of low-loss coupling schemes and ≥2 µm-compatible fiber components to preserve the intrinsic chip-level bandwidth in practical systems.
- Expanded applications: the broadband GaSb platform can be extended to LIDAR, gas sensing, and free-space communication, where its high brightness and mid-IR wavelength access are advantageous.
- OCT system advancement: integration with FD-OCT or SS-OCT architectures could exploit the full spectral potential of these emitters for faster and deeper imaging, although this requires further development of suitable spectrometers and detector technologies at ~2 µm and in extended wavelength range.

6 REFERENCES

1. Huang, D., Swanson, E.A., Lin, C.P., Schuman, J.S., Stinson, W.G., Chang, W., Hee, M.R., Flotte, T., Gregory, K., Puliafito, C.A., Fujimoto, J.G.: Optical Coherence Tomography. Science. 254, 1178–1181 (1991). https://doi.org/10.1126/science.1957169
2. Drexler, W., Fujimoto, J.: State-of-the-art retinal optical coherence tomography. Progress in Retinal and Eye Research. 27, 45–88 (2008). https://doi.org/10.1016/j.preteyeres.2007.07.005
3. Yazdanfar, S., Kulkarni, M.D., Izatt, J.A.: High resolution imaging of in vivo cardiac dynamics using color Doppler optical coherence tomography. Opt. Express. 1, 424–431 (1997). https://doi.org/10.1364/OE.1.000424
4. Elke C. Sattler, Raphaela Kästle, Julia Welzel: Optical coherence tomography in dermatology. Journal of Biomedical Optics. 18, 061224 (2013). https://doi.org/10.1117/1.JBO.18.6.061224
5. Alex, A., Považay, B., Hofer, B., Popov, S., Glittenberg, C., Binder, S., Drexler, W.: Multispectral in vivo three-dimensional optical coherence tomography of human skin. J. Biomed. Opt. 15, 026025 (2010). https://doi.org/10.1117/1.3400665
6. Shimada, Y., Burrow, M.F., Araki, K., Zhou, Y., Hosaka, K., Sadr, A., Yoshiyama, M., Miyazaki, T., Sumi, Y., Tagami, J.: 3D imaging of proximal caries in posterior teeth using optical coherence tomography. Sci Rep. 10, 15754 (2020). https://doi.org/10.1038/s41598-020-72838-2
7. Koller, D.M., Hannesschläger, G., Leitner, M., Khinast, J.G.: Non-destructive analysis of tablet coatings with optical coherence tomography. European Journal of Pharmaceutical Sciences. 44, 142–148 (2011). https://doi.org/10.1016/j.ejps.2011.06.017
8. Zhang, J., Williams, B.M., Lawman, S., Atkinson, D., Zhang, Z., Shen, Y., Zheng, Y.: Non-destructive analysis of flake properties in automotive paints with full-field optical coherence tomography and 3D segmentation. Opt. Express. 25, 18614 (2017). https://doi.org/10.1364/OE.25.018614
9. Stifter, D.: Beyond biomedicine: a review of alternative applications and developments for optical coherence tomography. Applied Physics B. 88, 337–357 (2007). https://doi.org/10.1007/s00340-007-2743-2
10. Optical+Biomedical Engineering Laboratory (OBEL), T.U. of W.A.: Introduction to OCT, https://obel.ee.uwa.edu.au/research/fundamentals/introduction-oct/
11. Yun, S.H., Tearney, G.J., de Boer, J.F., Bouma, B.E.: Motion artifacts in optical coherence tomography with frequency-domain ranging. Opt. Express. 12, 2977–2998 (2004). https://doi.org/10.1364/OPEX.12.002977
12. Nárai, Á., Hermann, P., Auer, T., Kemenczky, P., Szalma, J., Homolya, I., Somogyi, E., Vakli, P., Weiss, B., Vidnyánszky, Z.: Movement-related artefacts (MR-ART) dataset of matched motion-corrupted and clean structural

MRI brain scans. Scientific Data. 9, 630 (2022). https://doi.org/10.1038/s41597-022-01694-8
13. Zeppieri, M., Marsili, S., Enaholo, E.S., Shuaibu, A.O., Uwagboe, N., Salati, C., Spadea, L., Musa, M.: Optical Coherence Tomography (OCT): A Brief Look at the Uses and Technological Evolution of Ophthalmology. Medicina. 59, 2114 (2023). https://doi.org/10.3390/medicina59122114
14. Gora, M.J., Suter, M.J., Tearney, G.J., Li, X.: Endoscopic optical coherence tomography: technologies and clinical applications [Invited]. Biomed. Opt. Express. 8, 2405–2444 (2017). https://doi.org/10.1364/BOE.8.002405
15. Niu, C., Guan, Z., Yu, H., Li, Q., Liu, J., Wu, W., Ma, T., Dai, C.: Endoscopic OCTA in continuous rotation and retraction scheme using a proximal scanning catheter. Opt. Express. 32, 32799 (2024). https://doi.org/10.1364/OE.528684
16. Fujimoto, J.G., Pitris, C., Boppart, S.A., Brezinski, M.E.: Optical Coherence Tomography: An Emerging Technology for Biomedical Imaging and Optical Biopsy. Neoplasia. 2, 9–25 (2000). https://doi.org/10.1038/sj.neo.7900071
17. Bezerra, H.G., Costa, M.A., Guagliumi, G., Rollins, A.M., Simon, D.I.: Intracoronary Optical Coherence Tomography: A Comprehensive Review: Clinical and Research Applications. JACC: Cardiovascular Interventions. 2, 1035–1046 (2009). https://doi.org/10.1016/j.jcin.2009.06.019
18. Kodach, V.M., Kalkman, J., Faber, D.J., van Leeuwen, T.G.: Quantitative comparison of the OCT imaging depth at 1300 nm and 1600 nm. Biomed. Opt. Express. 1, 176–185 (2010). https://doi.org/10.1364/BOE.1.000176
19. Zhu, J., Chong, S.P., Zhou, W., Srinivasan, V.J.: Noninvasive, in vivo rodent brain optical coherence tomography at 2.1 microns. Opt. Lett. 44, 4147 (2019). https://doi.org/10.1364/OL.44.004147
20. Read, M., Cheung, C.S., Liang, H., Meek, A., Korenberg, C.: A Non-invasive Investigation of Egyptian Faience Using Long Wavelength Optical Coherence Tomography (OCT) at 2 μm. Studies in Conservation. 67, 168–175 (2022). https://doi.org/10.1080/00393630.2020.1871208
21. Cheung, C.S., Daniel, J.M.O., Tokurakawa, M., Clarkson, W.A., Liang, H.: High resolution Fourier domain optical coherence tomography in the 2 μm wavelength range using a broadband supercontinuum source. Opt. Express. 23, 1992 (2015). https://doi.org/10.1364/OE.23.001992
22. Cheung, C.S., Daniel, J.M.O., Tokurakawa, M., Clarkson, W.A., Liang, H.: Optical coherence tomography in the 2-μm wavelength regime for paint and other high opacity materials. Opt. Lett. 39, 6509 (2014). https://doi.org/10.1364/OL.39.006509
23. Fu, M.-Y., Yin, Z.-H., Yao, X.-Y., Xu, J., Liu, Y., Dong, Y., Shen, Y.-C.: The Progress of Optical Coherence Tomography in Industry Applications. Adv Devices Instrum. 5, 0053 (2024). https://doi.org/10.34133/adi.0053
24. Kim, S.-H., Kim, J.-H., Kang, S.-W.: Nondestructive defect inspection for LCDs using optical coherence tomography. Displays. 32, 325–329 (2011). https://doi.org/10.1016/j.displa.2011.04.002
25. Cho, N.H., Park, K., Kim, J.-Y., Jung, Y., Kim, J.: Quantitative assessment of touch-screen panel by nondestructive inspection with three-dimensional real-time display optical coherence tomography. Optics and Lasers in Engineering. 68, 50–57 (2015). https://doi.org/10.1016/j.optlaseng.2014.12.013
26. Shirazi, M.F., Park, K., Wijesinghe, R.E., Jeong, H., Han, S., Kim, P., Jeon, M., Kim, J.: Fast Industrial Inspection of Optical Thin Film Using Optical

Coherence Tomography. Sensors. 16, 1598 (2016). https://doi.org/10.3390/s16101598
27. Wolfgang, M., Peter, A., Wahl, P., Markl, D., Zeitler, J.A., Khinast, J.G.: At-line validation of optical coherence tomography as in-line/at-line coating thickness measurement method. International Journal of Pharmaceutics. 572, 118766 (2019). https://doi.org/10.1016/j.ijpharm.2019.118766
28. Lawman, S., Liang, H.: High precision dynamic multi-interface profilometry with optical coherence tomography. Appl. Opt. 50, 6039–6048 (2011). https://doi.org/10.1364/AO.50.006039
29. Haida Liang, Borislava Peric, Michael Hughes, Adrian Gh. Podoleanu, Marika Spring, Stefan Roehrs: Optical Coherence Tomography in archaeological and conservation science - a new emerging field. Presented at the Proc.SPIE December 30 (2008). https://doi.org/10.1117/12.819499
30. Nazari, A., Sadr, A., Saghiri, M.A., Campillo-Funollet, M., Hamba, H., Shimada, Y., Tagami, J., Sumi, Y.: Non-destructive characterization of voids in six flowable composites using swept-source optical coherence tomography. Dental Materials. 29, 278–286 (2013). https://doi.org/10.1016/j.dental.2012.11.004
31. Gliścińska, E., Sankowski, D., Krucińska, I., Gocławski, J., Michalak, M., Rowińska, Z., Sekulska-Nalewajko, J.: Optical coherence tomography image analysis of polymer surface layers in sound-absorbing fibrous composite materials. Polymer Testing. 63, 194–203 (2017). https://doi.org/10.1016/j.polymertesting.2017.08.011
32. Liu, P., Groves, R.M., Benedictus, R.: 3D monitoring of delamination growth in a wind turbine blade composite using optical coherence tomography. NDT & E International. 64, 52–58 (2014). https://doi.org/10.1016/j.ndteint.2014.03.003
33. Madruga, F.J., Sfarra, S., Real, E., Gargiulo, G., Conde, O.M., López-Higuera, J.M.: Complementary Use of Active Infrared Thermography and Optical Coherent Tomography in Non-destructive Testing Inspection of Ancient Marquetries. Journal of Nondestructive Evaluation. 39, 39 (2020). https://doi.org/10.1007/s10921-020-00683-4
34. Liang, H., Cid, M.G., Cucu, R.G., Dobre, G.M., Podoleanu, A.Gh., Pedro, J., Saunders, D.: En-face optical coherence tomography - a novel application of non-invasive imaging to art conservation. Opt. Express. 13, 6133–6144 (2005). https://doi.org/10.1364/OPEX.13.006133
35. Dickmann, K., Fotakis, C., Asmus, J.F. eds: Lasers in the conservation of artworks: LACONA V proceedings, Osnabrück, Germany, Sept. 15-18, 2003. Springer, Berlin ; New York (2005)
36. Israelsen, N.M., Petersen, C.R., Barh, A., Jain, D., Jensen, M., Hannesschläger, G., Tidemand-Lichtenberg, P., Pedersen, C., Podoleanu, A., Bang, O.: Real-time high-resolution mid-infrared optical coherence tomography. Light Sci Appl. 8, 11 (2019). https://doi.org/10.1038/s41377-019-0122-5
37. Su, R., Kirillin, M., Chang, E.W., Sergeeva, E., Yun, S.H., Mattsson, L.: Perspectives of mid-infrared optical coherence tomography for inspection and micrometrology of industrial ceramics. Opt. Express. 22, 15804–15819 (2014). https://doi.org/10.1364/OE.22.015804

38. Duelk, M., Hsu, K.: SLEDs and Swept Source Laser Technology for OCT. In: Drexler, W. and Fujimoto, J.G. (eds.) Optical Coherence Tomography: Technology and Applications. pp. 527–561. Springer International Publishing, Cham (2015)
39. Chen, S., Li, W., Zhang, Z., Childs, D., Zhou, K., Orchard, J., Kennedy, K., Hugues, M., Clarke, E., Ross, I., Wada, O., Hogg, R.: GaAs-Based Superluminescent Light-Emitting Diodes with 290-nm Emission Bandwidth by Using Hybrid Quantum Well/Quantum Dot Structures. Nanoscale Research Letters. 10, 340 (2015). https://doi.org/10.1186/s11671-015-1049-2
40. Maximov, M.V., Gordeev, N.Yu., Shernyakov, Y.M., Kornyshov, G.O., Beckman, A.A., Payusov, A.S., Mintairov, S.A., Kalyuzhnyy, N.A., Kulagina, M.M., Zhukov, A.E.: Superluminescent Diodes Based on Chirped InGaAs/GaAs Quantum Well-Dot Layers. Photonics. 10, 1090 (2023). https://doi.org/10.3390/photonics10101090
41. Gu, Y., Zhang, Y., Cao, Y., Zhou, L., Chen, X., Li, H., Xi, S.: 2.4 μm InP-based antimony-free triangular quantum well lasers in continuous-wave operation above room temperature. Applied Physics Express. 7, 032701 (2014). https://doi.org/10.7567/APEX.7.032701
42. Lyutetskii, A.V., Pikhtin, N.A., Slipchenko, S.O., Sokolova, Z.N., Fetisova, N.V., Leshko, A.Yu., Shamakhov, V.V., Andreev, A.Yu., Golikova, E.G., Ryaboshtan, Yu.A., Tarasov, I.S.: 1.7–1.8 μm Diode lasers based on quantum-well InGaAsP/InP heterostructures. Semiconductors. 37, 1356–1362 (2003). https://doi.org/10.1134/1.1626224
43. Belenky, G., Shterengas, L., Kisin, M.V., Hosoda, T.: Gallium antimonide (GaSb)-based type-I quantum well diode lasers: recent development and prospects. In: Semiconductor Lasers. pp. 441–486. Elsevier (2013)
44. Vizbaras, K., Dvinelis, E., Šimonytė, I., Trinkūnas, A., Greibus, M., Songaila, R., Žukauskas, T., Kaušylas, M., Vizbaras, A.: High power continuous-wave GaSb-based superluminescent diodes as gain chips for widely tunable laser spectroscopy in the 1.95–2.45 μm wavelength range. Applied Physics Letters. 107, 011103 (2015). https://doi.org/10.1063/1.4926367
45. Zia, N., Viheriälä, J., Koivusalo, E., Virtanen, H., Aho, A., Suomalainen, S., Guina, M.: GaSb superluminescent diodes with broadband emission at 2.55 μm. Applied Physics Letters. 112, 051106 (2018). https://doi.org/10.1063/1.5015974
46. Ojanen, S., Viheriälä, J., Zia, N., Koivusalo, E., Hilska, J., Tuorila, H., Guina, M.: Widely Tunable (2.47–2.64 μm) Hybrid Laser Based on GaSb/GaInAsSb Quantum-Wells and a Low-Loss Si3N4 Photonic Integrated Circuit. Laser & Photonics Reviews. 17, 2201028 (2023). https://doi.org/10.1002/lpor.202201028
47. Alam Bhuiyan, I.K., Hilska, J., Peil, M., Viheriälä, J., Guina, M.: Broadband continuous-wave GaSb-based superluminescent diodes emitting at 2.1 μm. AIP Advances. 15, 085015 (2025). https://doi.org/10.1063/5.0281496
48. Bhuiyan, I.K.A., Hilska, J., Peil, M., Viheriälä, J., Guina, M.: Broadband 2-μm superluminescent diodes with GaSb-based variable-thickness quantum wells. Applied Physics Letters. 127, 163307 (2025). https://doi.org/10.1063/5.0283821
49. Bhuiyan, I.K.A., Hilska, J., Peil, M., Viheriälä, J., Guina, M.: Design of broadband optical gain in GaSb-based heterostructures with asymmetric

quantum wells. Opt. Express. 33, 54154–54165 (2025). https://doi.org/10.1364/OE.575782
50. Shterengas, L., Kipshidze, G., Hosoda, T., Liang, R., Feng, T., Wang, M., Stein, A., Belenky, G.: Cascade Pumping of 1.9–3.3 μm Type-I Quantum Well GaSb-Based Diode Lasers. IEEE J. Select. Topics Quantum Electron. 23, 1–8 (2017). https://doi.org/10.1109/JSTQE.2017.2687763
51. Hosoda T., Kipshidze G., Shterengas L., Belenky G.: Diode lasers emitting near 3.44 μm in continuous-wave regime at 300K. Electronics Letters. 46, 1455–1457 (2010). https://doi.org/10.1049/el.2010.2564
52. Rouillard, Y., Genty, F., Pérona, A., Vicet, A., Yarekha, D.A., Boissier, G., Grech, P., Baranov, A.N., Alibert, C.: Edge and vertical surface emitting lasers around 2.0–2.5 μm and their applications. Philosophical Transactions of the Royal Society of London. Series A: Mathematical, Physical and Engineering Sciences. 359, 581–597 (2001). https://doi.org/10.1098/rsta.2000.0744
53. Y. Rouillard, S. Belahsene, M. Jahjah, G. Boissier, P. Grech, G. Narcy, A. Vicet, L. Naehle, M. v. Edlinger, M. Fischer, J. Koeth: Quantum well lasers emitting between 3.0 and 3.4 μm for gas spectroscopy. Presented at the Proc.SPIE January 20 (2012). https://doi.org/10.1117/12.905881
54. Fujimoto, J.G., Drexler, W.: Introduction to OCT. In: Drexler, W. and Fujimoto, J.G. (eds.) Optical Coherence Tomography: Technology and Applications. pp. 3–64. Springer International Publishing, Cham (2015)
55. Latychevskaia, T.: Lateral and axial resolution criteria in incoherent and coherent optics and holography, near- and far-field regimes. Appl. Opt. 58, 3597–3603 (2019). https://doi.org/10.1364/AO.58.003597
56. Drexler, W., Fujimoto, J.G.: Optical Coherence Tomography. Technology and Applications. Springer International Publishing, Berlin, Germany (2015)
57. Jacques, S.L.: Optical properties of biological tissues: a review. Phys. Med. Biol. 58, R37–R61 (2013). https://doi.org/10.1088/0031-9155/58/11/R37
58. S. Grelet, A. M. Jiménez, R. D. Engelsholm, P. B. Montague, A. Podoleanu: 40 MHz Swept-Source Optical Coherence Tomography at 1060 nm Using a Time-Stretch and Supercontinuum Spectral Broadening Dynamics. IEEE Photonics Journal. 14, 1–6 (2022). https://doi.org/10.1109/JPHOT.2022.3226820
59. Kopp, F., Eichler, C., Lell, A., Tautz, S., Ristić, J., Stojetz, B., Höß, C., Weig, T., Schwarz, U.T., Strauss, U.: Blue Superluminescent Light-Emitting Diodes with Output Power above 100 mW for Picoprojection. Japanese Journal of Applied Physics. 52, 08JH07 (2013). https://doi.org/10.7567/JJAP.52.08JH07
60. Zorin, I., Gattinger, P., Prylepa, A., Heise, B.: Time-encoded mid-infrared Fourier-domain optical coherence tomography. Opt. Lett. 46, 4108–4111 (2021). https://doi.org/10.1364/OL.434855
61. Colley, C.S., Hebden, J.C., Delpy, D.T., Cambrey, A.D., Brown, R.A., Zibik, E.A., Ng, W.H., Wilson, L.R., Cockburn, J.W.: Mid-infrared optical coherence tomography. Review of Scientific Instruments. 78, 123108 (2007). https://doi.org/10.1063/1.2821609
62. Charsley, J.M., Farrell, C., Rutkauskas, M., Schunemann, P.G., Reid, D.T.: Mid-infrared optical coherence tomography with a stabilized OP-GaP optical parametric oscillator. Opt. Lett. 49, 2882–2885 (2024). https://doi.org/10.1364/OL.520734

63. Marschall, S., Andersen, P.E.: Optical coherence tomography. In: Semiconductor Lasers and Diode-based Light Sources for Biophotonics. pp. 409–446
64. Podoleanu, A.Gh.: Unbalanced versus balanced operation in an optical coherence tomography system. Appl. Opt. 39, 173–182 (2000). https://doi.org/10.1364/AO.39.000173
65. Takada, K., Himeno, A., Yukimatsu, K.: Phase-noise and shot-noise limited operations of low coherence optical time domain reflectometry. Applied Physics Letters. 59, 2483–2485 (1991). https://doi.org/10.1063/1.105981
66. Ling Wang, Rongzhen Fu, Chen Xu, Mingen Xu: Methods and applications of full-field optical coherence tomography: a review. Journal of Biomedical Optics. 27, 050901 (2022). https://doi.org/10.1117/1.JBO.27.5.050901
67. Alphonse, G.A., Gilbert, D.B., Harvey, M.G., Ettenberg, M.: High-power superluminescent diodes. IEEE J. Quantum Electron. 24, 2454–2457 (1988). https://doi.org/10.1109/3.14376
68. Gerard A. Alphonse: Design of high-power superluminescent diodes with low spectral modulation. Presented at the Proc.SPIE April 16 (2002)
69. Lu, H., Alkhazragi, O., Wang, Y., Almaymoni, N., Yan, W., Gunawan, W.H., Lin, H., Park, T.-Y., Ng, T.K., Ooi, B.S.: Low-coherence semiconductor light sources: devices and applications. npj Nanophoton. 1, 9 (2024). https://doi.org/10.1038/s44310-024-00005-w
70. Vurgaftman, I., Meyer, J.R., Ram-Mohan, L.R.: Band parameters for III–V compound semiconductors and their alloys. Journal of Applied Physics. 89, 5815–5875 (2001). https://doi.org/10.1063/1.1368156
71. Donati, G.P., Kaspi, R., Malloy, K.J.: Interpolating semiconductor alloy parameters: Application to quaternary III–V band gaps. Journal of Applied Physics. 94, 5814–5819 (2003). https://doi.org/10.1063/1.1613371
72. Schubert, E.F.: Light-Emitting Diodes. Cambridge University Press, Cambridge (2006)
73. Corzine, S.W., Yan, R.-H., Coldren, L.A.: Chapter 1 - OPTICAL GAIN IN III–V BULK AND QUANTUM WELL SEMICONDUCTORS. In: Zory, P.S. (ed.) Quantum Well Lasers. pp. 17–96. Academic Press, San Diego (1993)
74. Roux, S., Barritault, P., Lartigue, O., Cerutti, L., Tournié, E., Gérard, B., Grisard, A.: Mid-infrared characterization of refractive indices and propagation losses in GaSb/AlXGa1−XAsSb waveguides. Applied Physics Letters. 107, 171901 (2015). https://doi.org/10.1063/1.4934702
75. HAROLD by Photon Design (2023). [Online], https://photond.com/harold
76. M. Asada, A. Kameyama, Y. Suematsu: Gain and intervalence band absorption in quantum-well lasers. IEEE Journal of Quantum Electronics. 20, 745–753 (1984). https://doi.org/10.1109/JQE.1984.1072464
77. Piprek, J.: Semiconductor optoelectronic devices : introduction to physics and simulation. Academic Press, Amsterdam ; Tokyo (2003)
78. Varshni, Y.P.: Temperature dependence of the energy gap in semiconductors. Physica. 34, 149–154 (1967). https://doi.org/10.1016/0031-8914(67)90062-6
79. Al-Muhanna, A., Salhi, A.: Numerical analysis of InGaAs–InP multiple-quantum well laser emitting at 2 μm. Opt Quant Electron. 46, 851–861 (2014). https://doi.org/10.1007/s11082-013-9796-8
80. Chenini, L., Aissat, A., Halbwax, M., Vilcot, J.P.: Performance simulation of an InGaSb/GaSb based quantum well structure for laser diode applications.

Physics Letters A. 467, 128711 (2023). https://doi.org/10.1016/j.physleta.2023.128711
81. Salhi, A., Al-Muhanna, A.A.: Self-Consistent Analysis of Quantum Well Number Effects on the Performance of 2.3-μm GaSb-Based Quantum Well Laser Diodes. IEEE J. Select. Topics Quantum Electron. 15, 918–924 (2009). https://doi.org/10.1109/JSTQE.2008.2012000
82. A F Fercher, W Drexler, C K Hitzenberger, T Lasser: Optical coherence tomography - principles and applications. Reports on Progress in Physics. 66, 239 (2003). https://doi.org/10.1088/0034-4885/66/2/204
83. Bignazzi, A., Bosacchi, A., Magnanini, R.: Photoluminescence study of heavy doping effects in Te-doped GaSb. Journal of Applied Physics. 81, 7540–7547 (1997). https://doi.org/10.1063/1.365297
84. HAROLD by Photon Design. (2023), https://photond.com/products/harold.htm
85. Boeck, J., Amann, M.-C.: AlGaAs/GaAs Double-Heterostructure Superluminescent Diodes for Optical Transmission Systems. Frequenz. 33, 278–283 (1979). https://doi.org/10.1515/FREQ.1979.33.10.278
86. Vizbaras, A., Šimonytė, I., Miasojedovas, A., Trinkūnas, A., Bučiūnas, T., Greibus, M., Naujokaitė, G., Torcheboeuf, N., Droz, S., Boiko, D., Dambrauskas, Ž., Gulbinas, A., Vizbaras, K.: Swept-wavelength lasers based on GaSb gain-chip technology for non-invasive biomedical sensing applications in the 1.7–2.5 μm wavelength range. Biomed. Opt. Express. 9, 4834 (2018). https://doi.org/10.1364/BOE.9.004834
87. Ojanen, S., Viheriälä, J., Zia, N., Koivusalo, E., Hilska, J., Tuorila, H., Guina, M.: Discretely Tunable (2594, 2629, 2670 nm) GaSb/Si3N4 Hybrid Laser for Multiwavelength Spectroscopy. Laser & Photonics Reviews. 17, 2300492 (2023). https://doi.org/10.1002/lpor.202300492
88. Liang, H., Lange, R., Peric, B., Spring, M.: Optimum spectral window for imaging of art with optical coherence tomography. Applied Physics B. 111, 589–602 (2013). https://doi.org/10.1007/s00340-013-5378-5
89. Cherchi, M., Ylinen, S., Harjanne, M., Kapulainen, M., Aalto, T.: Dramatic size reduction of waveguide bends on a micron-scale silicon photonic platform. Opt. Express. 21, 17814–17823 (2013). https://doi.org/10.1364/OE.21.017814
90. Wang, J., Hamp, M.J., Cassidy, D.T.: Design Considerations for Asymmetric Multiple Quantum Well Broad Spectral Width Superluminescent Diodes. IEEE J. Quantum Electron. 44, 1256–1262 (2008). https://doi.org/10.1109/JQE.2008.2003104
91. Akcay, C., Parrein, P., Rolland, J.P.: Estimation of longitudinal resolution in optical coherence imaging. Appl. Opt. 41, 5256 (2002). https://doi.org/10.1364/AO.41.005256
92. Ko, T.H., Adler, D.C., Fujimoto, J.G., Mamedov, D., Prokhorov, V., Shidlovski, V., Yakubovich, S.: Ultrahigh resolution optical coherence tomography imaging with a broadband superluminescent diode light source. Opt. Express. 12, 2112 (2004). https://doi.org/10.1364/OPEX.12.002112
93. Nilsen, T.A., Breivik, M., Selvig, E., Fimland, B.O.: Critical thickness of MBE-grown Ga1−xInxSb (x<0.2) on GaSb. Journal of Crystal Growth. 311, 1688–1691 (2009). https://doi.org/10.1016/j.jcrysgro.2008.11.083
94. Lazzari, J.L., Fouillant, C., Grunberg, P., Leclercq, J.L., Joullié, A., Schiller, C.: Critical layer thickness in AlGaAsSbGaSb heterostructures determined by

X-ray diffraction. Journal of Crystal Growth. 130, 96–100 (1993). https://doi.org/10.1016/0022-0248(93)90840-S
95. Mehuys D., Mittelstein M., Yariv A., Sarfaty R., Ungar J.E.: Optimised Fabry-Perot (AlGa)As quantum-well lasers tunable over 105 nm. Electronics Letters. 25, 143–145 (1989). https://doi.org/10.1049/el:19890104
96. Wang, D., Zhang, J., Hou, C., Zhao, Y., Cheng, F., Jia, X., Zhai, S., Zhuo, N., Liu, J., Liu, F., Wang, Z.: High performance continuous-wave InP-based 2.1 μ m superluminescent diode with InGaAsSb quantum well and cavity structure suppression. Applied Physics Letters. 113, 161107 (2018). https://doi.org/10.1063/1.5052056
97. Zia, N., Viheriälä, J., Koivusalo, E., Guina, M.: High-power single mode GaSb-based 2 µm superluminescent diode with double-pass gain. Applied Physics Letters. 115, 231106 (2019). https://doi.org/10.1063/1.5127407
98. Wang, T., Yang, C., Chen, Y., Shi, J., Yu, H., Su, X., Zhang, Y., Zhao, Y., Tong, C., Wu, D., Xu, Y., Ni, H., Niu, Z.: High power GaSb-based superluminescent diode with cascade cavity suppression waveguide geometry and ultra-low antireflection coating. Applied Physics Letters. 123, 021102 (2023). https://doi.org/10.1063/5.0157235
99. Zia, N., Viheriälä, J., Koskinen, R., Aho, A., Suomalainen, S., Guina, M.: High power (60 mW) GaSb-based 1.9 μ m superluminescent diode with cavity suppression element. Applied Physics Letters. 109, 231102 (2016). https://doi.org/10.1063/1.4971972

PUBLICATIONS

PUBLICATION I

Broadband continuous-wave GaSb-based superluminescent diodes emitting at 2.1 μm

Ifte Khairul Alam Bhuiyan, Joonas Hilska, Markus Peil, Jukka Viheriälä, Mircea Guina

AIP Advances **15** (8), 085015 (2025)
DOI: 10.1063/5.0281496

Publication is licensed under a Creative Commons Attribution 4.0 International License CC-BY

Broadband continuous-wave GaSb-based superluminescent diodes emitting at 2.1 μm

Cite as: AIP Advances 15, 085015 (2025); doi: 10.1063/5.0281496
Submitted: 19 May 2025 • Accepted: 31 July 2025 •
Published Online: 13 August 2025

View Online Export Citation CrossMark

Ifte Khairul Alam Bhuiyan,[a] Joonas Hilska, Markus Peil, Jukka Viheriälä, and Mircea Guina

AFFILIATIONS

Optoelectronics Research Centre, Physics Units, Tampere University, Korkeakoulunkatu 3, 33720 Tampere, Finland

[a]Author to whom correspondence should be addressed: ifte.alambhuiyan@tuni.fi

ABSTRACT

We report development of GaSb-based superluminescent diodes (SLDs) emitting around 2.1 μm wavelength for applications in sensing and non-destructive imaging benefitting from broad and smooth spectra with low modulation depth ripples. Record-large spectral bandwidth is reported by exploiting an asymmetric type-I double quantum well InGaSb/AlGaAsSb active region. Preventing lasing from such gain structures while enhancing the amplified stimulated emission and mitigating the spectral modulation is essential. To this end, we employ J-waveguide chip architecture and perform a systematic study of the influence of facet's reflectivity orienting the SLD chip's p-side in upward direction. Broad emission with a full width at half maximum spectrum of ≥140 nm [corresponds to ~1 mW in continuous wave (CW) power] and minimal ripples is reported, which is a nearly twofold increase in emission bandwidth compared to the previous reports in this spectral region. We also report SLD devices that can deliver a maximum output power of 56 mW for a limited bandwidth of ~45 nm at room temperature in CW operation.

© 2025 Author(s). All article content, except where otherwise noted, is licensed under a Creative Commons Attribution (CC BY) license (https://creativecommons.org/licenses/by/4.0/). https://doi.org/10.1063/5.0281496

17 March 2026 11:11:27

In the realm of light sources, superluminescent diodes (SLDs) have emerged with a unique positioning, merging attributes found in laser diodes (LDs) and light-emitting diodes (LEDs). An SLD emits partially coherent broadband light such as an LED, while exploiting amplified stimulated emission (ASE) effects and exhibiting similar brightness and beam directionality as an LD.[1,2] The SLD operation requires suppression of optical feedback to prevent the onset of lasing and to yield a relatively low temporal coherence.

SLDs have played a pivotal role as a light source in optical coherence tomography (OCT)[3] enabling high-resolution cross-sectional imaging, particularly in retinal diagnosis[4] and cardiology.[5] In fiber optic gyroscopes (FOGs),[6] SLDs serve as stable light sources for precise navigation systems used in aerospace and defense.[7,8] Due to their reduced coherence noise[9] in broad emission, SLDs are widely used in accurate measurement in optical sensing,[10,11] metrology, and interferometry.[12,13] Moreover, SLDs are integral to applications in spectroscopy,[14] where their spectral properties facilitate material characterization and chemical analysis. Their compact size, reliability, and efficiency further extend their utility to visible optical communication systems[15] and forensic inspection.[16,17]

Mid-infrared (mid-IR) light sources emitting around 2–3 μm wavelength regions are more and more sought after due to the potential applications in gas and liquid sensing using molecular absorption spectroscopy,[18] noninvasive imaging in dentistry,[19,20] or archeology[21] using OCT.[22,23] The development of 2 μm SLDs has only recently gained a higher level of attention,[14,24–27] yet without focusing on enlarging the optical bandwidth or ensuring smooth spectrum, which are essential features for applications, especially for OCT imaging. To fabricate such broadband light sources, the GaSb-based semiconductor InGaSb/AlGaAsSb material system has emerged as an attractive candidate with the ability to cover the mid-IR wavelength range 2–3 μm and beyond.[28–32]

Leading results have been concentrated on the development of GaSb-based SLDs emitting around 2 μm wavelength with optimized emission power in CW operation at room temperature (RT). The optimization mostly showcased cavity design geometry, passive absorbing section, and facet coatings without improving the spectral width and the smoothness of the spectrum, which are critical in OCT measurement. Notably, Vizbaras *et al.*[14] demonstrated single-angled-facet ridge-waveguide (RWG) SLD devices emitting (i) 40 mW power at 2.05 μm with over 40 nm full width at half maximum (FWHM), (ii) 10 mW power at 2.25 μm with 80 nm FWHM, and (iii) 5 mW power at 2.4 μm with over 80 nm FWHM. At 1.9 μm wavelength, Zia *et al.*[24] reported an SLD-device with a

© Author(s) 2025

60 nm broad spectrum with 60 mW power collected from a single-pass tapered waveguide terminated through an unpumped cavity suppression (CS) section. Another CS technique was presented by Wang *et al.*,[25] for SLDs emitting at 2.1 μm, which utilized a 5.4 mm long spiral cavity coupled to a tilted tapered RWG, resulting in emission of a maximum power of 30 mW with on average a 70 nm FWHM. Employing an unpumped-CS section in J-shaped double-pass gain geometry, the emission power at 2 μm wavelength was further improved by Zia *et al.*[26] demonstrating an output power of 120 mW with a 43 nm FWHM. Furthermore Wang *et al.*[27] demonstrated cascaded cavity geometry to increase the power to record 152 mW at 2 μm wavelength with about 42 nm FWHM. For the above-mentioned devices, the SLD chips were bonded to the submount through indium evaporation in p-side down configuration, enabling effective heat sinking to maintain increased saturation power. Despite these advancements, there is a lack of investigations to address concerns of (i) trade-offs between emission power and emission bandwidth, (ii) flattening the gain ripples in the spectrum, and (iii) facet reflectivities, in connection with cavity length for a specific device geometry.

In this report, we present the development of broadband GaSb-based SLDs emitting around 2.1 μm wavelength. We have employed an asymmetric double quantum well (QW) active region[33–37] to substantially widen the emission spectrum and used a J-shaped double-pass RWG geometry, which promotes ASE while preventing lasing. Furthermore, the role of coatings at the waveguide facets was systematically investigated. All SLD chips were mounted in p-side-up orientation and specific devices could deliver more than 56 mW output in CW (emission FWHM limited to ~45 nm) at RT. In addition, some other SLDs configured with increased mirror losses, exhibited stable single transverse mode emission, with FWHMs exceeding 140 nm and mW-level output power.

The epitaxial layer structure of the GaSb-based SLDs was designed using the commercial simulation tool Harold.[38] The epitaxial structure was grown by solid-source molecular beam epitaxy on a 2 in. n-GaSb(100) substrate. The active region included two compressively strained $In_{0.28}Ga_{0.72}Sb$ type-I QWs with different thicknesses of 10 and 13 nm, which were separated by a 20 nm thick $Al_{0.26}Ga_{0.74}As_{0.02}Sb_{0.98}$ barrier. The QWs were sandwiched by lattice matched 130 nm thick $Al_{0.26}Ga_{0.74}As_{0.02}Sb_{0.98}$ layers forming the WG core. The WG core was further sandwiched by two thick lattice matched $Al_{0.49}Ga_{0.51}As_{0.04}Sb_{0.96}$ cladding layers on either side with opposite doping. The n-side cladding layer was doped to ~3×10^{17} cm^{-3}, while the p-cladding layer was p-doped to ~6×10^{18} cm^{-3}, with the doping being graded down around inner 500 nm around the WG core. The p-cladding was overgrown by a 200 nm p-GaSb cap layer that was highly p-doped (~3×10^{19} cm^{-3}). Figure 1(a) presents the epitaxial structure. Figure 1(b) shows photoluminescence (PL) spectra measured from the epitaxial layer structure after etching down the top-cladding by ~1700 nm to allow for more efficient excitation with the 532 nm laser, which strongly absorbs the n-GaSb buffer and cladding layers. The PL spectra near room temperature (290 K) exhibit a broad emission spectrum with two distinct components at ~2.02 and ~2.09 μm with an envelope FWHM of ~140 nm. The two-component nature of this emission is revealed more clearly in low temperature PL (LT-PL) measurements, especially at a temperature of ~12 K. Each of these components corresponds to the ground state emission of each of the two QWs, with the thicker QW emitting at a longer wavelength given its lower confinement potential. In addition, LT-PL revealed emission peaking at 1.64 μm, originating from the highly tellurium (Te) doped n-GaSb substrate.[39]

The fundamental concept behind designing the SLDs waveguide aims at ensuring a single-mode transverse operation and high output power with efficient ASE, while minimizing the reflection from the facets to avoid lasing and ensure a smooth optical spectrum. To this end, we have chosen a J-shaped ridge waveguide RWG architecture, as shown in Fig. 2. The front-facet (green) on the right-hand side (used as the main output) had a low reflectivity, while the reflectivity of the back-facet (red) on the left-hand side was used as a tailoring parameter for controlling the trade-off between the output power and ASE on the one hand, and the FP-related spectral ripples on the other hand. The epitaxial wafer was processed into SLD chips with different cavity lengths (L) of 3, 2, 1.1, and 0.8 mm. The curved section of the RWG had an Euler-bend geometry,[40] a length of 0.95 mm ($L_{curved\ RWG}$), and ended with a 7° tilted ridge section at

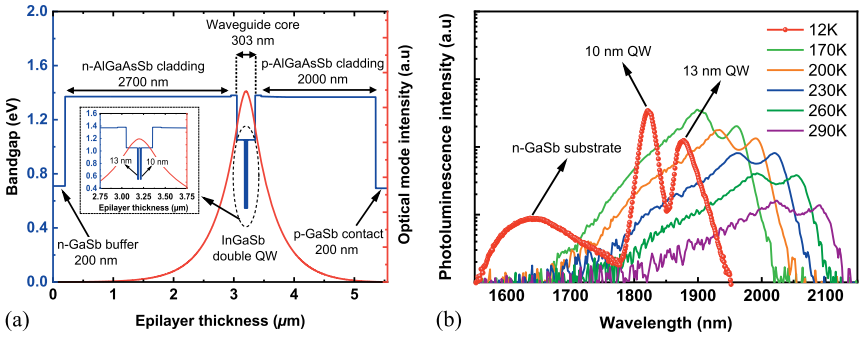


FIG. 1. (a) Epitaxial layer structure showing layer thickness, bandgap, and optical mode intensity. (b) Photoluminescence (PL) spectra of the epitaxial structure from 12 to 290 K. The measurement is performed after the top clad layer was etched down to ~1700 nm.

17 March 2026 11:11:27

© Author(s) 2025

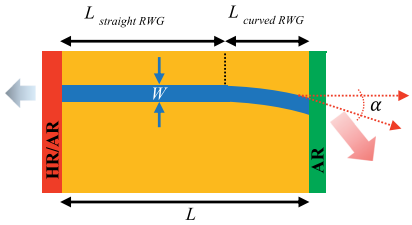


FIG. 2. Schematic of J-shaped SLD cavity geometry. The front facet was coated with anti-reflective (AR) coating and the rear facet is coated with high reflective (HR) or anti-reflective (AR) dielectric coating.

the front facet. The straight section of the waveguide was terminated at the back-facet of the chips and had a variable length ($L_{straight\ RWG}$). The smallest chip with L = 0.8 mm was all-curved and without any straight section near the rear facet.

To study the interplay between reflectivity of the facets, we applied a set of thin film dielectric coatings on the back- and front-facets with designed broad reflection bands from 1.9 to 2.3 μm. The dielectric coatings consisted of a stack of SiO_2 and TiO_2 and were deposited by ion-beam sputtering (IBS). The anti-reflective (AR) dielectric coatings had designed target power reflectivity (R%) values of 0.5%–0.01% and were first deposited to the front-facets of all processed SLD chips. Then, the dielectric mirrors changing from a low reflectivity of ~0.01% to values as high as ~90% were deposited to the back-facets of the SLDs. Due to technical limitations, it was not possible to apply different HR coatings at the rear facets of 0.8 and 1.1 mm long cavities. Table I summarizes the design features defining the waveguide architecture, where in the effective index of fundamental TE mode, the n_{eff} parameter was estimated from the Harold simulation tool.[38]

SLD chips from each type of devices were operated in CW for light–current–voltage (L–I–V) characteristics at RT. Exemplary measurements are shown in Fig. 3. At an injection current of up to 100 mA (in case of type-I) and 200 mA (in case of type-II and type-III), the SLD's free-space output power slowly increases in the sub-mW and mW-level dominated by the ASE process. After these levels, gain saturation deteriorates linearity of the output characteristic, yielding a sub-linear dependence of the output power with the current.[41] Double pass amplification occurs for the devices with a combination of broadband AR dielectric coatings at the front-facets and higher value of back-facet mirror reflectivity of ~10%, ~30% (as-cleaved facet, i.e., with no coatings) and HR ≥90%. The use of AR coating and the 7° tilted ridge are essential to reduce the modal reflectivity and suppress the appearance of FP cavity resonances.

TABLE I. SLD types and their design parameters.

SLD types	L (mm)	$L_{straight\ RWG}$ (mm)	R_{front}(%)/R_{rear}(%)
Type-I	0.8	0	0.01/as-cleaved (~30)
	1.1	0.15	0.01/10
Type-II	2	1.05	0.01/0.01
	3	2.05	0.01/0.01
Type-III	2	1.05	0.01/as-cleaved (~30)
	3	2.05	0.5/92

Depending on the cavity lengths and facet-reflectivities, the SLDs are broadly categorized into three types. Type-I SLDs are short cavities with non-identical facet reflectivity (AR ~0.01%, HR ~10%, 30%). In this case, the loss coefficient associated with the back-facet mirror is the highest, and in consequence, the output power was limited to ~1 and ~3 mW for devices with L of 0.8 and 1.1 mm, respectively. In case of type-II SLDs, the dielectric coatings at the two facets have identical and low reflectivities (AR ≈ HR ~0.01%). However, the front-facet with the 7° tilted RWG has lower reflectivity and allows more photons to be out-coupled compared to the rear-facet. Such SLD configuration produces a much higher level of ASE output power, i.e., ~13 mW in case of 2 mm chips and ~35 mW in cases of 3 mm SLD chips. Type-III SLDs have an AR front-facet and a HR back-facet allowing some of the generated photons within the RWG to experience a double-pass amplification process. In this type of SLDs, the maximum CW power in free-space was ~56 mW at RT recorded for 3 mm AR (~0.5%) and HR (≥92%). Due to SLD's p-side-up orientation on the submount, heat sinking in the active region of epi-layers was not efficient. Moreover, shorter cavity suffers with nonradiative Auger recombination due to higher threshold carrier density ($R_{auger} \sim CN^3$). Thereby, linear power scaling was not possible to maintain among all device variants despite the temperature controller was stable at ~20 °C (RT).

Figure 4 shows the emission spectra of all types of SLDs measured using a Yokogawa AQ6375 optical spectrum analyzer (OSA) with a resolution of 0.1 nm under CW injection at 20 °C. An increase in injection current increases the material gain bandwidth and produces a broader ASE spectrum. Across all devices at all injection currents, the FWHM increases from a minimum of ~36 nm to a maximum ~140 nm. For all types of devices, the percentage of spectral modulation depth (SMD) is low at a low injection current near the threshold where ASE process starts. The SMD parameter (m_s) is calculated based on the standard formula $m_s = \left(\frac{I_{max}-I_{min}}{I_{max}+I_{min}}\right)$%, where I_{max} and I_{min} denote maximum and minimum intensity in the emission spectrum, respectively.[42] In Fig. 5, calculated spectral modulation depth, m_s (%), from all types of SLDs are presented.

Figure 4(a) shows that a type-I short cavity device (L = 0.8 mm) is an all curved SLD cavity that produces the broadest ASE spectrum with a very low ~1% SMD, as shown in Fig. 5(a). In this device, the maximum CW power ~1 mW is recorded for an injection current of 300 mA. This short cavity device produces an ASE spectrum more than 114 nm broad at a very low current of ~150 mA with central emission wavelength around 2.04 μm and could be injection tuned to maximum 2.08 μm with a ~140 nm FWHM broad spectrum at 400 mA. The other short cavity device (L = 1.1 mm) shown in Fig. 4(b) contains a 0.15 mm straight RWG section at the rear facet (10% HR) and produces slightly more amplification. For an injection of 300 mA, the device generates an 87 nm FWHM broad ASE spectrum around 2.08 μm, corresponding to a maximum power of ~3 mW.

17 March 2026 11:11:27

© Author(s) 2025

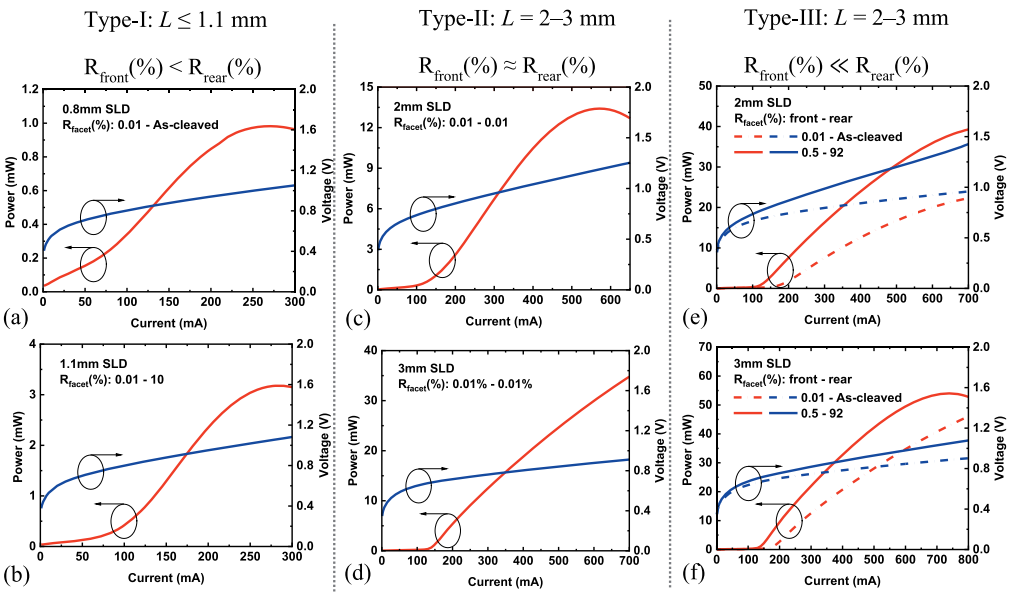


FIG. 3. *L–I–V* comparison of different types of SLD based on facet reflectivities [R_{facet}(%)] and cavity lengths (L): [(a), (b)] type-I SLD devices are short cavities ($L \leq 1.1$ mm) having AR (0.01%) at front and HR (10%, As-cleaved or 30%) at rear facets, [(c), (d)] type-II devices ($L = 2$–3 mm) have AR (0.01%) coatings at both facets, and [(e), (f)] type-III devices ($L = 2$–3 mm) have AR (0.01%, 0.5%) at front and higher HR (As-cleaved or 30%, 92%) at the rear facets.

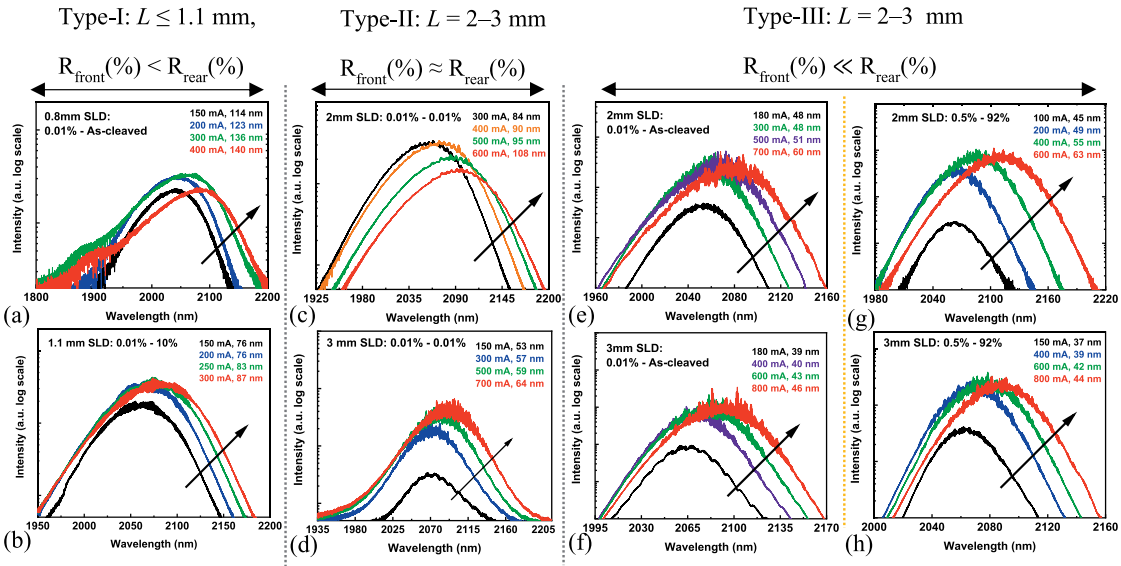


FIG. 4. Measured emission spectra of three types of 2.1 μm SLDs operated at RT in CW mode. The arrows indicate the changes in the spectrum with the increments of injecting currents.

17 March 2026 11:11:27

© Author(s) 2025

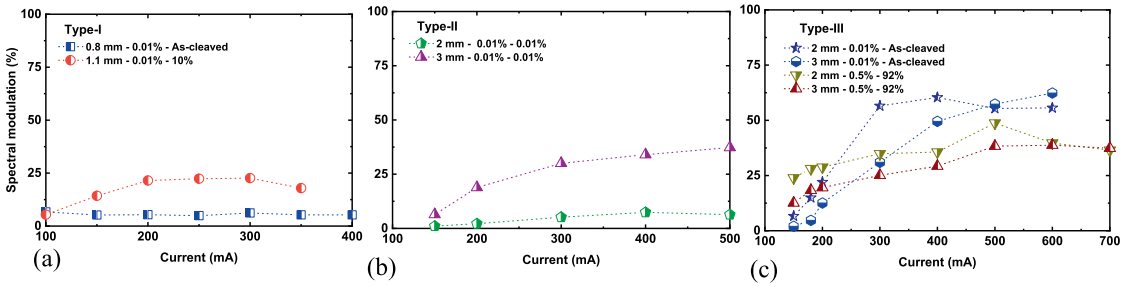


FIG. 5. SMD (%) for different injection currents in (a) type-I, (b) type-II, and (c) type-III SLDs, as shown in Fig. 4. All measurements are done at RT (~20 °C) in CW operation mode.

The SMD (%) varies from ~5% to ~20%, depending on injection current.

Type-II devices have AR coatings at both facets. Following Figs. 4(c) and 5(b), 2 mm SLD chips generate a maximum 108 nm FWHM broad and smooth spectrum (~3%–~7% SMD) and corresponds to ~13 mW power in CW at 600 mA. This result confirms the expected effect of AR coatings. The ASE peak could be tuned from 2.05 to 2.1 μm with a FWHM of ~70–~110 nm for an injection current increasing from 150 to 700 mA. Similarly, emission from the 3 mm long chip could be operated in the same spectral range for high power but offered limited bandwidth (~53–~64 nm). In the latter case, an increased straight RWG section (2.05 mm at the rear-facet) gives more amplification and high rippled ASE spectra (SMD ~5%–~35%).

Type-III SLDs exhibit a maximum ~60–~70 nm FWHM for chips with L = 2 mm and a maximum of 46 nm FWHM for chips with L = 3 mm at an injection of ~600–~1000 mA. In this case, the central emission wavelength was injection tuned from 2.06 to 2.12 μm for 2 mm chips and to 2.09 μm for 3 mm chips 0.5%/92% coated devices. The SMDs of these devices, as shown in Fig. 5(c), range from a minimum ~5% to a maximum ~25% when operated within ~200 mA. However, the SMD increases rapidly above 200 mA, primarily assumed due to unwanted reflections arising from the non-ideal AR coating. This results in higher visibility of the residual FP cavity modes enhanced by the ASE process. Furthermore, the highly reflective back-facets facilitate double-pass amplification in type-III gain structures, which is advantageous in terms of achieving higher power but again will give rise to unwanted spectral modulation. These effects are more visible for longer cavity devices due to higher accumulation of ASE.

The far-field (FF) beam profile of the J-shaped SLDs measured from the front facet is shown in Fig. 6(a) for a L = 3 mm (AR/As-cleaved) SLD, considered as an exemplary device. The Gaussian-shaped slow axis beam profile is offset by 23° from the central 0°-reference position, without any sign of side-lobes. This specific angular deviation from the 0°-reference to the facet-normal is expected from Snell's law for a 7° tilted optical field at the front-facet. The FWHM of the slow and fast axes are measured as 18° and 43°, respectively. The beam intensity profile slightly varies for all types of SLD devices due to different magnitudes of back-facet coating and cavity length. Figure 6(b) shows variations in slow axis beam intensity profile for 3 mm SLDs for a 1000 mA CW injection at RT. For the high reflective back-facet ($R \geq$ 90%, HR coated) with a different AR front facet (R ~0.5%) compared to other devices produced higher optical power density in the waveguide, which causes thermal lensing[43,44] and broadens the slow axis beam profile. The emitted beam profile has slightly broader FWHM compared to lower reflective devices at the same facet (21° vs 17°). However, the absence of the side lobes in either case confirms single transverse mode operation from the SLDs.

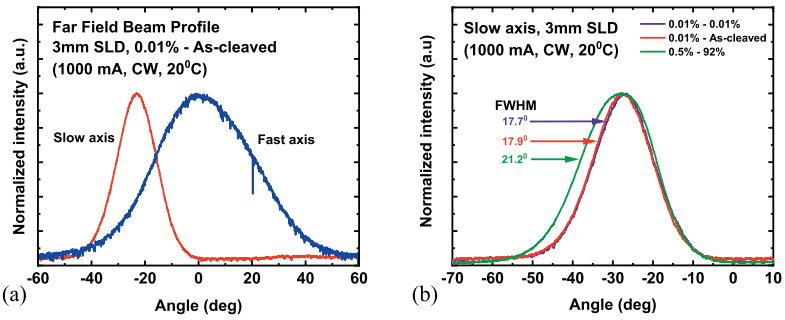


FIG. 6. Far-field (FF) beam profile of SLDs measured at 1000 mA from 3 mm SLD coated with AR at the front facet and no coating at the rear facet. In panel (a), the blue and red curves indicate fast and slow axes, respectively. The changes in the beam shape of slow axis due to different combinations of front and rear facets is shown in panel (b), measured from 3 mm SLDs.

17 March 2026 11:11:27

© Author(s) 2025

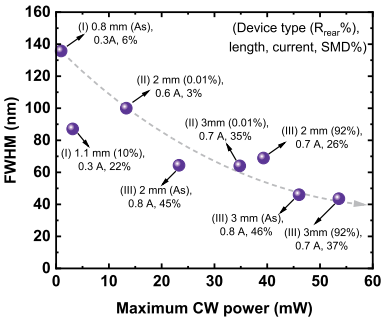


FIG. 7. FWHM (nm) of the emission spectrum at maximum CW power measured for different types of devices related to cavity length, injection current, and SMD (%).

Figure 7 summarizes the key performance of the devices analyzed, presenting the measured FWHM of the ASE spectral bandwidth corresponding to the maximum CW output power for each SLD variant. At their maximum CW operating powers, the SLD variants exhibit distinct trade-offs between output power and spectral characteristics. Type-I and 2 mm type-II devices achieve broad ASE spectral bandwidths ranging from ~90 to ~140 nm with low spectral modulation depth (minimum SMD ~3%), making them well-suited for broadband applications that require a smooth spectrum, such as in OCT imaging. In contrast, the 3 mm type-II device delivers significantly higher ASE output power, up to ~35 mW, but with a narrower spectral width of ~64 nm and increased spectral ripple (SMD ~35%), favoring applications where power is the primary requirement, such as in tunable laser-based application. Type-III SLDs offer a balanced performance, supporting higher ASE powers (~40 to 60 mW) while maintaining spectral widths between ~45 and ~70 nm. These results demonstrate how careful selection of device structure and cavity length enables optimization for specific optoelectronics and photonics applications.

The cavity suppression was studied according to different sets of facet coating parameters where cavity length and back-facet reflectivities control the amplification process and impact the emission bandwidth. For 2 mm type-II SLD having 0.01% reflectivity at both facets shows maximum 7% SMD at maximum power of 10.5 mW while maintaining a 90 nm FWHM spectral width. The shortest 0.8 mm SLD cavity shows the highest spectral emission bandwidth with ~140 nm FWHM at 0.7 mW free space power. The broad spectral emission confirms the combined effect of asymmetric QW design with a J-shaped RWG structure, which is a nearly twofold increment compared to prior reports of FWHMs in this spectral regime.[14,26,27] The emission power in such devices can be further enhanced by optimizing epi-structure, waveguide geometry, and mounting SLD chips in p-side-down orientation for efficient heat sinking. The ripple in the ASE spectra can be also smoothened by adjusting the RWG architecture and the facet coatings.

The trend line (dashed gray) in Fig. 7 shows an exponentially decaying relationship with maximum CW power to the corresponding FWHM emission bandwidth measured for increasing cavity length and rear-facet reflectivities. The data plot also explicitly shows a clear trend in growth of the maximum ASE power level following exponential dependency of gain, with increasing cavity length at reduced mirror losses.[42] To our observation, in short-cavity devices (Type-I, $L \leq 1.1$ mm), reduced gain length and combined facet reflectivities minimized optical feedback, preserving the broadband ASE spectrum shaped by the asymmetric QW gain. In contrast, longer cavities (Type-II, L = 3 mm/Type-III, L = 2–3 mm) introduced stronger feedback and spectral filtering, promoting mode selection near the maximum gain and narrowing the emission. These trends highlight how ASE characteristics arise from the interplay between QW design and cavity geometry.

In conclusion, we have reported electrically pumped single-transverse-mode SLDs operating at 2.1 μm wavelength showing a maximum 140 nm FWHM at room temperature for CW operation. This is a twofold improvement in emission bandwidth employing type-I GaInSb/AlGaAsSb double QWs utilizing asymmetrical thickness compared to the prior state-of-the-art in this spectral regime. The J-shaped RWG architecture acts effectively in suppressing the cavity facet from lasing and enables the generation of more than 50 mW of CW superluminescence emission power from p-side-up oriented SLD chips. In our experiments, we have systematically studied the effects of broadband AR/HR coatings on the device's facets on the spectral emission bandwidth and the depth of the spectral ripples. All SLDs show Gaussian-shaped emission spectra having injection tuning of central emission wavelength from 2050 nm to more than 2100 nm. The far-field Gaussian profile of the devices does not show any side lobes up to high injection current. Such a low-rippled wide spectral emission spectrum, RT emission power level with good beam quality opens a promising path for developing trace gas sensing and OCT at wavelength >2 μm.

The authors thank MSc. Mervi Koskinen and Dr. Heidi Tuorila for support during the wafer level fabrication. The authors also thank Dr. Nouman Zia and Dr. Samu Pekka Ojanen for valuable discussion and Dr. Marika Janka for providing guidance regarding AR/HR coatings. The authors acknowledge funding from the European Commission Horizon 2020 project "NExt Generation of Tunable LASers for Optical Coherence Tomography," Grant Agreement No. 860807 – NETLAS – H2020-MSCA-ITN-2019. This work was also linked to the Academy of Finland flagship program PREIN (decision 320168).

AUTHOR DECLARATIONS

Conflict of Interest

The authors have no conflicts to disclose.

Author Contributions

Ifte Khairul Alam Bhuiyan: Data curation (lead); Formal analysis (lead); Investigation (lead); Methodology (lead); Software (lead); Validation (lead); Visualization (lead); Writing – original draft (lead); Writing – review & editing (lead). **Joonas Hilska**: Formal analysis (supporting); Methodology (supporting); Resources (equal); Writing – review & editing (supporting). **Markus Peil**: Resources (equal). **Jukka Viheriälä**: Formal analysis (supporting); Funding acquisition (supporting); Investigation (equal); Project

17 March 2026 11:11:27

© Author(s) 2025

administration (equal); Resources (equal); Supervision (supporting); Writing – review & editing (supporting). **Mircea Guina**: Conceptualization (supporting); Funding acquisition (equal); Investigation (equal); Project administration (equal); Resources (equal); Supervision (lead); Writing – review & editing (supporting).

DATA AVAILABILITY

The data that support the findings of this study are available from the corresponding author upon reasonable request.

REFERENCES

[1]N. Matuschek, M. Rossetti, J. Napierala, M. Duelk, and C. Velez, "Numerical simulations of blue and green GaN SLEDs," in *2011 Numerical Simulation of Optoelectronic Devices* (IEEE, Rome, 2011), pp. 189–190.

[2]H. Ohno, K. Orita, M. Kawaguchi, K. Yamanaka, and S. Takigawa, "200 mW GaN-based superluminescent diode with a novel waveguide structure," in *IEEE Photonic Society 24th Annual Meeting* (IEEE, Arlington, VA, 2011), pp. 505–506.

[3]D. Huang, E. A. Swanson, C. P. LiN, J. S. Schuman, W. G. Stinson, W. Chang, M. R. Hee, T. Flotte, K. Gregory, C. A. Puliafito, and J. G. Fujimoto, "Optical coherence tomography," Science **254**, 1178–1181 (1991).

[4]W. Drexler and J. Fujimoto, "State-of-the-art retinal optical coherence tomography," Prog. Retinal Eye Res. **27**, 45–88 (2008).

[5]S. Yazdanfar, M. D. Kulkarni, and J. A. Izatt, "High resolution imaging of *in vivo* cardiac dynamics using color Doppler optical coherence tomography," Opt. Express **1**, 424–431 (1997).

[6]W. K. Burns, C.-L. Chen, and R. P. Moeller, "Fiber-optic gyroscopes with broadband sources," J. Lightwave Technol. **1**, 98–105 (1983).

[7]P. R. Ashley, M. G. Temmen, and M. Sanghadasa, "Applications of SLDs in fiber optical gyroscopes," paper presented at the Symposium on Integrated Optoelectronic Devices, San Jose, CA, 2002.

[8]J. Nayak, "Fiber-optic gyroscopes: From design to production [Invited]," Appl. Opt. **50**, E152 (2011).

[9]H. Lu, O. Alkhazragi, Y. Wang, N. Almaymoni, W. Yan, W. H. Gunawan, H. Lin, T.-Y. Park, T. K. Ng, and B. S. Ooi, "Low-coherence semiconductor light sources: Devices and applications," npj Nanophotonics **1**, 9 (2024).

[10]Z. Djinovic, M. Tomic, and N. Plank, "A fiber-optic sensing technique for submicrometer distance measurement between the surgical tools and retina," in *2021 44th International Convention on Information, Communication and Electronic Technology (MIPRO)* (IEEE, Opatija, 2021), pp. 1787–1792.

[11]M. Szczerska, P. Wityk, and P. Listewnik, "Impact of temperature on optical sensing in biology based on investigation of SARS-CoV-2," J. Biophotonics **16**, e202200186 (2023).

[12]L. Di Cecilia, S. Cattini, F. Giovanardi, and L. Rovati, "Single-arm self-mixing superluminescent diode interferometer for flow measurements," J. Lightwave Technol. **35**, 3577–3583 (2017).

[13]S. Cattini and L. Rovati, "A review on guided optical feedback in superluminescence diodes for metrological purposes," J. Lightwave Technol. **39**, 3771–3780 (2021).

[14]K. Vizbaras, E. Dvinelis, I. Šimonytė, A. Trinkūnas, M. Greibus, R. Songaila, T. Žukauskas, M. Kaušylas, and A. Vizbaras, "High power continuous-wave GaSb-based superluminescent diodes as gain chips for widely tunable laser spectroscopy in the 1.95–2.45 μm wavelength range," Appl. Phys. Lett. **107**, 011103 (2015).

[15]C. Shen, J. A. Holguin-Lerma, A. A. Alatawi, P. Zou, N. Chi, T. K. Ng, and B. S. Ooi, "Group-III-nitride superluminescent diodes for solid-state lighting and high-speed visible light communications," IEEE J. Sel. Top. Quantum Electron. **25**, 1–10 (2019).

[16]M. Leich, S. Kiltz, J. Dittmann, and C. Vielhauer, "Non-destructive forensic latent fingerprint acquisition with chromatic white light sensors," Proc. SPIE **7880**, 78800S (2011).

[17]N. M. Israelsen, C. R. Petersen, A. Barh, D. Jain, M. Jensen, G. Hannesschläger, P. Tidemand-Lichtenberg, C. Pedersen, A. Podoleanu, and O. Bang, "Real-time high-resolution mid-infrared optical coherence tomography," Light: Sci. Appl. **8**, 11 (2019).

[18]L. S. Rothman, I. E. Gordon, Y. Babikov, A. Barbe, D. Chris Benner, P. F. Bernath, M. Birk, L. Bizzocchi, V. Boudon, L. R. Brown, A. Campargue, K. Chance, E. A. Cohen, L. H. Coudert, V. M. Devi, B. J. Drouin, A. Fayt, J.-M. Flaud, R. R. Gamache, J. J. Harrison, J.-M. Hartmann, C. Hill, J. T. Hodges, D. Jacquemart, A. Jolly, J. Lamouroux, R. J. Le Roy, G. Li, D. A. Long, O. M. Lyulin, C. J. Mackie, S. T. Massie, S. Mikhailenko, H. S. P. Müller, O. V. Naumenko, A. V. Nikitin, J. Orphal, V. Perevalov, A. Perrin, E. R. Polovtseva, C. Richard, M. A. H. Smith, E. Starikova, K. Sung, S. Tashkun, J. Tennyson, G. C. Toon, V. G. Tyuterev, and G. Wagner, "The HITRAN2012 molecular spectroscopic database," J. Quant. Spectrosc. Radiat. Transfer **130**, 4–50 (2013).

[19]V. Damodaran, S. R. Rao, and N. J. Vasa, "Optical coherence tomography based imaging of dental demineralisation and cavity restoration in 840 nm and 1310 nm wavelength regions," Opt. Lasers Eng. **83**, 59–65 (2016).

[20]R.-A. Erdelyi, V.-F. Duma, C. Sinescu, G. M. Dobre, A. Bradu, and A. Podoleanu, "Dental diagnosis and treatment assessments: Between x-rays radiography and optical coherence tomography," Materials **13**, 4825 (2020).

[21]P. Targowski, M. Kowalska, M. Sylwestrzak, and M. Iwanicka, "OCT for examination of cultural heritage objects," in *Optical Coherence Tomography and Its Non-medical Applications*, edited by M. R. Wang (IntechOpen, 2020).

[22]M. Read, C. S. Cheung, H. Liang, A. Meek, and C. Korenberg, "A non-invasive investigation of Egyptian faience using long wavelength optical coherence tomography (OCT) at 2 μm," Stud. Conserv. **67**, 168–175 (2022).

[23]H. Liang, R. Lange, B. Peric, and M. Spring, "Optimum spectral window for imaging of art with optical coherence tomography," Appl. Phys. B **111**, 589–602 (2013).

[24]N. Zia, J. Viheriälä, R. Koskinen, A. Aho, S. Suomalainen, and M. Guina, "High power (60 mW) GaSb-based 1.9 μm superluminescent diode with cavity suppression element," Appl. Phys. Lett. **109**, 231102 (2016).

[25]D. Wang, J. Zhang, C. Hou, Y. Zhao, F. Cheng, X. Jia, S. Zhai, N. Zhuo, J. Liu, F. Liu, and Z. Wang, "High performance continuous-wave InP-based 2.1 μm superluminescent diode with InGaAsSb quantum well and cavity structure suppression," Appl. Phys. Lett. **113**, 161107 (2018).

[26]N. Zia, J. Viheriälä, E. Koivusalo, and M. Guina, "High-power single mode GaSb-based 2 μm superluminescent diode with double-pass gain," Appl. Phys. Lett. **115**, 231106 (2019).

[27]T. Wang, C. Yang, Y. Chen, J. Shi, H. Yu, X. Su, Y. Zhang, Y. Zhao, C. Tong, D. Wu, Y. Xu, H. Ni, and Z. Niu, "High power GaSb-based superluminescent diode with cascade cavity suppression waveguide geometry and ultra-low antireflection coating," Appl. Phys. Lett. **123**, 021102 (2023).

[28]A. Joullié and P. Christol, "GaSb-based mid-infrared 2–5 μm laser diodes," C. R. Phys. **4**, 621–637 (2003).

[29]K. Kashani-Shirazi, K. Vizbaras, A. Bachmann, S. Arafin, and M.-C. Amann, "Low-threshold strained quantum-well GaSb-based lasers emitting in the 2.5- to 2.7- μm wavelength range," IEEE Photonics Technol. Lett. **21**, 1106–1108 (2009).

[30]G. Belenky, L. Shterengas, M. V. Kisin, and T. Hosoda, "Gallium antimonide (GaSb)-based type-I quantum well diode lasers: Recent development and prospects," in *Semiconductor Lasers* (Elsevier, 2013), pp. 441–486.

[31]T. D. Eales, I. P. Marko, B. A. Ikyo, A. R. Adams, S. Arafin, S. Sprengel, M.-C. Amann, and S. J. Sweeney, "Wavelength dependence of efficiency limiting mechanisms in type-I mid-infrared GaInAsSb/GaSb lasers," IEEE J. Sel. Top. Quantum Electron. **23**, 1–9 (2017).

[32]M. Kurka, M. Dyksik, S. Suomalainen, E. Koivusalo, M. Guina, and M. Motyka, "GaInAsSb/AlGa(In)AsSb type I quantum wells emitting in 3 μm range for application in superluminescent diodes," Opt. Mater. **91**, 274–278 (2019).

[33]H. Hager, C. S. Hong, J. Mantz, E. Chan, D. Booher, and L. Figueroa, "Broadband emission from a multiple asymmetric quantum-well light-emitting diode," IEEE Photonics Technol. Lett. **3**, 436–438 (1991).

[34]C.-F. Lin, B.-L. Lee, and P.-C. Lin, "Broad-band superluminescent diodes fabricated on a substrate with asymmetric dual quantum wells," IEEE Photonics Technol. Lett. **8**, 1456–1458 (1996).

[35]C.-F. Lin and B.-L. Lee, "Extremely broadband AlGaAs/GaAs superluminescent diodes," Appl. Phys. Lett. **71**, 1598–1600 (1997).

[36]C.-F. Lin, C.-W. Tsai, Y.-S. Su, and G. S. Shmavonyan, "Extremely broadband InGaAsP/InP superluminescent diode/semiconductor optical amplifiers with emission spectrum covering from 1250 nm to 1650 nm," in *Optical Amplifiers and their Applications* (OSA, Otaru, 2003), p. MD20.

17 March 2026 11:11:27

© Author(s) 2025

[37]T. D. Nguyen, J. Hwang, Y. Kim, E.-T. Kim, J. O. Kim, and S. J. Lee, "Dual-wavelength InGaAsSb/AlGaAsSb quantum-well light-emitting diodes," J. Korean Phys. Soc. **72**, 1249–1253 (2018).
[38]See https://photond.com/products/harold.htm for more information about HAROLD by photon design, 2023.
[39]A. Bignazzi, A. Bosacchi, and R. Magnanini, "Photoluminescence study of heavy doping effects in Te-doped GaSb," J. Appl. Phys. **81**, 7540–7547 (1997).
[40]M. Cherchi, S. Ylinen, M. Harjanne, M. Kapulainen, and T. Aalto, "Dramatic size reduction of waveguide bends on a micron-scale silicon photonic platform," Opt. Express **21**, 17814–17823 (2013).
[41]J. Boeck and M.-C. Amann, "AlGaAs/GaAs double-heterostructure superluminescent diodes for optical transmission systems," Frequenz **33**, 278–283 (1979).
[42]G. A. Alphonse, "Design of high-power superluminescent diodes with low spectral modulation," Proc. SPIE **4648**, 125–138 (2002).
[43]P. K. L. Chan, K. P. Pipe, J. J. Plant, R. B. Swint, and P. W. Juodawlkis, "Temperature mapping and thermal lensing in large-mode, high-power laser diodes," Appl. Phys. Lett. **89**, 201110 (2006).
[44]H. Yang, L. J. Mawst, and D. Botez, "1.6 W continuous-wave coherent power from large-index-step ($\Delta n \approx 0.1$) near-resonant, antiguided diode laser arrays," Appl. Phys. Lett. **76**, 1219–1221 (2000).

17 March 2026 11:11:27

© Author(s) 2025

PUBLICATION
II

Broadband 2-μm superluminescent diodes with GaSb-based variable-thickness quantum wells

Ifte Khairul Alam Bhuiyan, Joonas Hilska, Markus Peil, Jukka Viheriälä, Mircea Guina

Applied Physics Letter **127**(16), 163307, (2025)
DOI: 10.1063/5.0283821

Publication is licensed under a Creative Commons Attribution 4.0 International License CC-BY

Broadband 2-μm superluminescent diodes with GaSb-based variable-thickness quantum wells

Cite as: Appl. Phys. Lett. **127**, 163307 (2025); doi: 10.1063/5.0283821
Submitted: 3 June 2025 · Accepted: 7 October 2025 ·
Published Online: 22 October 2025

View Online Export Citation CrossMark

Ifte Khairul Alam Bhuiyan,[a] Joonas Hilska, Markus Peil, Jukka Viheriälä, and Mircea Guina

AFFILIATIONS

Optoelectronics Research Centre, Physics Unit, Tampere University, Korkeakoulunkatu 3, 33720 Tampere, Finland

[a]Author to whom correspondence should be addressed: ifte.alambhuiyan@tuni.fi

ABSTRACT

A GaSb-based superluminescent diode (SLD) operating near the 2-μm wavelength region, employing quantum wells with variable thicknesses to achieve broadband emission, is reported. The gain region incorporates two $Ga_{0.73}In_{0.27}Sb/Al_{0.27}Ga_{0.73}As_{0.02}Sb_{0.98}$ quantum wells with identical composition but significant difference in the thicknesses of 7 and 13 nm, exhibiting broadband amplified spontaneous emission. To minimize reflections from the output facet and to enable operation at high current injection, we employed a J-shaped ridge waveguide. For an injection current of ∼200 mA, the device delivers a continuous-wave output power of ∼1.2 mW at room temperature exhibiting a bimodal emission spectrum with a combined bandwidth of ∼132 nm. Increasing the injection current to 1000 mA results in a maximum output power of ∼40 mW, accompanied by emission bandwidth narrowing to ∼40 nm. In general, the broad amplified spontaneous emission spectrum demonstrates the capacity of variable-thickness quantum wells to further engineer the emission properties extending the bandwidth and the output power in GaSb-based SLDs and opens a path for practical applications in advanced optical coherence tomography, spectroscopy, and microscopy.

© 2025 Author(s). All article content, except where otherwise noted, is licensed under a Creative Commons Attribution (CC BY) license (https://creativecommons.org/licenses/by/4.0/). https://doi.org/10.1063/5.0283821

17 March 2026 11:51:03

The spectral window spanning 1.7–3 μm encompasses strong vibrational absorption bands of numerous gases (e.g., CO_2, CH_4, and NH_3)[1] as well as overtone and combination of stretch and bending vibration of liquid biomolecules, including water, lipids, and proteins.[2] This wealth of molecular fingerprints in this spectral region has prompted the deployment of absorption-based spectroscopy technology for a wide range of applications involving gas sensing and identification of specific molecules in liquids. Compared to visible or near-IR, this spectral window also offers reduced scattering and improved molecular contrast in profiling lipid- and collagen-rich tissues, making it attractive for optical coherence tomography (OCT) imaging.[3,4] For both areas of applications, the availability of practical light sources emitting broadband radiation at acceptable power levels (mW-level) and exhibiting low spectral modulation depth (defined here as minimal relative intensity variation across the emission bandwidth) are instrumental. To this end, superluminescent diodes (SLDs) present compelling features.[5–7] Unlike laser diodes (LDs), SLDs emit broadband radiation owing to amplified spontaneous emission (ASE) while offering high spatial brightness combined with low temporal coherence. These features make them ideal for speckle free imaging and interferometric sensing[6] and, in recent years, have triggered a noticeable effort for developing GaSb SLD devices at 2-μm and beyond.

With reference to the results summarized in Fig. 1, we note some of the most representative SLD demonstrations starting with emission at around 1.73-μm[8] and extensions to 1.9,[8,9] 2,[10–12] 2.25,[13] 2.4,[13] and 2.55-μm.[14] In all cases, the gain media have utilized heterostructures including symmetric (one type) quantum wells (QWs), and the emission bandwidth has been generally limited to below or around ∼100 nm.

To significantly extend the emission bandwidth, one can employ bandgap-engineering of the QWs either by using QWs with different thicknesses, by varying their composition, or by combining both of these approaches.[15–23] In general, the use of asymmetric QWs to achieve broadband gain has been widely deployed for laser diodes[17,18,22,24] and to achieve broad superluminescence emission[19–21,25,26] at wavelength around 1.5-μm or below. For example, Mikami *et al.*[15] demonstrated a broadband SLD device employing InGaAsP/InP double-QW heterostructure with different thicknesses, exhibiting 80 nm (∼59 meV) and 140 nm (∼77 meV) broad ASE spectrum around 1.3 and 1.5-μm, respectively. In general, device demonstrations at this wavelength range make use of InP-based heterostructures. For GaSb-based materials, used for the short-wave infrared (SWIR) wavelength region, variable-thickness QW structures have been deployed only in broadband gain LD-structures and light emitting diodes (LEDs). For example, Jiang *et al.*[27] demonstrated broad gain spectra in a 2.1-μm multimode diode

© Author(s) 2025

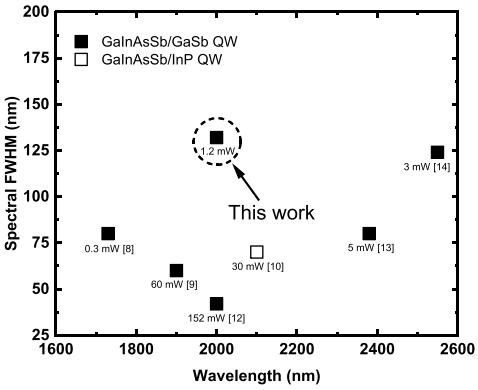


FIG. 1. Reported SLD spectral FWHM and power in the 1.7–2.6 μm wavelength range for single transverse mode operation using symmetric GaInAsSb QWs. The performance of the device reported in this work utilizing variable-thickness GaSb-based QWs has bimodal emission and is highlighted with a dashed circle. Given the bimodal emission spectrum, the spectral width is reported as the sum of the FWHMs corresponding to the two dominant spectral peaks.

laser structure comprising multiple InGaAsSb and InGaSb QWs with different thickness and compositions. In another report, Nguyen *et al.*[28] demonstrated a GaSb multiple-QW LEDs with varying QW thicknesses emitting at both 1.97 and 2.1-μm.

In this report, we extend the use of GaSb-based variable-thickness QWs to 2-μm SLD devices and demonstrate major broadening of the emission spectra compared to reported results for the similar wavelength region (see Fig. 1). More precisely, we use a heterostructure with two $Ga_{0.73}In_{0.27}Sb/Al_{0.27}Ga_{0.73}As_{0.02}Sb_{0.98}$ QWs with the same composition but a relatively large difference in the thicknesses of 7 and 13 nm. We study the photoluminescence properties and how the SLD spectral output depends on the injection level and demonstrate continuous-wave room-temperature operation with ability to reach a combined spectral width as broad as ~132 nm.

The generic layer and bandgap design of the heterostructure used for the study are shown in Fig. 2. The thickness of the QWs was optimized to produce broad gain spectra using Harold laser simulation software.[29] To this end, we simulated the emission of a Fabry–Pérot laser diode with an active region similar to the SLD. The active layers comprised two $Ga_{0.73}In_{0.27}Sb$ QWs with ~1.7% compressive strain embedded in lattice matched $Al_{0.27}GaAs_{0.02}Sb$ barriers exhibiting a type-I band alignment for efficient carrier recombination. The QWs had a thickness of 7 and 13 nm, with the thinner QW grown near the p-side and the thicker QW near the n-side of the heterostructure. The QWs were separated by a 20 nm $Al_{0.27}GaAs_{0.02}Sb$ barrier and surrounded by undoped $Al_{0.27}GaAs_{0.02}Sb$ waveguide (WG) layers with a thickness of 130 nm on both sides of the QW. The separate confinement heterostructure was further defined by two doped $Al_{0.50}GaAs_{0.04}Sb$ cladding layers with a thickness of 2.7 and 2 μm for n- and p-side, respectively. The n-side cladding layer was doped to $\sim 3 \times 10^{17}\,cm^{-3}$, while the 2 μm thick p-cladding layer was doped to $\sim 6 \times 10^{18}\,cm^{-3}$. We note that the doping was graded for the 500 nm around WG core to reduce free-carrier absorption. The structure was capped by 200 nm p-GaSb cap layer that was highly doped with Be to $\sim 3 \times 10^{19}\,cm^{-3}$. The structure was grown on 2 in. n-GaSb (100) substrate using solid-source molecular beam epitaxy. The grown epitaxial wafer was processed into 3 mm long (L) and 5 μm wide (w) ridge waveguide (RWG) devices with a J-shaped geometry [see in Fig. 2(c)]. The 7° curved Euler bend[30] near the front facet (top side) is effective in suppressing the unwanted facet reflections, promoting SLD operation. The length of the curved section was $L_{curved} = 0.95$ mm, and the remaining straight has a length of $L_{straight} = 2.05$ mm. The front and

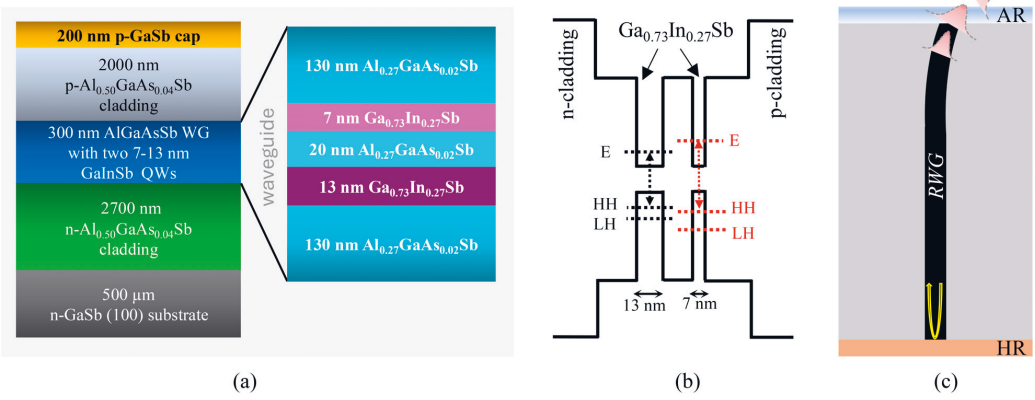


FIG. 2. (a) Schematic of the layer structure; (b) illustration of the conduction band (top solid black line) and valence band (bottom solid black line) alignment corresponding to the active area (not in scale). The vertical black and red dotted lines in the QWs indicate the lowest energy transition in both QWs. (c) Schematic of the J-shaped waveguide architecture with a 7° curved (Euler bend) at antireflection coated (AR) front facet and straight rear facet (HR).

17 March 2026 11:51:03

© Author(s) 2025

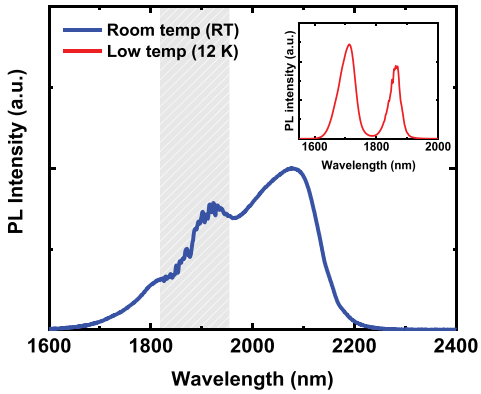


FIG. 3. RT-PL spectra of the active region calibration growth. The greyed-out portion of the spectrum is influenced by atmospheric absorption. Inset shows the low temperature (∼12 K) PL measurement from the same heterostructure.

rear mirror facets of the SLD cavity were coated using ion-beam sputtering (IBS) to deposit a broadband anti-reflective (AR; R_{front} ∼0.5% from ∼1910 nm to ∼2125 nm) and highly reflective (HR; $R_{rear} \geq 90\%$ from ∼1900 nm to ∼2300 nm) films, respectively.

In Fig. 3, the solid blue line shows the RT photoluminescence (PL) emission spectra measured from an active region calibration growth structure, which incorporates the complete active region layer stack but omits the thick doped cladding layers. This results in a physically thinner epitaxial structure that facilitates efficient optical pumping and collection of the photoluminescence signal. This PL spectrum shows double peak emission near ∼1923 and ∼2078 nm originating from thinner and thicker QW, respectively. We note that the measured emission spectrum is affected by atmospheric absorption around the ∼1.9-μm wavelength (greyed-out). Therefore, in the inset of Fig. 3, we show low temperature (∼12 K) PL measurements (solid red line) from the same epi-structure where the PL emission is more clearly distinguished into two distinct components (peaks at ∼1713 and ∼1863 nm) with reduced effects from atmospheric absorption.

Charge carriers are electrically pumped into the active region to generate photons, part of which travel directly to the end facets, and the other part reflect from the rear facet, exhibiting enhanced ASE on the exit through the AR coated front facet. The coated chip was mounted p-side up on AlN submount using silver epoxy glue, and the mount was attached to a thermo-electrical element for temperature control.

The fabricated SLD was first analyzed in terms of output power and voltage dependence on current injection (i.e., *L–I–V* characteristic). Figure 4(a) shows the measured *L–I–V* behavior together for direct current (DC) injection at RT. At low current injection up to ∼150 mA (CW power ∼0.37 mW), the emission power varies linearly with current. In this regime, the SLD generates only spontaneous emission. Increasing the injection (from 150 to 250 mA) switches the device to the linear gain region, and the output power increases first exponentially with current due to stimulated emission. Further increasing the injection above 250 mA, the SLD output varies linearly with current (until ∼500 mA) due to onset of the gain saturation.

For CW operation, the maximum power of the SLD was recorded to be ∼40 mW at ∼900 mA at 20 °C. The maximum power level is slightly reduced and shifted to lower current (∼860 mA) with increasing temperature due to increased carrier leakage, gain saturation, and non-radiative recombination. The recorded maximum CW power level was reduced to 33 mW at an increased temperature of ∼50 °C. The device was also operated in pulsed mode (1% duty cycle, 100 μs pulse width). As shown in Fig. 4(b), the measured power was stable around 70 mW for 1000 mA at different temperatures without any thermal roll-over. Derivative or slope efficiency of the SLD was also calculated at different temperatures at the same operation mode. The maximum recorded slope efficiency was found to be 0.0945 W/A at 280 mA for RT operation. For the increased temperature, the maximum efficiency followed a down shift to 0.089 W/A at an injection current of 310 mA. The voltage level at a maximum driving current 1000 mA was ∼1.08 V and remained stable during all operating temperatures (20–50 °C).

Figure 5 shows the SLD's output spectrum measured over 150–1000 mA injection current in the CW mode at RT. The measurement setup consisted of a Yokogawa AQ6375 optical spectrum analyzer (OSA) with 0.1 nm wavelength resolution and an input optical fiber port. The ASE output from the SLD chip was free-space coupled into Thorlab's P4-2000AR-2 single mode fiber patch cable. The other end of the fiber (AR coated; R < 0.25%) was connected to the OSA's input terminal through ferrule connector/angled physical contact (FC/APC) type connector to minimize any backreflection of the

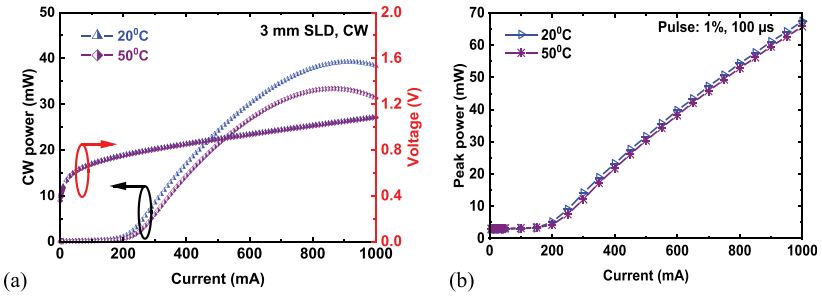


FIG. 4. Measured *L–I–V* characteristics of SLD driven at (a) the CW mode and at (b) the pulse mode (1% duty cycle, 100 μs pulse) at 20 and 50 °C.

17 March 2026 11:51:03

© Author(s) 2025

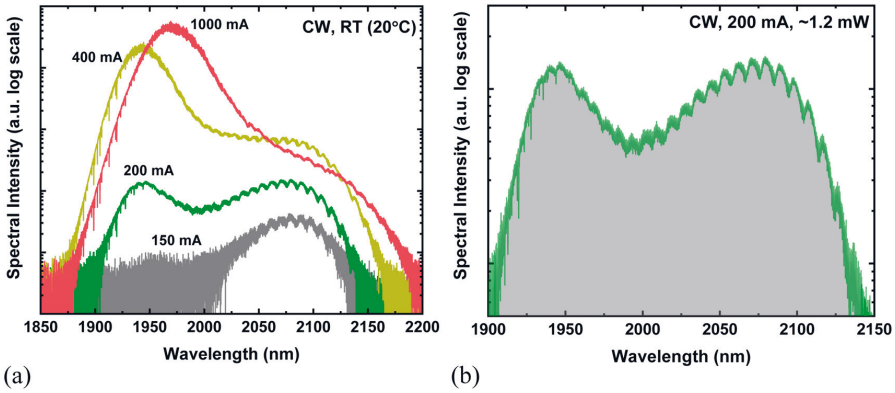


FIG. 5. (a) SLD emission spectra for different current at RT and CW operation; (b) magnified ASE spectrum at 200 mA, highlighting balanced emission from the QWs and residual Fabry–Pérot cavity effect.

signal. ASE spectra recorded at 150, 200, 400, and 1000 mA are displayed in the figure. Below ASE threshold (<200 mA), pure spontaneous emission is generated at ~150 mA at the longer-wavelength region (~2.078-μm) due to ground transition from the 13 nm thick QW. This is due to the density of available states in the double-QW system being first higher at the thicker QW (lowest energy state). Increasing the injection ($\geq$ 180 mA) allows carriers to populate at the thinner QW and recombine to produce emission at shorter wavelength (~1.95-μm).

Figure 5(b) shows a magnified view of the ASE spectrum for an injection current ~200 mA (the corresponding linear scale spectrum is provided in the supplementary material). The emission is bimodal, with two dominant peaks near ~1.95 and ~2.08-μm, separated by ~130 nm, with ~4-dB peak-to-peak variation. Because this dip prevents a conventional cross-lobe FWHM definition to be considered as a figure-of-merit, we report the individual FWHM levels for the dominant peaks of ~47 nm (~15 meV) for the shorter-wavelength peak and ~85 nm (~24 meV) for the longer-wavelength peak with a FWHM sum value of ~132 nm. This situation is attributed to equalization of the peak gain from both QWs.[22] For bias currents extending to 250 mA, the emission spectra remain bimodal with a few-dB inter-peak modulation, with significant spectral power density across the ~1920–2120 nm, at adequate levels (several μW/nm) for applications such as OCT and spectroscopy.[31–33] At a higher injection of ~400 mA, the dominant emission peak at ~1945 nm shows a FWHM of ~38 nm (~12.5 meV) due to the stronger confinement in the thinner (7 nm) QW. The emission at this bias associated with the thicker (13 nm) QWs is comparatively weaker, leading to a spectrum skewed toward the ~1900–2000 nm region. Similarly, at 1000 mA, the emission peak redshifts slightly to ~1970 nm, with a FWHM of ~40 nm (~12.8 meV). While the emission bandwidth (FWHM) clearly narrows at higher injection, the emission bandwidth at the –20 dB level still extends from 1897 to 2120 nm (i.e., ~220 nm) at 400 mA and from 1913 to 2065 nm (i.e., ~152 nm) at 1000 mA.

The calculated spectral modulation depth is as low as ~4% when the SLD was operated at balanced QW injection regime around ~200 mA. Such low spectral modulation is a key requirement for high quality nondestructive OCT inspection. The coherence length is estimated as ~5 μm using autocorrelation-based approach from measured spectrum[34] and gives a clear indication of the SLD's suitability in non-invasive OCT inspection to produce high-resolution OCT image compared to existing results.[35–38]

We have measured the SLD's beam quality by assessing the Far-Field (FF) pattern at RT in the CW mode. The beam patterns both in lateral and transverse direction follow Gaussian distribution without showing any sidelobes. The measured beam divergence angle varied from 18 to 20° along the slow axis (transverse) and remained stable at ~40° along the fast axis (lateral) for injection currents between 400 and 1000 mA (see the supplementary material). The transverse beam exited through 7° curved RWG and following Snell's law of refraction. The beam shapes confirm transverse single mode operation of the J-waveguide and suitability for efficient coupling into a single mode fiber.

In conclusion, we demonstrated an electrically pumped GaSb-based SLD operating in the 1.9–2.1 μm spectral range with record broadband ASE. Double-pass amplification and cavity suppression are reported employing J-shaped RWG along with an active region containing type-I variable thickness double QWs. A combined −3 dB bandwidth of ~132 nm with smooth ASE emission at ~1.2 mW power for an CW injection of ~200 mA at the RT mode is reported. The far-field (FF) beam profile and emission angle of ~23° relative to the RWG axis at the output facet confirm the efficacy of the J-shaped waveguide geometry. Generated broadband ASE emission spanning from ~1917 to ~2122 nm at −6 dB validates the drastic role. The integration of dimensional variation in QWs has in terms of ASE emission broadening. Carrier distribution between QWs is shown to be sensitive to injection current, indicating that precise current control is essential to maintain spectral flatness across the broadband output. The demonstrated broadband GaSb-based SLDs hold strong promises for enabling high-resolution optical coherence tomography (OCT) and for the development of widely tunable laser sources, either in external-cavity configurations or integrated with silicon photonics. Further engineering of the active region by integrating multiple QWs with tailored

17 March 2026 11:51:03

© Author(s) 2025

thicknesses and band alignments can enable better spectral overlap of QW transition energies, thereby flattening and broadening the ASE spectrum as well as increasing output power.

See the supplementary material for a detailed picture of the calculated electronic band structure of the variable-thickness quantum well design shown in Fig. 2(b), including the conduction band (CB) and valence band (VB) profiles along with the corresponding confined electron and hole wavefunctions. The document also provides the linearly scaled ASE spectra from Fig. 5(b), offering additional insight into the spectral characteristics of the SLD device driven at a specific bias condition. Furthermore, this supplementary includes exemplary FF beam characteristics for the same device discussed in this work.

The authors gratefully acknowledge M.Sc. Mervi Koskinen for her support in wafer-level fabrication. Valuable discussions with Dr. Nouman Zia and Dr. Samu Pekka Ojanen are also appreciated. The authors thank Dr. Heikki Virtanen and Dr. Marika Janka for their expert guidance in IBS operation and AR/HR coatings. This work was supported by the European Commission under the Horizon 2020 program through the project Next Generation of Tunable Lasers for Optical Coherence Tomography (Grant Agreement No. 860807–NETLAS–H2020-MSCA-ITN-2019). Additional support was provided by the Research Council of Finland Flagship Programme PREIN (Decision No. 320168).

AUTHOR DECLARATIONS

Conflict of Interest

The authors have no conflicts to disclose.

Author Contributions

Ifte Khairul Alam Bhuiyan: Data curation (lead); Formal analysis (lead); Investigation (lead); Methodology (lead); Software (lead); Visualization (lead); Writing – original draft (lead); Writing – review & editing (lead). **Joonas Hilska:** Formal analysis (supporting); Methodology (supporting); Writing – original draft (supporting). **Markus Peil:** Data curation (supporting); Methodology (supporting). **Jukka Viheriälä:** Formal analysis (equal); Funding acquisition (equal); Project administration (equal); Resources (lead); Supervision (equal); Writing – review & editing (supporting). **Mircea Guina:** Conceptualization (supporting); Funding acquisition (equal); Investigation (supporting); Project administration (equal); Resources (equal); Supervision (lead); Writing – review & editing (equal).

DATA AVAILABILITY

The data that support the findings of this study are available from the corresponding author upon reasonable request.

REFERENCES

[1]L. S. Rothman, I. E. Gordon, Y. Babikov, A. Barbe, D. Chris Benner, P. F. Bernath, M. Birk, L. Bizzocchi, V. Boudon, L. R. Brown, A. Campargue, K. Chance, E. A. Cohen, L. H. Coudert, V. M. Devi, B. J. Drouin, A. Fayt, J.-M. Flaud, R. R. Gamache, J. J. Harrison, J.-M. Hartmann, C. Hill, J. T. Hodges, D. Jacquemart, A. Jolly, J. Lamouroux, R. J. Le Roy, G. Li, D. A. Long, O. M. Lyulin, C. J. Mackie, S. T. Massie, S. Mikhailenko, H. S. P. Müller, O. V. Naumenko, A. V. Nikitin, J. Orphal, V. Perevalov, A. Perrin, E. R. Polovtseva, C. Richard, M. A. H. Smith, E. Starikova, K. Sung, S. Tashkun, J. Tennyson, G. C. Toon, V. Tyuterev, and G. Wagner, "The HITRAN2012 molecular spectroscopic database," J. Quant. Spectrosc. Radiat. Transfer **130**, 4–50 (2013).
[2]A. K. Amerov, J. Chen, and M. A. Arnold, "Molar absorptivities of glucose and other biological molecules in aqueous solutions over the first overtone and combination regions of the near-infrared spectrum," Appl. Spectrosc. **58**, 1195–1204 (2004).
[3]D. Huang, E. A. Swanson, C. P. Lin, J. S. Schuman, W. G. Stinson, W. Chang, M. R. Hee, T. Flotte, K. Gregory, C. A. Puliafito, and J. G. Fujimoto, "Optical coherence tomography," Science **254**, 1178–1181 (1991).
[4]W. Drexler and J. Fujimoto, "State-of-the-art retinal optical coherence tomography," Prog. Retinal Eye Res. **27**, 45–88 (2008).
[5]W. Burns, C.-L. Chen, and R. Moeller, "Fiber-optic gyroscopes with broadband sources," J. Lightwave Technol. **1**, 98–105 (1983).
[6]G. A. Alphonse, D. B. Gilbert, M. G. Harvey, and M. Ettenberg, "High-power superluminescent diodes," IEEE J. Quantum Electron. **24**, 2454–2457 (1988).
[7]G. A. Alphonse, "Design of high-power superluminescent diodes with low spectral modulation," in Presented at the Symposium on Integrated Optoelectronic Devices, San Jose, CA (2002).
[8]A. Vizbaras, I. Šimonytė, A. Miasojedovas, A. Trinkūnas, T. Bučiūnas, M. Greibus, G. Naujokaitė, N. Torcheboeuf, S. Droz, D. Boiko, Ž. Dambrauskas, A. Gulbinas, and K. Vizbaras, "Swept-wavelength lasers based on GaSb gain-chip technology for non-invasive biomedical sensing applications in the 1.7–2.5 μm wavelength range," Biomed. Opt. Express. **9**, 4834 (2018).
[9]N. Zia, J. Viheriälä, R. Koskinen, A. Aho, S. Suomalainen, and M. Guina, "High power (60 mW) GaSb-based 1.9 μm superluminescent diode with cavity suppression element," Appl. Phys. Lett. **109**, 231102 (2016).
[10]D. Wang, J. Zhang, C. Hou, Y. Zhao, F. Cheng, X. Jia, S. Zhai, N. Zhuo, J. Liu, F. Liu, and Z. Wang, "High performance continuous-wave InP-based 2.1 μm superluminescent diode with InGaAsSb quantum well and cavity structure suppression," Appl. Phys. Lett. **113**, 161107 (2018).
[11]N. Zia, J. Viheriälä, E. Koivusalo, and M. Guina, "High-power single mode GaSb-based 2 μm superluminescent diode with double-pass gain," Appl. Phys. Lett. **115**, 231106 (2019).
[12]T. Wang, C. Yang, Y. Chen, J. Shi, H. Yu, X. Su, Y. Zhang, Y. Zhao, C. Tong, D. Wu, Y. Xu, H. Ni, and Z. Niu, "High power GaSb-based superluminescent diode with cascade cavity suppression waveguide geometry and ultra-low anti-reflection coating," Appl. Phys. Lett. **123**, 021102 (2023).
[13]K. Vizbaras, E. Dvinelis, I. Šimonytė, A. Trinkūnas, M. Greibus, R. Songaila, T. Žukauskas, M. Kaušylas, and A. Vizbaras, "High power continuous-wave GaSb-based superluminescent diodes as gain chips for widely tunable laser spectroscopy in the 1.95–2.45 μm wavelength range," Appl. Phys. Lett. **107**, 011103 (2015).
[14]N. Zia, J. Viheriälä, E. Koivusalo, H. Virtanen, A. Aho, S. Suomalainen, and M. Guina, "GaSb superluminescent diodes with broadband emission at 2.55 μm," Appl. Phys. Lett. **112**, 051106 (2018).
[15]O. Mikami, H. Yasaka, and Y. Noguchi, "Broader spectral width InGaAsP stacked active layer superluminescent diodes," Appl. Phys. Lett. **56**, 987–989 (1990).
[16]C.-F. Lin, B.-L. Lee, and P.-C. Lin, "Broad-band superluminescent diodes fabricated on a substrate with asymmetric dual quantum wells," IEEE Photonics Technol. Lett. **8**, 1456–1458 (1996).
[17]M. J. Hamp and D. T. Cassidy, "Critical design parameters for engineering broadly tunable asymmetric multiple-quantum-well lasers," IEEE J. Quantum Electron. **36**, 978–983 (2000).
[18]M. J. Hamp, D. T. Cassidy, B. J. Robinson, Q. C. Zhao, and D. A. Thompson, "Effect of barrier thickness on the carrier distribution in asymmetric multiple-quantum-well InGaAsP lasers," IEEE Photonics Technol. Lett. **12**, 134–136 (2000).
[19]C.-F. Lin, B.-R. Wu, L.-W. Laih, and T.-T. Shih, "Sequence influence of non-identical InGaAsP quantum wells on broadband characteristics of semiconductor optical amplifiers–superluminescent diodes," Opt. Lett. **26**, 1099 (2001).
[20]C.-W. Tsai, Y.-C. Chang, G. S. Shmavonyan, Y.-S. Su, and C.-F. Lin, "Extremely broadband superluminescent diodes/semiconductor optical amplifiers in optical communication band," in Presented at the Integrated Optoelectronics Devices, San Jose, CA (2003).

17 March 2026 11:51:03

© Author(s) 2025

[21]O.-K. Kwon, K. Kim, E.-D. Sim, J.-H. Kim, H.-S. Kim, and K.-R. Oh, "Asymmetric multiple-quantum-well laser diodes with wide and flat gain," Opt. Lett. **28**, 2189 (2003).
[22]J. Wang, M. J. Hamp, and D. T. Cassidy, "Design considerations for asymmetric multiple quantum well broad spectral width superluminescent diodes," IEEE J. Quantum Electron. **44**, 1256–1262 (2008).
[23]T. Ohgoh, A. Mukai, J. Yaguchi, and H. Asano, "Demonstration of 1.0 μm InGaAs high-power and broad spectral bandwidth superluminescent diodes by using dual quantum well structure," Appl. Phys. Express. **6**, 014101 (2013).
[24]T. Yamatoya, S. Mori, F. Koyama, and K. Iga, "High power GaInAsP/InP strained quantum well superluminescent diode with tapered active region," Jpn. J. Appl. Phys. **38**, 5121 (1999).
[25]C.-F. Lin, C.-W. Tsai, Y.-S. Su, and G. Shmavonyan, "Extremely broadband InGaAsP/InP superluminescent diode/semiconductor optical amplifiers with emission spectrum covering from 1250 nm to 1650 nm," in *Optical Amplifiers and Their Applications* (OSA, Otaru, 2003), p. MD20.
[26]C.-F. Lin and B.-L. Lee, "Extremely broadband AlGaAs/GaAs superluminescent diodes," Appl. Phys. Lett. **71**, 1598–1600 (1997).
[27]J. Jiang, L. Shterengas, T. Hosoda, A. Belyanin, G. Kipshidze, and G. Belenky, "GaSb-based diode lasers with asymmetric coupled quantum wells," Appl. Phys. Lett. **113**, 071106 (2018).
[28]T. D. Nguyen, J. Hwang, Y. Kim, E.-T. Kim, J. O. Kim, and S. J. Lee, "Dual-wavelength InGaAsSb/AlGaAsSb quantum-well light-emitting diodes," J. Korean Phys. Soc. **72**, 1249–1253 (2018).
[29]See https://photond.com/products/harold.htm for more information about HAROLD by Photon Design (2023).
[30]M. Cherchi, S. Ylinen, M. Harjanne, M. Kapulainen, and T. Aalto, "Dramatic size reduction of waveguide bends on a micron-scale silicon photonic platform," Opt. Express **21**, 17814–17823 (2013).
[31]C. S. Cheung, J. M. O. Daniel, M. Tokurakawa, W. A. Clarkson, and H. Liang, "Optical coherence tomography in the 2-μm wavelength regime for paint and other high opacity materials," Opt. Lett. **39**, 6509 (2014).
[32]C. Akcay, P. Parrein, and J. P. Rolland, "Estimation of longitudinal resolution in optical coherence imaging," Appl. Opt. **41**, 5256 (2002).
[33]T. H. Ko, D. C. Adler, J. G. Fujimoto, D. Mamedov, V. Prokhorov, V. Shidlovski, and S. Yakubovich, "Ultrahigh resolution optical coherence tomography imaging with a broadband superluminescent diode light source," Opt. Express **12**, 2112 (2004).
[34]C. E. Flores-Domínguez, R. Ochoa-Valiente, and L. A. García-Trujillo, "Low coherence optic source characterization," J. Phys.: Conf. Ser. **582**, 012043 (2015).
[35]H. Liang, R. Lange, B. Peric, and M. Spring, "Optimum spectral window for imaging of art with optical coherence tomography," Appl. Phys. B **111**, 589–602 (2013).
[36]C. Canavesi and J. P. Rolland, "Ten years of gabor-domain optical coherence microscopy," Appl. Sci. **9**, 2565 (2019).
[37]R.-A. Erdelyi, V.-F. Duma, C. Sinescu, G. M. Dobre, A. Bradu, and A. Podoleanu, "Dental diagnosis and treatment assessments: Between x-rays radiography and optical coherence tomography," Materials **13**, 4825 (2020).
[38]V. Damodaran, S. R. Rao, and N. J. Vasa, "Optical coherence tomography based imaging of dental demineralisation and cavity restoration in 840 nm and 1310 nm wavelength regions," Opt. Lasers Eng. **83**, 59–65 (2016).

17 March 2026 11:51:03

© Author(s) 2025

SUPPLEMENTARY MATERIAL

Broadband 2-µm superluminescent diodes with GaSb-based variable-thickness quantum wells

Ifte Khairul Alam Bhuiyan, [a] Joonas Hilska, Markus Peil, Jukka Viheriälä, and Mircea Guina

Optoelectronics Research Centre, Physics Unit, Tampere University, Korkeakoulunkatu 3, 33720, Tampere, Finland

a) Author to whom correspondence should be addressed: ifte.alambhuiyan@tuni.fi

Fig. S1 presents the calculated electronic band structure of the asymmetric quantum wells corresponding to the schematic in Fig. 2(b) of the main text. In addition to the conduction (CB) and valence band (VB) profiles, the figure includes the first quantized states and their corresponding confined wavefunctions for electrons, heavy holes, and light holes (wavefunctions are scaled for visibility). We also note the simulations agree in terms of transition wavelength with the data in Fig. 3 with reasonable accuracy (i.e. E1-HH1 transition).

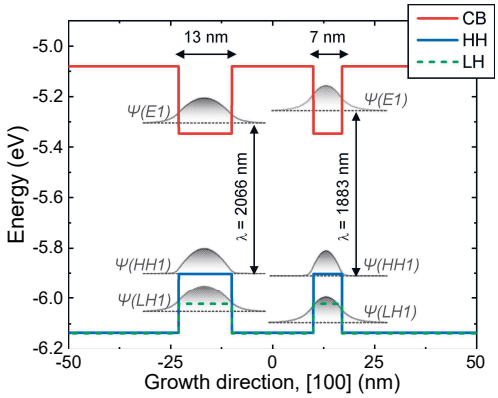


Fig. S1. Calculated conduction and valence band profiles of the active region. The first quantized electron $\psi(E1)$, heavy-hole $\psi(HH1)$, and light-hole $\psi(LH1)$ wavefunctions are overlaid. The growth direction axis is centered to the mid-point of the active region between the QWs.

Fig. S2 shows the recorded ASE spectrum at 200 mA in linear scales, to enable direct inspection of the ASE profile as shown in Fig. 5(b) in log scale. The linear-scale spectrum confirms the broadband profile across the combined bandwidth of ~132 nm, despite the presence of two partially overlapping peaks.

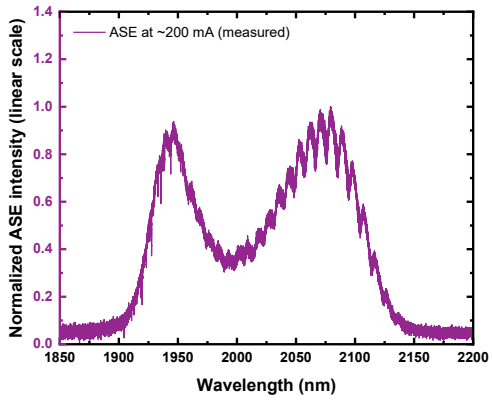


Fig. S2. ASE spectrum recorded at 200 mA in CW mode at 20°C corresponding to log scaled spectrum shown in Fig. 5(b) in the main manuscript.

Fig. S3 shows far-field profile recorded at 1000 mA CW injection current in RT. The 7° J-shaped SLD exhibits a clean, single-lobe far-field with ~40° (along fast-axis) and ~20° (along slow-axis) FWHM. The side-lobe-free beam profiles confirm transverse single mode operation of the J-shaped waveguide architecture implemented in the SLD device.

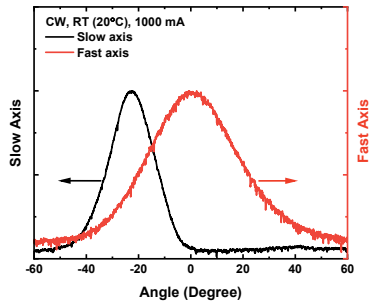


Fig. S3. Far-field (FF) profile of J-shaped SLD recorded at 1000 mA injection current operating under CW mode in RT. Recorded slow-axis and fast-axis beam profile are gaussian shaped and free of side-lobes confirms single mode transverse operation of the SLD.

Reference:

1. HAROLD by Photon Design (2023). [Online], https://photond.com/harold
2. Bhuiyan, I.K.A., Hilska, J., Peil, M., Viheriälä, J., Guina, M.: Design of broadband optical gain in GaSb-based waveguide amplifiers with asymmetric quantum wells. Optica Open. Preprint. (2025). https://doi.org/10.48550/arXiv.2508.17495
3. Cheung, C.S., Daniel, J.M.O., Tokurakawa, M., Clarkson, W.A., Liang, H.: Optical coherence tomography in the 2-μm wavelength regime for paint and other high opacity materials. Opt. Lett. 39, 6509 (2014). https://doi.org/10.1364/OL.39.006509
4. Marks, D., Carney, P.S., Boppart, S.A.: Adaptive spectral apodization for sidelobe reduction in optical coherence tomography images. J. Biomed. Opt. 9, 1281 (2004). https://doi.org/10.1117/1.1806471

PUBLICATION III

Design of broadband optical gain in GaSb-based heterostructures with asymmetric quantum wells

Ifte Khairul Alam Bhuiyan, Joonas Hilska, Markus Peil, Jukka Viheriälä, Mircea Guina

Optics Express **33**(26), 54154-54165, (2025)
DOI: 10.1364/OE.575782

Publication is licensed under a Creative Commons Attribution 4.0 International License CC-BY

Research Article | Vol. 33, No. 26 / 29 Dec 2025 / Optics Express 54154

Optics EXPRESS

Design of broadband optical gain in GaSb-based heterostructures with asymmetric quantum wells

IFTE KHAIRUL ALAM BHUIYAN,* JOONAS HILSKA, MARKUS PEIL, JUKKA VIHERIÄLÄ, AND MIRCEA GUINA

Optoelectronics Research Centre, Tampere University, Korkeakoulunkatu 10, 33720 Tampere, Finland
**ifte.alambhuiyan@tuni.fi*

Abstract: A design strategy for achieving broadband optical gain in GaSb-based semiconductor heterostructures operating beyond 2 µm is presented. By employing asymmetric GaInSb/AlGaAsSb quantum wells (QWs) of varying thicknesses, a flat and wide gain spectrum is demonstrated. The approach leverages carrier density and transition energy tuning across QWs to access various energy levels at specific current densities. Simulations using "Harold" self-consistent environment predict a full-width at half-maximum (FWHM) gain bandwidth exceeding 340 nm for a structure comprising one 7 nm and three 13 nm-thick QWs. The modelling parameters were validated against experimental data, ensuring a robust framework for gain engineering in broadband amplifiers and superluminescent diodes for mid-infrared applications.

Published by Optica Publishing Group under the terms of the Creative Commons Attribution 4.0 License. Further distribution of this work must maintain attribution to the author(s) and the published article's title, journal citation, and DOI.

1. Introduction

The development of optoelectronic devices operating at 2–3 µm spectral window has gained significant attention owing to an increasing number of sensing applications exploiting absorption-based molecular spectroscopy [1–4]. Moreover, if available with required performance, broadband light sources at this wavelength region could enable expansion of advanced imaging using optical coherence tomography (OCT) to new application areas, benefiting from reduced scattering at > 2 µm, and higher axial resolution linked to broadband emission [5–7]. At the same time, the 2 µm wavelength region aligns well with the transmission capabilities in thulium-doped fiber, potentially contributing to the development of free-space communication and LIDAR applications [8–10]. Finally, the recent progress of mid-infrared photonic integration technologies offers pathways to scale the production of these customized broadband devices with advanced functionalities integrated on-chip [11–14]. In general, these application areas would benefit from the availability of light sources that combine broad spectral coverage with high output power and electrical pumping. For example, a flat gain spectrum is highly desired for broadband tunable lasers allowing to decrease the variations in output power across the tuning range, or for broadband superluminescent diodes used in multi-wavelength spectroscopy and OCT imaging.

To this end, we exploit the versatility of bandgap engineering and investigate the use of asymmetric QWs to produce broadband gain profiles in GaSb-based heterostructures. Prior work at shorter wavelength regions, based on more conventional GaAs- and InP-based systems, has demonstrated the effectiveness of using bandgap engineering, strain engineering, and the variation of QW thicknesses to achieve broadened emission profiles [15–23]. Extending these design principles into the mid-infrared, specifically using GaSb-based material system, opens up compelling opportunities. Namely, GaInSb/AlGaAsSb QWs provide direct bandgap transitions with high radiative efficiency and flexibility for tuning the band structure through alloy composition and strain management [24,25]. By varying the number of QWs, their thicknesses, and the

#575782 https://doi.org/10.1364/OE.575782
Journal © 2025 Received 7 Aug 2025; revised 21 Nov 2025; accepted 24 Nov 2025; published 18 Dec 2025

Optics EXPRESS

surrounding barrier layers, it is possible to access various energy levels of confined states such that multiple energy transitions contribute to broadening the gain spectrum. However, given the large number of degrees of freedom in such structures, the design of broadband heterostructures requires systematic approach to optimize the gain features while taking into account physical design constraints. To this end, in this study we make use of advanced simulation tools (Harold; Photon Design [26]), taking into account carrier transport, and waveguiding optical confinement.

A simplified schematic of the simulated heterostructures used in the study is shown in Fig. 1. We first explore the simulation results with respect to single QW (SQW) structures with different thicknesses to observe basic trends setting the base of comparison with more advanced structures. Then these simulations are extended to double-QW (DQW) and multi-QW (MQW) configurations to evaluate the role of QW thickness variation in broadening the gain profile. Although it is somewhat marginal for the ultimate scope, our choice for engineering the bandgap based on changing the QW thickness instead of alloy composition is motivated by a higher accuracy in fabrication, i.e. higher precision in controlling the thickness.

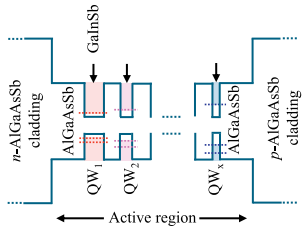


Fig. 1. Schematic of InGaSb/AlGaAsSb QW gain structure defining the generic design framework for simulation. The number of QWs and their individual thicknesses are varied during the optimization routine.

We would like to note that previous reports on using self-consistent simulations employing Harold simulator for heterostructures design operating at 2 μm wavelength range were confined to simulation of laser diodes, based on InP heterostructure operating at 2 μm [27], and GaSb heterostructures operating at 2.3 μm [28,29].

2. Methodology

The Harold simulation framework employs a self-consistent coupled-physics approach, solving Poisson's equation for electrostatic potential, current continuity equations for carrier transport, capture–escape balance equations for QW carrier dynamics, photon rate equations for optical field evolution as well as heat flow equations for thermal effects. The simulation tool computes the optical mode profile by solving the vertical and longitudinal wave equations, while the Schrödinger equation is applied to determine confined states in the QWs. The optical gain is evaluated using parabolic band approximation as described by Asada et al. [30]. The model accounts for carrier transport in MQW systems, resolving the spatial distributions of electron and hole densities for both confined (in QW) and unconfined (barrier/separate confinement heterostructure) carriers. A simplifying assumption is adopted, wherein carrier capture and escape times are treated as constants across all QWs, neglecting potential variations due to local strain or compositional fluctuations.

The bandgaps and general material parameters for the $Ga_{1-x}In_xSb$ and $Al_xGa_{1-x}As_ySb_{1-y}$ materials used in the heterostructures were taken from literature [31,32]. We simulate the gain structure in isothermal operation mode (pulsed mode). The temperature dependency of the

Optics EXPRESS

compound semiconductor band gaps were interpolated from the binary alloy parameters using the semi-empirical Varshni model [33].

The optical gain spectra of a single QW is evaluated by the simulator following the standard expression:

$$g(E_{phot.}) = \frac{\pi\hbar q^2}{ncm_e\varepsilon_0} M^2 \frac{1}{E} \sum_{j=1} K_{ij} A_{ij}(E_{phot.}) D_{ij}[F_j(E_{phot.}) - F_i(E_{phot.})] \tag{1}$$

where $E_{phot.}$ is the photon energy, K_{ij} is the overlap integral of the transition state i and j, A_{ij} is the dipole moment enhancement factor, n is the real part of the refractive index, q is the free electron charge, m_e is the electron mass, $\hbar$ is the plank's constant, ε_0 is the free space dielectric constant, c is the speed of light, M^2 is the dipole moment of the bulk material, $F_j(E_{phot.})$ and $F_i(E_{phot.})$ are fermi occupation factors, D_{ij} is the reduced density of states for the transition between j-th and i-th energy levels. Then the spontaneous emission rate is evaluated by

$$r_{sp}(E_{phot.}) = \frac{q^2 n^3 E_{phot.}}{\pi\hbar^2 m_e^2 c^3 \varepsilon_0} M^2 \sum_{j=1} K_{ij} D_{ij} F_j(E_{phot.})[1 - F_i(E_{phot.})] \tag{2}$$

and is consistent with the expression of gain model. The summation operation loop flows for all quantum confined states. Thus, the gain and the spontaneous emission spectrum are subsequently calculated using the following expressions:

$$G(\hbar\omega) = \int g(E_{phot.}) L(\hbar\omega - E_{phot.}) dE_{phot.} \tag{3}$$

$$R_{QW}^{sp}(\hbar\omega) = \int r_{sp}(E_{phot.}) L(\hbar\omega - E_{phot.}) dE_{phot.} \tag{4}$$

where $L(x)$ is the Lorentzian shape function. Broadening in gain and spontaneous emission expressions are based on convolution of gain and spontaneous emission rate with Lorentzian function, respectively.

Initially we designed a set of gain structures based on SQW and DQW. All active region of the gain structures included type-I compressively strained $Ga_{0.73}In_{0.27}Sb$ QWs, separated by 20 nm of $Al_{0.25}Ga_{0.75}As_{0.02}Sb_{0.98}$ barriers lattice matched to GaSb. The QWs were embedded within 130 nm waveguide material from both sides. The waveguide region was surrounded by ~1 µm thick n- and p-doped cladding layers consisting of higher band gap $Al_{0.5}Ga_{0.5}As_{0.04}Sb_{0.96}$ alloy, which is also lattice matched to GaSb. The epitaxial structure was finalized by a highly doped p-GaSb contact (cap) layer. The generic epitaxial structure is shown in Fig. 2; we show here only single QW on the figure. For double or multiple QW cases analyzed in the next sections, we used a 20 nm- $Al_{0.25}Ga_{0.75}As_{0.02}Sb_{0.98}$ barrier between adjacent QWs. The epitaxial structure was processed to define waveguide device configured as a broad-area (BA) laser diode (LD) structure with a stripe width of 80 µm and a cavity length of 2 mm.

In addition to simulating the lasing action, Harold allows evaluation of QW material gain and spontaneous emission characteristics by setting the reflectivities at both mirror facets close to zero (~10^{-7}). To validate the modeling parameters, we initially simulated the spontaneous emission and lasing characteristics of a structure incorporating a DQW gain region. The selected design was experimentally realized, and its optical properties were characterized through photoluminescence (PL) and LD characteristic measurements, which were then used as benchmark to adjust the key parameters of the simulator. Figure 3(a) shows the comparison fit for PL revealing an excellent matching in spontaneous emission peaks at ~1950nm and ~2090nm between the simulated and experimental structure. The calculated emission bandwidth is ~300 nm FWHM at a carrier density of ~3e17 cm^{-3}. Intensity mismatch on the shorter wavelength side is mainly due to atmospheric

Optics EXPRESS

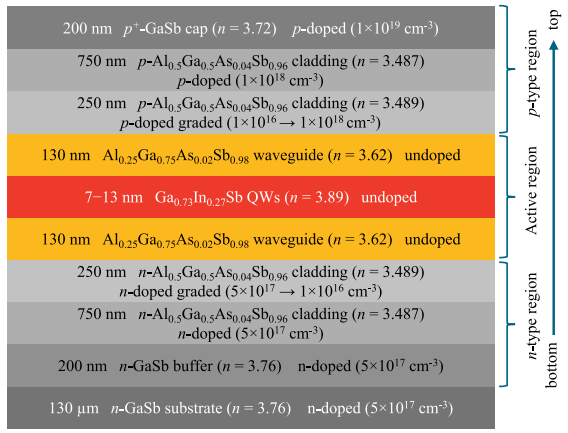


Fig. 2. Epitaxial layer structure and the key parameters considered in the simulated gain structures. The QW thickness varied from 7 nm to 13 nm. In case of double or multiple QWs, a 20 nm barrier with similar composition of waveguide was used between two adjacent QWs.

absorption, while minor discrepancies arise from experimental conditions (532 nm CW excitation at ~90 mW). To further validate the model, we simulated the performance of a broad-area laser diode (2 mm × 80 µm) incorporating the same DQW active region in heterostructure with slightly thicker cladding. Figure 3(b) compares the simulated and experimental light–current (L–I) characteristics under pulsed operation at room temperature. The inset in Fig. 3(b) presents the corresponding current–voltage (I–V) characteristics. The simulation shows again good agreement with the experimental threshold behavior and output power slope across the full bias range. These results support the validity of the simulation setting the relevant parameters used in simulation.

We note that for the BA-LD calibration step, both facets of the LD, with R_f and R_b being the front and back facet reflectivity, respectively were as-cleaved and uncoated, corresponding to $R_f = R_b \approx 0.32$. Top-view schematics of the lateral device structures used in the simulations are provided in Supplement 1. The numerical parameters used in the simulation are listed in the Table 1.

Table 1. Simulation parameters and their values

Parameter (symbol)	Value (unit)
Intraband relaxation time (τ_{in})	1e-13 s
Shockley-Read-Hall lifetime of electron (τ_{e-SRH})	1e-07 s
Shockley-Read-Hall lifetime of hole (τ_{h-SRH})	1e-07 s
Capture time constant of electron (τ_e^{cap})	5e-12 s
Capture time constant of hole (τ_h^{cap})	3e-13 s
Gain factor	0.6
Fraction of spontaneous emission coupled into optical mode	0.0001
Mirror reflectivity (both facets)	1e-07
Scattering loss (cm^{-1})	4.5

Optics EXPRESS

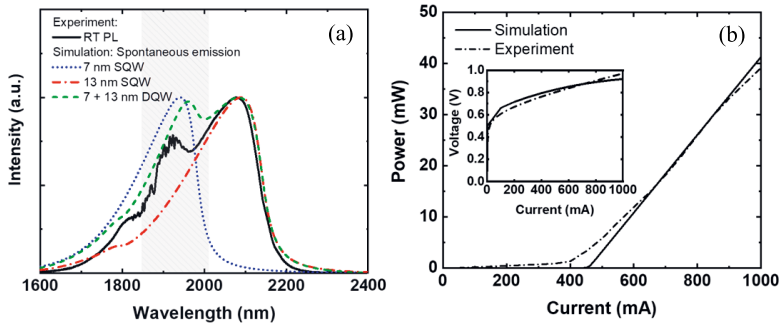


Fig. 3. (a) Room-temperature PL spectrum from a DQW gain structure with 7 nm and 13 nm wells. Simulated PL (green, short-dashed) is fitted for the same structure for carrier density ~3e17 cm^{-3}. Simulated gain spectra from 7 nm (blue, short-dotted) and 13 nm (red, dash-dotted) SQWs are also shown for comparison. The weak ripples near 1.85–1.9 µm (marked in grey) arise from atmospheric absorption related to water along optical path of the PL measurement system. (b) Experimental and simulated characteristics for the BA-LD structure with the same DQW heterostructure under pulsed operation.

3. Design and optimization of broadband gain structure with SQW and MQWs

We first simulated gain structures comprising SQW with different thickness of the QW, i.e, from 7 nm to 13 nm with one nm intervals. Then in a second iteration we simulated DQW structures with asymmetric QWs wherein the top QW thickness (see in Fig. 4) was fixed to 7 nm and the bottom QW varied in thickness from 7 nm to 13 nm, again with one nm intervals. A key aspect of the optimization was to understand the contribution for individual QWs to the gain spectrum, and their combined contributions in a DQW structure, and corresponding dependence on carrier

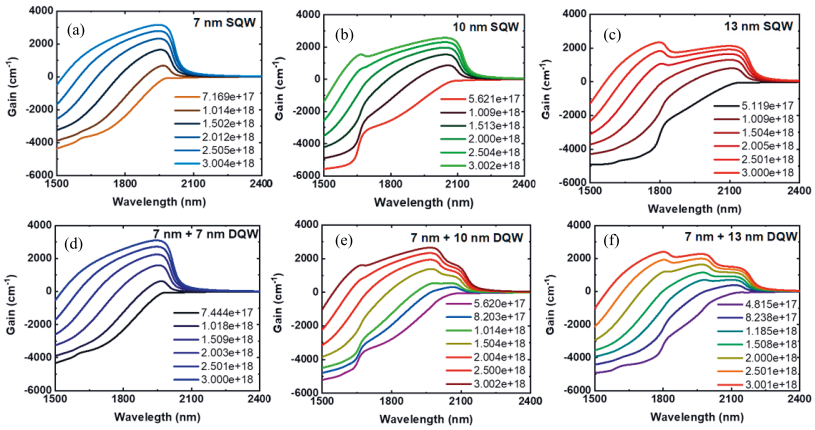


Fig. 4. Exemplary gain spectrum of different (a-c) SQWs of thickness 7 nm, 10 nm and 13 nm, and (d-f) DQWs with top QW thickness fixed to 7 nm, and bottom QW thickness of 7 nm, 10 nm, and 13 nm. All legends in the figures show the carrier density level in the QWs.

Optics EXPRESS

densities. Figure 4 summarizes the exemplary simulated gain curves at 20°C for SQW and DQW structures. The simulation reveal important distinctive features in the wavelength variation with carrier density, with clear transitions form gain peak corresponding to E1-HH1 QW transition to E1-LH1 transitions when carrier density increases.

Figure 5 summarizes the gain spectrum maxima (gain peak wavelength) variation with the carrier density. Up to a carrier density in the range of ~2.5e18 cm^{-3} (corresponding to a current injection level of ~1600 mA), the gain is dominated by the E1-HH1 transition for all SQW structures (see in Fig. 5(a)). Beyond this carrier density, significant contribution from the E1-LH1 transition appears. For example, in 13 nm QW, a sharp shift in the gain peak from 2097nm to 1800nm at ~2.6e18 cm^{-3} indicates the onset of broader gain spectra. Similar transition are observed in the 10 nm, 11 nm, and 12 nm SQWs at carrier densities exceeding ~3e18 cm^{-3}.

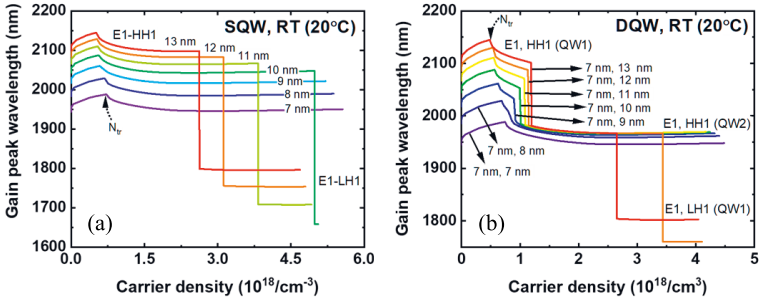


Fig. 5. Evolution of the QW gain peak wavelength as a function of carrier densities for (a) SQWs of different thicknesses varying from 7 nm to 13 nm. (b) Similar variation is shown for DQWs with the QW near the p-cladding is fixed to 7 nm, and the thickness of other QW is varied from 7 to 13 nm. In both cases N_{tr} specifies transparency carrier density level. The dominant E1–HH1 and E1–LH1 transitions are also indicated in each figure.

For the DQW gain structures (see in Fig. 5(b)), the simulations showed that at a carrier density of ~1.2e18 cm^{-3} both QWs exhibit gain maxima corresponding to E1-HH1 transition, which varies with QW thickness. Moreover, the DQW structures containing bottom QWs with thickness of 12 nm and 13 nm QWs showed clear E1-LH1 transition at ~1967nm for a carrier density of ~3.4e18 cm^{-3} and ~2.6e18 cm^{-3}, respectively. This E1-LH1 transition could not be seen for DQW structures with thinner "bottom" QWs, since we limit our simulation to injection current level of 10 A (corresponds to a carrier density of ~4.5e18 cm^{-3}); observation of the thinner QWs E1-LH1 transition would require higher carrier density, which is considered impractical. In general, our analysis shows that at a specific carrier density, a balanced gain condition can be achieved, wherein transitions from both QWs add to form a broad and flat gain spectrum. However, under higher injection levels, carrier occupation becomes higher in the thinner QW with larger density of states, resulting in a spectral shift of peak emission towards that QW.

Based on the observations made, several combinations of thicknesses employed in DQW heterostructures could be found for which wide and flat gain profile was achieved at specific carrier densities. For example, Fig. 6 shows simulated gain spectra having flat gain and wide spectral coverage for a DQW structure with fixed top QW of 7 nm, and bottom QW thickness varied from 9 nm to 13 nm. The peak gain corresponding to the 7 nm QW is always near ~1980nm, while the gain peak for thicker QW changes from ~2030nm to ~2100 nm with the thickness. A maximum gain bandwidth of ~256 nm FWHM can be achieved for a combination of 7 nm and 13 nm QWs at higher carrier density of N = 1.2e18 cm^{-3} (corresponds to ~340 mA current injection). In this case a maximum gain of ~710 cm^{-1} is maintained between 1953nm and 2140 nm, with a

Optics EXPRESS

variation of ~70 cm^{-1} in the overlapping region of the different contributions to the total gain spectra.

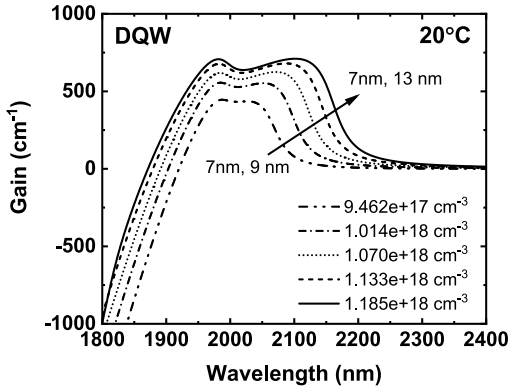


Fig. 6. Flat gain spectrum obtained for asymmetric DQW structures employing a fixed bottom QW with a thickness of 7 nm and a top QW with varying thickness from 10 nm to 13 nm (varying in 1 nm intervals in increasing order as highlighted by the arrow). The legend denotes the carrier density ($cm^{-}3$) levels for this simulation.

To further extend the spectral bandwidth and emission power, we simulated MQW devices with more than two QWs, while keeping the total QW thickness below strain relaxation. More specifically, we set a total strain-times-thickness limit of around 100%×nm as a rough estimate based on available data for GaInSb [25] and AlGaAsSb [24] strain relaxation when grown on GaSb substrate. Within these constraints, the MQW structures were systematically optimized to achieve a balance between spectral flatness and bandwidth (in FWHM) of the gain spectrum at high carrier density.

Figure 7 shows flat gain spectra at RT from three different structures: A, B and C, comprising two different types of QW thickness (7 nm and, 13 nm) with uniform composition. Structure A corresponds to the DQW structure analyzed in Fig. 3 and acts as the reference. Structure B includes one additional 13 nm QW compared to structure A and shows an improved flat gain level from 706 cm^{-1} to 1032 cm^{-1} at an elevated carrier density. Moreover, structure C that comprising one 7 nm and three 13 nm QWs produces a yet broader gain profile, at a higher carrier density level compared to other structures. We limit inclusion of additional QWs in the simulation to not exceed the critical strain limit in the active region. We note employing strain-compensation architectures [34,35] could be utilized for further optimization however that is considered out-of-scope for this work.

The simulation shows that the thin QW contributes to gain at shorter wavelengths (around ~1980nm), while the thicker QWs dominate in the longer-wavelength region (around ~2100 nm) at a carrier density level of ~1.73e18 cm^{-3} (corresponds to ~2.1 A injection current). Maximum flat gain level (red shaded region in gain spectra of Fig. 7) for structure C covers a wavelength range ~185 nm (from ~1950nm to ~2135 nm) with a gain fluctuation of 73 cm^{-1}. The calculated maximum gain is ~1253 cm^{-1}, which is approximately two-fold improvement compared to reference gain structure A. The gain spectrum for structure C shows double gain peaks around ~1987nm and ~2096nm due to the combined energy transition from the four QWs. The maximum bandwidth of the gain spectra from the optimized structure C has a FWHM of ~342 nm, which is approximately 100 nm broader compared to structure A.

Optics EXPRESS

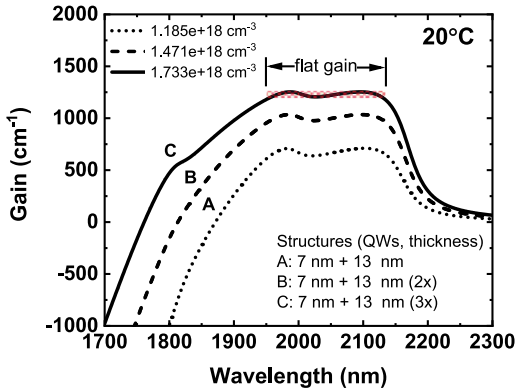


Fig. 7. Simulated gain spectra for various MQW designs.

Figure 8(a) shows simulation of RT gain spectra at different carrier densities for structure C. At a moderate carrier density level ~1e18 cm^{-3}, peak gain appears near ~2100 nm only due to dominant carrier transition from 13 nm QWs. As mentioned earlier, flat and balanced gain spectra appear around ~1.73e18 cm^{-3} having distinguishable double peaks with a relative small dip in between. However, at a higher carrier density level of ~2.14e18 cm^{-3}, the gain extends to shorter wavelength region around ~1800nm with a degraded flatness. The third peak around ~1800nm is generated due to excitation from higher energy levels favoring the thicker QW.

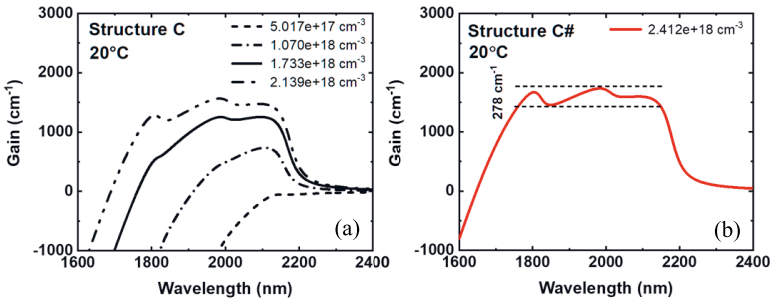


Fig. 8. (a) Simulated gain spectra for structure C at different carrier densities. (b) Gain spectra of structure C# for a modified waveguide/cavity length (1775μm) at a specific carrier density (at N = 2.412e18 cm^{-3}) showing elevated gain for E1-HH1 transition from all QWs as well as E1-LH1 transition from 13 nm QW.

Figure 8(b) shows the gain profiles for structure C# but for a shorter device. Here the length of the active waveguide (current injection region) was reduced from 2 mm to 1775μm to, while 225 μm of the waveguide end was not pumped to implement a mirror loss of ~95 cm^{-1} without modifying the facet reflectivity. In practice, this strategy allows us to suppress cavity feedback while preventing lasing and allows us to use higher injection densities to access E1-LH1 transition. In this case, the gain enhancement is primarily attributed to the contribution of the second quantized state originating from the thicker quantum well (QW), at a carrier density of N = 2.412e18 cm^{-3} (corresponds to ~4.4 A). We would note that Mehuys *et al.* [36] employed a

Optics EXPRESS

similar strategy to enhance gain bandwidth by optimizing cavity loss to enable lasing from both the n = 1 and n = 2 quantum states, resulting in a broadened and flattened gain spectrum. The fluctuation in the non-uniformity or flatness corresponds to QW gain variation of ~278 cm^{-1} over a broad spectral window spanning 1760–2150 nm. The peak gain values are calculated as ~1600 cm^{-1} at ~2100 nm (E1-HH1, 13 nm QW), ~1733cm^{-1} at 1980nm (E1-HH1, 7 nm QW), ~1670 cm^{-1} at 1800nm (E1-LH1, 13 nm QW). This optimization yields a gain enhancement of approximately 400–500 cm^{-1} for both thick and thin QWs, respectively.

A very important aspect for practical device operation is temperature dependencies. Figure 9 shows simulated gain spectrum at temperatures between 10°C and 100°C, revealing the change of the carrier density required to attain a flat gain spectral characteristic. Owing to the temperature increase, the gain peak at the sorter wavelength region increased from 1970nm to 2113 nm, while for the longer wavelength region of the gain peak increased from 2078nm to 2237 nm. Moreover, the FWHM of the gain spectra varies from ~335 nm to a maximum ~400 nm as temperature increases. However, as expected, the maximum gain was significantly reduced (~195 cm^{-1}) with increasing temperature.

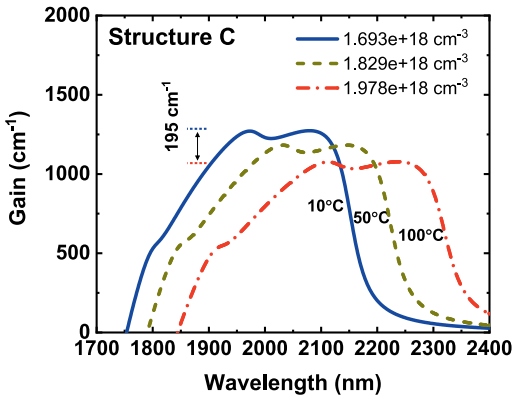


Fig. 9. Temperature dependency of the gain spectra for structure C.

At an elevated injection, charge carriers tend to populate at the thinner QW due to its stronger confinement and higher density of state (DOS) at the ground state, resulting in higher optical gain relative to the thicker well. This behavior leads to spectral tilt and reduced uniformity in gain spectrum and underscores a fundamental trade-off: while increasing the number of QW can enhance overall gain and broaden the emission spectrum, it does not guarantee proportionally higher gain especially when carrier distribution becomes increasingly non-uniform across the wells. Further optimization of the gain structure to achieve better carrier uniformity may include the use of energy barriers between groups of QWs to minimize carrier leakage and improve carrier confinement.

It should be noted that the present work focuses on heterostructure-level gain engineering rather than device-level amplifier operation. The calculated gain coefficients already incorporate the relevant absorption and emission processes, so the broadband flat-gain profiles obtained under optimized bias conditions are directly indicative of the achievable emission spectra in corresponding devices. Any residual re-absorption between wells is inherently accounted for in the gain model and does not significantly distort the spectral flatness.

Optics EXPRESS

Table 2 summarizes the key parameters of the simulated structures and their performance with respect to simulated gain properties at specific carrier densities. More specifically, it comprises the gain peak wavelengths, gain bandwidth in FWHM, as well as the peak gain value.

Table 2. Key parameters of simulated heterostructures

Type	Number of QWs	Thicknesses of QWs (nm)	Carrier density (cm^{-3})	Peak wavelength (nm)	FWHM gain (nm)	Peak gain (cm^{-1})
SQW	1	7	1.014×10^{18}	1967	85	683
SQW	1	10	1.009×10^{18}	2057	166	861
SQW	1	13	1.009×10^{18}	2110	175	805
DQW	2	7 + 7	1.018×10^{18}	1967	87	630
DQW	2	7 + 10	1.014×10^{18}	1985, 2052	170	555
DQW (A)	2	7 + 13	1.185×10^{18}	1980, 2102	256	710
MQW (B)	3	7 + 2 × 13	1.471×10^{18}	1983, 2098	298	1034
MQW (C)	4	7 + 3 × 13	1.733×10^{18}	1988, 2096	342	1253
MQW (C#)	4	7 + 3 × 13	2.412×10^{18}	1804, 1983, 2088	473	1700

As shown in Table 2, the three SQW structures based on 7 nm to 13 nm wells exhibit a clear dependence of gain and bandwidth on QW thickness. Increasing the QW thickness from 7 nm to 10 nm and to 13 nm shifts the peak wavelength to longer values and increases the peak gain. The DQW designs (7 nm + 7 nm and 7 nm + 10 nm) provide only modest improvements, while the asymmetric 7 nm + 13 nm structure (DQW A) produces a noticeably broader gain spectrum. Extending the asymmetric concept to three- and four- QW heterostructures yields further gain bandwidth enhancement and higher peak gain. Among all designs, the optimized 7 nm + 3 × 13 nm structure (C, and C#) shows the highest gain and the broadest FWHM bandwidth, confirming the effectiveness of asymmetric MQW configurations.

Combining the simulation with physically realizable structural design, this study shows a pathway to develop broadband gain devices in the 2 µm wavelength region and beyond. The insights herein also bridge a critical gap between understanding the theoretical potential of these novel broadband devices, while minimizing the need for extensive experimental iterations of device development.

4. Conclusion

A design strategy for achieving broadband optical gain in GaSb-based semiconductor heterostructures operating beyond 2 µm was proposed. Through systematic bandgap engineering, we explored the impact of varying QW thicknesses within asymmetric MQW heterostructures on the gain spectrum. To this end we used a validated self-consistent simulation with the Harold framework. Our analysis revealed that the use of asymmetric GaInSb/AlGaAsSb QWs enables broader gain spectrum by exploiting the interplay between carrier density-dependent energy transitions (corresponding to E1-HH1 and E1-LH1 transitions) in different QWs.

Simulations of both SQW and DQW structures established the relationship between carrier injection levels and the onset of multi-transition gain contributions. Notably, a MQW structure with one 7 nm and three 13 nm QW was found to deliver a flat and wide gain profile, maintaining a high gain (~1253 cm^{-1}) across a spectral range of ~1953–2140 nm with a full-width at FWHM exceeding 340 nm for room-temperature operation. Furthermore, the simulations revealed the effects of temperature increase, demonstrating the possibility for even broadening the gain spectrum with a FWHM of ~400 nm at ~100°C at the expense of reduced gain. The simulation results were validated against experimental data obtained from PL and LD characterization,

Optics EXPRESS

confirming the accuracy of the modeling parameters and supporting the practicality of the proposed design approach. Future work will focus on further expanding the gain bandwidth through the inclusion of additional QWs with optimized thickness and strain profiles, aiming also at wavelength extension towards 3 µm.

Funding. Research Council of Finland (320168); Horizon 2020 Framework Programme (860807); HORIZON EUROPE Framework Programme (101139777-2).

Acknowledgement. The authors acknowledge Dr. Topi Uusitalo, and Dr. Nouman Zia for fruitful discussion on the simulation.

Disclosures. The authors declare no conflicts of interest.

Data availability. Data underlying the results presented in this paper can be obtained from the authors upon reasonable request.

Supplemental document. See Supplement 1 for supporting content.

References

1. K. Vizbaras, E. Dvinelis, I. Šimonytė, *et al.*, "High power continuous-wave GaSb-based superluminescent diodes as gain chips for widely tunable laser spectroscopy in the 1.95–2.45 µm wavelength range," Appl. Phys. Lett. **107**(1), 011103 (2015).
2. A. Vizbaras, I. Šimonytė, A. Miasojedovas, *et al.*, "Swept-wavelength lasers based on GaSb gain-chip technology for non-invasive biomedical sensing applications in the 1.7–2.5 µm wavelength range," Biomed. Opt. Express **9**(10), 4834 (2018).
3. N. Zia, J. Viheriälä, E. Koivusalo, *et al.*, "GaSb superluminescent diodes with broadband emission at 2.55 µm," Appl. Phys. Lett. **112**(5), 051106 (2018).
4. S. Ojanen, J. Viheriälä, N. Zia, *et al.*, "Discretely Tunable (2594, 2629, 2670 nm) GaSb/Si3N4 Hybrid Laser for Multiwavelength Spectroscopy," Laser & Photonics Reviews **17**(12), 2300492 (2023).
5. H. Liang, R. Lange, B. Peric, *et al.*, "Optimum spectral window for imaging of art with optical coherence tomography," Appl. Phys. B **111**(4), 589–602 (2013).
6. C. S. Cheung, J. M. O. Daniel, M. Tokurakawa, *et al.*, "High resolution Fourier domain optical coherence tomography in the 2 µm wavelength range using a broadband supercontinuum source," Opt. Express **23**(3), 1992 (2015).
7. M. Read, C. S. Cheung, H. Liang, *et al.*, "A Non-invasive Investigation of Egyptian Faience Using Long Wavelength Optical Coherence Tomography (OCT) at 2 µm," Studies in Conservation **67**(3), 168–175 (2022).
8. Z. Li, A. M. Heidt, J. M. O. Daniel, *et al.*, "Thulium-doped fiber amplifier for optical communications at 2 µm," Opt. Express **21**(8), 9289–9297 (2013).
9. L. Flannigan, L. Yoell, and C. Xu, "Mid-wave and long-wave infrared transmitters and detectors for optical satellite communications—a review," J. Opt. **24**(4), 043002 (2022).
10. S. Chin, J. Holzer, A. D. Groote, *et al.*, "Development of hybrid photonic integrated wavelength-tunable laser at 2 µm and its application to FMCW LiDAR," Opt. Express **32**(13), 22470 (2024).
11. N. Zia, S.-P. Ojanen, J. Viheriala, *et al.*, "Widely tunable 2 µm hybrid laser using GaSb semiconductor optical amplifiers and a Si_3N_4 photonics integrated reflector," Opt. Lett. **48**(5), 1319 (2023).
12. E. Tournié, L. Monge Bartolome, M. Rio Calvo, *et al.*, "Mid-infrared III–V semiconductor lasers epitaxially grown on Si substrates," Light: Sci. Appl. **11**(1), 165 (2022).
13. A. Remis, L. Monge-Bartolome, M. Paparella, *et al.*, "Unlocking the monolithic integration scenario: optical coupling between GaSb diode lasers epitaxially grown on patterned Si substrates and passive SiN waveguides," Light: Sci. Appl. **12**(1), 150 (2023).
14. S. Ojanen, J. Viheriälä, N. Zia, *et al.*, "Widely Tunable (2.47–2.64 µm) Hybrid Laser Based on GaSb/GaInAsSb Quantum-Wells and a Low-Loss Si3N4 Photonic Integrated Circuit," Laser & Photonics Reviews **17**(7), 2201028 (2023).
15. O. Mikami, H. Yasaka, and Y. Noguchi, "Broader spectral width InGaAsP stacked active layer superluminescent diodes," Appl. Phys. Lett. **56**(11), 987–989 (1990).
16. Ching-Fuh Lin, Bor-Lin Lee, and Po-Chien Lin, "Broad-band superluminescent diodes fabricated on a substrate with asymmetric dual quantum wells," IEEE Photonics Technol. Lett. **8**(11), 1456–1458 (1996).
17. M. J. Hamp and D. T. Cassidy, "Critical design parameters for engineering broadly tunable asymmetric multiple-quantum-well lasers," IEEE J. Quantum Electron. **36**(8), 978–983 (2000).
18. J. Wang, M. J. Hamp, and D. T. Cassidy, "Design Considerations for Asymmetric Multiple Quantum Well Broad Spectral Width Superluminescent Diodes," IEEE J. Quantum Electron. **44**(12), 1256–1262 (2008).
19. M. J. Hamp, D. T. Cassidy, B. J. Robinson, *et al.*, "Effect of barrier thickness on the carrier distribution in asymmetric multiple-quantum-well InGaAsP lasers," IEEE Photonics Technol. Lett. **12**(2), 134–136 (2000).
20. C.-F. Lin, B.-R. Wu, L.-W. Laih, *et al.*, "Sequence influence of nonidentical InGaAsP quantum wells on broadband characteristics of semiconductor optical amplifiers–superluminescent diodes," Opt. Lett. **26**(14), 1099 (2001).
21. C.-W. Tsai, Y.-C. Chang, G. S. Shmavonyan, *et al.*, "Extremely broadband superluminescent diodes/semiconductor optical amplifiers in optical communication band," in M. J. F. Digonnet, ed. (2003), p. 69.

Optics EXPRESS

22. O.-K. Kwon, K. Kim, E.-D. Sim, *et al.*, "Asymmetric multiple-quantum-well laser diodes with wide and flat gain," Opt. Lett. **28**(22), 2189 (2003).
23. T. Ohgoh, A. Mukai, J. Yaguchi, *et al.*, "Demonstration of 1.0 µm InGaAs High-Power and Broad Spectral Bandwidth Superluminescent Diodes by Using Dual Quantum Well Structure," Appl. Phys. Express **6**(1), 014101 (2013).
24. J. L. Lazzari, C. Fouillant, P. Grunberg, *et al.*, "Critical layer thickness in AlGaAsSbGaSb heterostructures determined by X-ray diffraction," J. Cryst. Growth **130**(1-2), 96–100 (1993).
25. T. A. Nilsen, M. Breivik, E. Selvig, *et al.*, "Critical thickness of MBE-grown Ga1−xInxSb (x<0.2) on GaSb," J. Cryst. Growth **311**(7), 1688–1691 (2009).
26. "HAROLD by Photon Design (2023). [Online]," (n.d.).
27. A. Al-Muhanna and A. Salhi, "Numerical analysis of InGaAs–InP multiple-quantum well laser emitting at 2 µm," Opt. Quant. Electron. **46**(7), 851–861 (2014).
28. L. Chenini, A. Aissat, M. Halbwax, *et al.*, "Performance simulation of an InGaSb/GaSb based quantum well structure for laser diode applications," Physics Letters A **467**, 128711 (2023).
29. A. Salhi and A. A. Al-Muhanna, "Self-Consistent Analysis of Quantum Well Number Effects on the Performance of 2.3-µm GaSb-Based Quantum Well Laser Diodes," IEEE J. Select. Topics Quantum Electron. **15**(3), 918–924 (2009).
30. M. Asada, A. Kameyama, and Y. Suematsu, "Gain and intervalence band absorption in quantum-well lasers," IEEE J. Quantum Electron. **20**(7), 745–753 (1984).
31. J. Piprek, *Semiconductor Optoelectronic Devices : Introduction to Physics and Simulation*, 1st ed. (Academic Press, 2003).
32. I. Vurgaftman, J. R. Meyer, and L. R. Ram-Mohan, "Band parameters for III–V compound semiconductors and their alloys," J. Appl. Phys. **89**(11), 5815–5875 (2001).
33. Y. P. Varshni, "Temperature dependence of the energy gap in semiconductors," Physica **34**(1), 149–154 (1967).
34. W. Li, J. B. Héroux, H. Shao, *et al.*, "Strain-compensated InGaAsSb/AlGaAsSb mid-infrared quantum-well lasers," Appl. Phys. Lett. **84**(12), 2016–2018 (2004).
35. W. Li, H. Shao, D. Moscicka, *et al.*, "Strain-compensated InGaAsSb multiple quantum-wells with digital AlGaAsSb barriers for midinfrared lasers," IEEE Photonics Technol. Lett. **17**(11), 2274–2276 (2005).
36. D. Mehuys, M. Mittelstein, A. Yariv, *et al.*, "Optimised Fabry-Perot (AlGa)As quantum-well lasers tunable over 105 nm," Electron. Lett. **25**(2), 143–145 (1989).

Supplemental Document

Optics EXPRESS

Design of broadband optical gain in GaSb-based heterostructures with asymmetric quantum wells: supplement

IFTE KHAIRUL ALAM BHUIYAN,* JOONAS HILSKA, MARKUS PEIL, JUKKA VIHERIÄLÄ, AND MIRCEA GUINA

Optoelectronics Research Centre, Tampere University, Korkeakoulunkatu 10, 33720 Tampere, Finland
**ifte.alambhuiyan@tuni.fi*

This supplement published with Optica Publishing Group on 18 December 2025 by The Authors under the terms of the Creative Commons Attribution 4.0 License in the format provided by the authors and unedited. Further distribution of this work must maintain attribution to the author(s) and the published article's title, journal citation, and DOI.

Supplement DOI: https://doi.org/10.6084/m9.figshare.30702935

Parent Article DOI: https://doi.org/10.1364/OE.575782

DESIGN OF BROADBAND OPTICAL GAIN IN GASB-BASED HETEROSTRUCTURES WITH ASYMMETRIC QUANTUM WELLS: SUPPLEMENTAL DOCUMENT

Fig. S1 shows the schematic top view of the lateral structure (heterostructure gain device) layouts used in Harold simulation. Fig. S1(a) illustrates the general configuration common to all simulated structures.Fig. S1(a) shows general configuration of all the structures. Fig. S1(b) shows the specific layout of the optimized C# structure, which includes a short unpumped section (grey) near one facet, doesn't contain p-metal layers for 225 µm length on top of the structure. The 80 µm wide waveguide strip (deep sea blue) area also contain the p-metal layers (orange) to enable uniform current injection. The wire bond pads (dark orange) are on top of the p-metal layers to inject current to the devices.

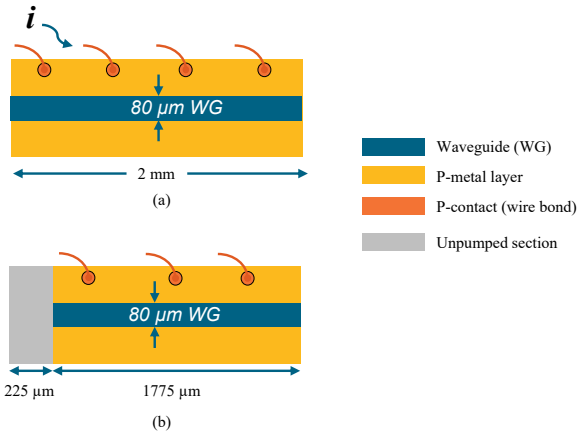


Fig. S1. Top-view schematic of the lateral device structure layouts. (a) General configuration of all simulated gain structures. (b) Layout of the optimized C# structure, showing the 225-µm unpumped section (grey) where the p-metal is intentionally omitted. The 80-µm-wide ridge waveguide (blue) is covered by p-metal contacts (orange), with wire-bond pads (dark orange) providing current injection.

PUBLICATION IV

Time-domain optical coherence tomography at 2 μm using GaSb-based broadband superluminescent diode

Ifte Khairul Alam Bhuiyan, Alejandro Martinez Jimenez, Ramona Cernat, Adrian Fernandez Uceda, Joonas Hilska, Markus Peil, Manuel Jorge Marques, George Dobre, Jukka Viheriälä, Adrian Podoleanu, Mircea Guina

Optics Express, **34** (10), 17833-17846, (2026)
DOI: 10.1364/OE.592137

Publication is licensed under a Creative Commons Attribution 4.0 International License CC-BY

Research Article Vol. 34, No. 10 / 18 May 2026 / Optics Express 17833
Optics EXPRESS

Time-domain optical coherence tomography at 2 µm using GaSb-based broadband superluminescent diode

IFTE KHAIRUL ALAM BHUIYAN,[1,5,*] ALEJANDRO MARTÍNEZ JIMÉNEZ,[2] RAMONA CERNAT,[3] ADRIÁN FERNÁNDEZ UCEDA,[3] JOONAS HILSKA,[1] MARKUS PEIL,[1] MANUEL JORGE MARQUES,[3] GEORGE DOBRE,[3] JUKKA VIHERIÄLÄ,[4] ADRIAN PODOLEANU,[3] AND MIRCEA GUINA[1]

[1]*Optoelectronics Research Centre, Physics Unit, Tampere University, Korkeakoulunkatu 3, 33720 Tampere, Finland*
[2]*Department of Physical Sciences, University de Castilla-La Mancha (UCLM), 45004 Toledo, Spain*
[3]*Applied Optics Group, Engineering, Mathematics and Physics School, University of Kent, Canterbury CT2 7NH, UK*
[4]*Advanced Microelectronics Packaging Group, Faculty of Information Technology and Communication Sciences, Tampere University, Korkeakoulunkatu 10, 33720 Tampere, Finland*
[5]*Department of Physical Sciences, Independent University, Bangladesh, Plot 16, Block B, Aftabuddin Ahmed Road, Bashundhara R/A, Dhaka – 1229, Bangladesh*
[*]*ifte.alambhuiyan@tuni.fi*

Abstract: We report a time-domain optical coherence tomography (TD-OCT) system operating in the 2 µm spectral region, enabled by a GaSb-based superluminescent diode (SLD). The spectrum emitted by the SLD exhibits a full-width half-maximum (FWHM) of ~80 nm centered near 2.1 µm. For OCT operation, stable amplified spontaneous emission with low spectral ripple (<20%) is maintained at drive currents below 150 mA. The SLD is fiber coupled and integrated into a fiber-based Michelson interferometer. In the OCT system, the measured coherence envelope yields an axial resolution of approximately 300 µm in air and enables depth-resolved imaging of scattering paint-based coating samples. In contrast to OCT implementations at 2 µm wavelength region that commonly rely on supercontinuum sources, the use of GaSb-based SLDs offers a compact, practical alternative, leveraging the maturity and scalability of electrically driven semiconductor light sources packaged in a standard "butterfly" module. This report represents the first demonstration of TD-OCT imaging at 2 µm using a GaSb-based SLD source and establishes its suitability for compact and scalable mid-IR OCT instrumentation targeting non-biological, low-water-content materials.

Published by Optica Publishing Group under the terms of the Creative Commons Attribution 4.0 License. Further distribution of this work must maintain attribution to the author(s) and the published article's title, journal citation, and DOI.

1. Introduction

Optical coherence tomography (OCT) utilizes low-coherence interferometry to perform non-invasive imaging with micrometer-scale resolution and millimeter-scale penetration depth, enabling to retrieve the 3D cross-sectional profile of tissue microstructure [1]. Axial resolution depends on the coherence length of the light source, and the penetration depth depends on the scattering and absorption of the object at the imaging wavelength. While OCT systems operating at 800 nm, 1060 nm, and 1300 nm are mature and have enabled significant advancements in vivo medical diagnosis [2–4], there is growing interest in imaging non-biological structures exploiting light sources emitting at longer wavelengths [4]. OCT in longer spectral region exhibits

#592137 https://doi.org/10.1364/OE.592137
Journal © 2026 Received 30 Jan 2026; revised 29 Mar 2026; accepted 2 Apr 2026; published 6 May 2026

Optics EXPRESS

substantial advantages, as optical scattering coefficients generally can be assumed to exhibit inverse dependence on wavelength for many heterogeneous non-biological materials [5], leading to improved penetration depth compared to shorter wavelengths.

Present commercial OCT systems mostly operate at 800 nm, 1060 nm or 1300 nm, benefiting from the minimal water absorption in biological tissues and availability of mature optical components developed for telecommunication applications. While the initial development in OCT at these wavelengths have been triggered by medical applications [6], there is an increasing trend to extend its application towards nondestructive testing and characterization. Application examples include damage inspection of polymer and composites [7,8], ceramic layer characterization [9], monitoring of the thicknesses of thin coatings [10], velocity measurements of fluids [11], forensic document inspection [12], and dielectric coating inspection [13]. In these applications, the materials typically exhibit low water content, and hence they do not impose operational wavelength restrictions in terms of water absorption that is a common issue in biological samples. Additionally, while these materials under study generally have multiple scattering events resulting in noise, speckling and blurring can still compromise imaging quality at shorter wavelengths. Additionally, multiple scattering events and speckle compromise imaging quality at shorter wavelengths. While shorter-wavelength OCT systems (e.g., UV/blue region) can achieve sub-micron axial resolution and are attractive for high-precision surface inspection, their application required high degree of safety concern [14,15]. In contrast, longer-wavelength OCT systems operating near 2 µm offer improved subsurface imaging capability in non-biological materials due to lower scattering losses, without any risk of hazardous radiation [16].

Therefore, to improve imaging fidelity, OCT operations have recently extended to the 2 µm spectral band, with already demonstrated notable outcomes [13,16,17]. However, these OCT systems have predominantly employed supercontinuum (SC) sources, which while providing high output power and extremely broad bandwidths, exhibit noise and bring limitation in terms of complexity, size, and cost.

As an alternative to SC sources, superluminescent diodes (SLDs) are semiconductor-based compact broadband light sources that have been utilized extensively in time domain (TD) and spectral domain (SD) OCT systems [18–20]. An SLD generates amplified spontaneous emissions (ASE) using a single- or double-pass optical channel [21]. Furthermore, when purposely designed to avoid waveguide reflections, they can emit a smooth near-Gaussian ASE spectrum with spectral modulation sufficiently suppressed within a large bandwidth (i.e. approaching 100 nm at -3 dB). This leads to a clean axial point-spread function (PSF), which represents an important instrumental feature in OCT imaging. These properties together with benefits of low power consumption, availability as standard fiber-coupled modules, reduced system complexity and leveraging the scalability of semiconductor fabrication are key reasons for SLDs enabling wider spread of OCT technology.

In this work, the use of a GaSb-based SLD for TD-OCT operating in the 2 µm wavelength region is investigated. Such miniaturized light-sources have recently raised attention owing to their ability to provide broadband emission across the 2–3 µm range, supporting not only OCT but also multispecies spectroscopic applications [22–27]. In particular, we report the development of a fiber-based TD-OCT system incorporating a GaSb SLD emitting near 2.05 µm and evaluate its performance for imaging non-biological samples. The system is implemented using single-mode fiber interferometry, which simplifies optical alignment and facilitates compact integration. In our experiment, the spectral and coherence properties of the GaSb SLD are characterized and reported as a function of injection currents, aiming at quantifying their impact on the axial resolution and OCT image quality in the presence of fiber packaging penalties. Imaging experiments on layered scattering phantoms and painted samples are conducted to assess the practical capability of the system. This work further aims to evaluate the potential of GaSb SLDs as practical sources for

Optics EXPRESS

compact OCT systems in the mid-IR region, with relevance to non-destructive inspection and related imaging scenarios where SC sources may be impractical.

2. General performance assessment of 2 µm OCT systems

The axial resolution in a TD-OCT system is fundamentally determined by the coherence length of the light source, which is inversely proportional to its spectral bandwidth. For a source with Gaussian spectrum, axial resolution in a medium of refractive index n is approximated as [28–30]:

$$\Delta z \approx \frac{2\ln(2)}{\pi}\frac{\lambda_0^2}{n\cdot\Delta\lambda} \tag{1}$$

where λ_0 is the central wavelength and $\Delta\lambda$ is the FWHM bandwidth. This estimation assumes a smooth source spectrum at the OCT interferometer input and therefore represents an upper band on the achievable axial resolution. Based on this analytical estimation, Fig. 1 illustrates the theoretical axial resolution in air (FWHM of the coherence envelope) for OCT sources centered at 2 µm as a function of spectral FWHM bandwidth for refractive indices ranging from $n = 1.0$ (air) to higher-index media, such as, polymers, ceramics, or glasses where refractive index often ranges from ~1.3 to above ~2.5. The figure also shows an exponentially decayed trend where the axial resolution improves with increasing spectral bandwidth; the axial resolution is also better for higher refractive index media. However, dense medium with higher refractive index n scales down the effective axial resolution ($\Delta z_n = \Delta z/n$).

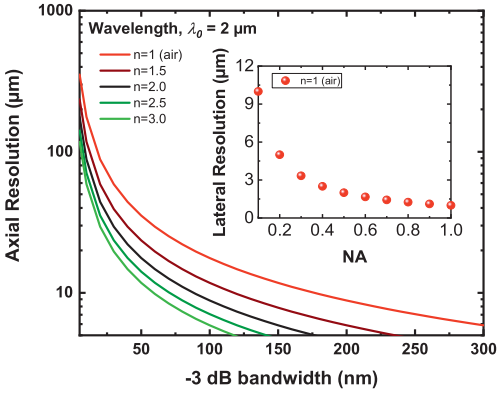


Fig. 1. Theoretical axial resolution for operation near 2 µm as a function of -3 dB FWHM spectral bandwidth for different refractive indices. Inset shows lateral resolution in air (n = 1) at 2 µm vs numerical aperture (NA), illustrating the lateral spot size and depth of focus.

Unlike biological tissues, where high water content dominates absorption at 2 µm and limits penetration, non-biological materials generally contain little to no water. Their optical performance is instead governed by scattering, refractive index contrast, and the presence of vibrational absorption bands. Scattering strength depends on the relative size of scattering features to wavelength, being a combination of Rayleigh scattering for sizes smaller than a wavelength (decreasing roughly with λ^{-4} [5]) and Mie scattering for larger features than the wavelength, where scattering maybe independent to wavelength or decreases only slightly with wavelength.

Thus, in non-biological samples, both the refractive index and internal morphology determine how much backscattered light contributes to the OCT signal. Presence of multi-scattered light

Optics EXPRESS

may also affect the measurement of the axial resolution. On the other hand, the lateral resolution of the optical system is determined by the focusing optics and the operating wavelength, and can be approximated in the diffraction-limited case as [31,32]

$$r \approx \frac{\lambda_0}{2\, n \sin\theta} = \frac{\lambda_0}{2\, NA} \tag{2}$$

where n is the refractive index of the media, and θ is the half-angle of the focused beam, and $\mathrm{NA} = n \sin\theta$ is the numerical aperture. Here r should be interpreted as an approximate lateral resolution limit rather than physical beam diameter. The inset of Fig. 1 shows the dependence of estimated lateral resolution on the NA of the focusing optics for operation at 2 µm wavelength. The lateral resolution improves with increasing NA at the expense of the depth of focus (DOF), i.e., the axial range over which the beam remains tightly focused. For example, doubling NA improves the lateral resolution, while the DOF is reduced by approximately a factor of four. At 2 µm, diffraction-limited DOF is larger than at 1.3 µm for the same NA, although scattering media can still limit the useful imaging depth. Overall, Fig. 1 predicts that an axial resolution well below 10 µm can be obtained at 2 µm for practical refractive index ranges, provided that a source with an emission bandwidth >100 nm is available.

3. SLD fabrication and characterization

The SLD is based on an active region with two $Ga_{0.72}In_{0.28}Sb$/GaSb quantum wells (QWs) and has a lateral waveguide design with a J-shaped ridge waveguide (RWG) geometry. The design and fabrication details have been recently reported in Alam Bhuiyan *et. al.* 2025 [25], which can be visualized from Fig. 2(a)-(c) illustrating the active region's conduction band profile (E_c), device layout (top-view), and the cross-section. The right panel of Fig. 2(c) shows the cross-sectional schematic of the fabricated SLD device, while the left panel illustrates the corresponding layer structures, including SiN_x insulator, p-GaSb cap layer, cladding layers (n-cladding near the substrate and p-cladding near the cap layer), active region, p-metal contact, and GaSb substrate. In current experiments a 2 mm long SLD chip was used that has 5 µm wide RWG. Along the longitudinal direction the waveguide has a straight section with a length of ~1.05 mm while the remaining waveguide exhibits an Euler bend [33] geometry with a 7° curvature terminated at the facet. For suppressing the unwanted cavity reflections at the end facet of the waveguide an SiO_x/TiO_x antireflective (AR) coating was deposited with an estimated reflectivity of 0.5% at the curved front facet. Then, at the straight end of the waveguide a 90% high-reflective (HR) coating was deposited to enhance the ASE effect and hence the output power and the degree of coherence. At this point, it is important to note that the increase in stimulated emission comes with a decrease of the optical bandwidth and generally less smooth spectra owing to gain saturation effects. The fabricated SLD chips were mounted in a "p-side-up" configuration while the metallized n-side was bonded to the sub-mount using conductive epoxy-glue. The assembled chip was then integrated into a standard 14–pin butterfly package by Superlum Diode Ltd, with the output facet focused into a Corning SMF-28 single-mode fiber (FC/APC connector). A schematic illustration of the packaged butterfly module is shown as an inset in Fig. 2(d).

The SLD was driven in continuous-wave (CW) mode at room temperature (RT) and the corresponding light-current (*L-I*) and voltage-current (*V-I*) dependence of the packaged device are shown in Fig. 2(d). The output characteristics reveal the onset of ASE at a current of ~100 mA, beyond which the power increases linearly with the injection current. The maximum power measured at the fiber end was approximately 19.5 mW at a current of 1 A. For free-space operation, the same device has demonstrated a maximum power of ~40 mW at a current of 1 A, suggesting an overall fiber coupling efficiency of ~49%, a clear indication of the excellent beam quality provided by the SLD. The power saturation observed near 900–1000 mA is primarily due to saturation in gain as well as thermal rollover of the SLD device, which may be mitigated for a

Optics EXPRESS

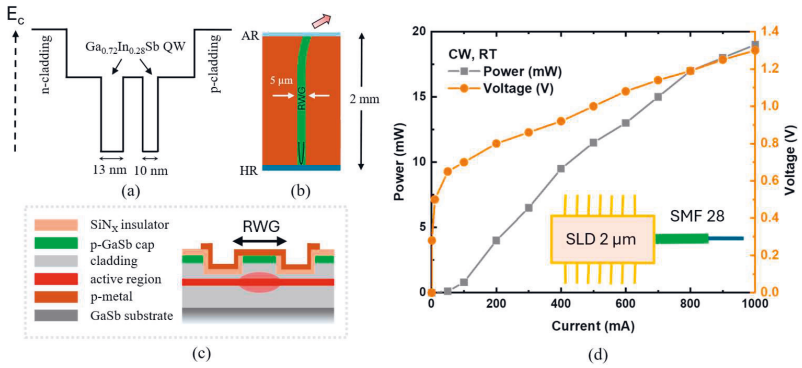


Fig. 2. (a) Conduction band edge profile (E_c) of the active region comprising two $Ga_{0.72}In_{0.28}Sb$/GaSb QWs embedded within AlGaAsSb barrier layers. (b) Top-view schematic of J-shaped RWG-based SLD device geometry, showing output light signal collected along the arrow near the AR-coated facet. (c) Cross-sectional schematic of the fabricated RWG structure illustrating the epi-structure and ridge formation. (d) *L-I,* and *V-I* characteristics of the pigtailed 14-pin butterfly SLD module driven under CW mode in RT. Inset shows a schematic illustration of the packaged SLD module configuration.

p-side-down mounting temperature. Furthermore, the *V–I* characteristics of the SLD measured in CW mode at room temperature reveal an accessible maximum operation voltage of ~1.3 V, which makes a strong case for simplicity of driving such devices [25,34,35].

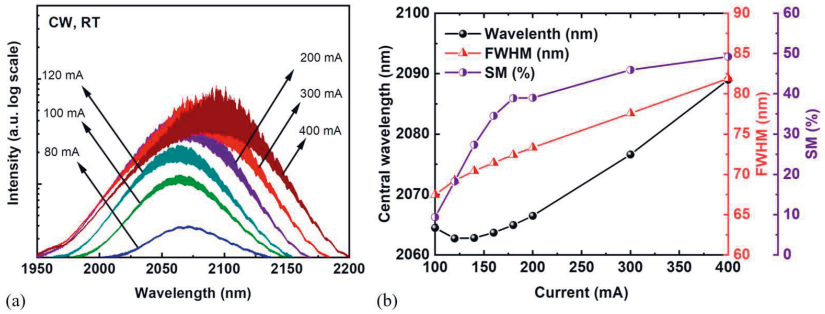


Fig. 3. (a) ASE spectra of the SLD measured in the free space at different injection current (0-400 mA) under CW mode in RT. (b) Evolution of the central emission wavelength (circle), FWHM bandwidth (half-filled tringle) and spectral modulation SM (%) (half-filled circle) as a function of drive current.

The emission spectrum was measured using Yokogawa AQ6375 optical spectrum analyzer (OSA) with a resolution of 0.1 nm, with the output coupled via an SM1950 single-mode fiber patch cord. Figure 3(a) shows the measured spectrum at different currents (80–400 mA) demonstrating a broad ASE spectrum for RT operation. Figure 3(b) reveals the evolution of the center wavelength from ~2065nm at lower currents (100 mA) to ~2090nm at higher currents (400 mA), accompanied by a bandwidth (FWHM) increase from ~65 nm to ~83 nm. At the same time the output power changed from ~1 mW to ~10 mW. The measured spectral modulation (SM) is < 20% when driven

Optics EXPRESS

up to until 150 mA, however, higher injection yields higher amplification in the double pass gain geometry resulting in increased SM of ~50% at 400 mA. To this end, 400 mA is set as a practical operational current limit in order to avoid excess heating as well as cavity oscillations due to lasing events.

The best axial resolution in air for the broadest spectra (corresponding to a drive current of ~400 mA) was estimated to be 23 µm. The estimated axial resolution for a semi-dense media (i.e., n=1.5) decreases to ~19 µm and down to ~15 µm when the SLD was driven at 100 mA and 400 mA, respectively. Similarly, for more dense media (i.e., n=3) the resolution can be lowered to ~7.7 µm. This can provide an excellent OCT resolution, especially in semi-/non-transparent scattering materials such as polymer layers (i.e., paints), dielectric stacks, adhesives, or ceramic composites. For applications requiring even higher resolution, the SLD's emission bandwidth could be further engineered (e.g., via SLD cavity geometry) and the SM can be reduced by optimized AR/HR coatings.

4. TD-OCT setup and imaging

4.1. Interferometer setup

Figure 4 shows the 2 µm fiber-based TD-OCT employing a Michelson interferometer configuration. The system utilizes a Thorlabs 50:50 wideband SMF-28 fiber optic coupler (TW2000R5A2B), built for broadband transmission around 2 µm (2000 ± 200 nm) and terminated with FC/APC connectors. The output of the 2 µm SLD butterfly module injects ASE into one input port of the fiber coupler (FC#1), and the signal splits into two parts: one to the reference arm and the other to the sample arm. In the sample arm, the light is first collimated towards the scanner via a Thorlabs's RC04APC-P01 protective silver reflective collimator (450 nm - 20 µm, focal length = 15 mm). The XY galvo scanners, deflects the beam towards a broadband AR coated (1.65 - 3.0 µm) CaF_2 focusing lens L4 (LA5315-D - Ø1/2", plano-convex) with a focal length of 20 mm, which focuses the light into the sample. The galvos are positioned in the conjugate plane with the sample. In the reference arm, the 20 mm CaF_2 lens L1 collimates the beam, and using the same configuration the light is injected back (through L2) into the fiber. A reference arm translation stage (TSR), movable along Z-axis, in the reference arm path is used with the lens L1 to adjust the optical path difference and axial positioning. The TSR was moved by a distance ΔZ, in order to generate the B-scans. The light from reference and sample arm is recombined using another 50:50 fiber coupler (FC#2). The two-coupler TD-OCT configuration (with FC#1 and FC#2) enables balance detection. At the output of FC#2, the ac signal exhibits a "pi" phase difference. In this way, a balance detection configuration doubles the interference signal and reduces the bias and the excess photon noise, enabling better sensitivities [36].

The balanced outputs from the FC#2 are then coupled into the custom-built balanced photodetector (BPD) using two identical Hamamastu G12183-010 K extended InGaAs PIN photodiodes, with 1 A/W photosensitivity from 1.7 µm to 2.4 µm. By using the balanced detection scheme, the interferometric signal is enhanced by reducing common-mode intensity noise between reference and sample arm [37]. The signal is acquired with a 14-bit digitizer (NI PCI-6132, max 2.5 MS/s per channel) and demodulated to retrieve the fringe envelope.

4.2. Coherence measurement

Figure 5 shows coherence measurement using the Michelson interferometer setup (shown in Fig. 4), when the 2 µm SLD source is driven at ~150 mA, corresponds to ~2.5 mW output power. Although the power would be larger at increased currents, for the best trade-off between bandwidth and axial resolution the 150 mA drive current is chosen for device characterization. Coherence measurement is a critical step in assessing the suitability of a light source for OCT. Unlike total output power or central wavelength, which only describe the gross emission characteristics, the

Optics EXPRESS

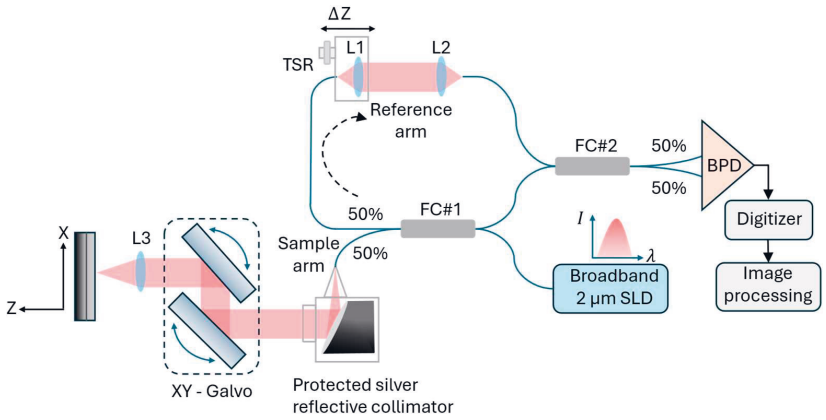


Fig. 4. Schematic of the time domain Optical Coherence Tomography (TD-OCT) system. Collimating lenses L1–L3 have identical focal lengths of 20 mm, and the protected silver reflective collimator has a focal length of 15 mm. A reference arm translation stage (TSR) is used in the reference arm path.

coherence function directly estimates the axial resolution and image quality achievable in the TD-OCT scheme. Measuring the interferometric coherence length of the SLD therefore provides an experimental validation of its performance as a low-coherence source at 2 µm. Scanning the reference arm produces a central fringe packet around the zero-path difference position, while the sample arm contains a stable fixed mirror. The envelope of this interferogram reveals the finite coherence of the source. The measured FWHM of the envelope is approximately 0.6 mm, corresponding to an axial resolution of about 300 µm in air after accounting for the two-way propagation in the interferometer. This experimental resolution is lower than the ideal resolution predicted from the optical bandwidth alone, indicating deviations from an ideal smooth source spectrum at the interferometer input. In particular, residual cavity effects within the SLD structure and losses due to packaging optics have detrimental influence on spectral modulation and partial bandwidth reduction, which together broaden the coherence envelope and introduce secondary peaks in the axial PSF. Despite these effects, the measurement demonstrates the essential low-coherence operation of the GaSb-based SLD at 2 µm and confirms its suitability as a practical OCT source, where the achievable axial resolution will depend primarily on spectrum shaping and fiber-coupling.

4.3. Setup optimization

To optimize the scanning efficiency of the interferometer, *en-face* images of a structured test object (a British five-pence coin) were initially obtained, as shown in Fig. 6. The measurement was conducted utilizing the galvo scanners at a fixed optical path difference as adjusted by actuating the TSR. The scanners were driven with a 250 or 500 Hz triangular signal for scanning along X axis (fast scanning direction) and with a 1 Hz or 2 Hz sawtooth signal along Y axis (slow scanning direction). To evaluate the performance of the configured system, confocal and OCT images were taken from identical targets using custom-built 100 kHz rectifier. Without rectification, both confocal and OCT images exhibit strong modulation artefacts and periodic distortions, which obscure fine details of the coin's engraved pattern. With rectification applied, these artefacts

Optics EXPRESS

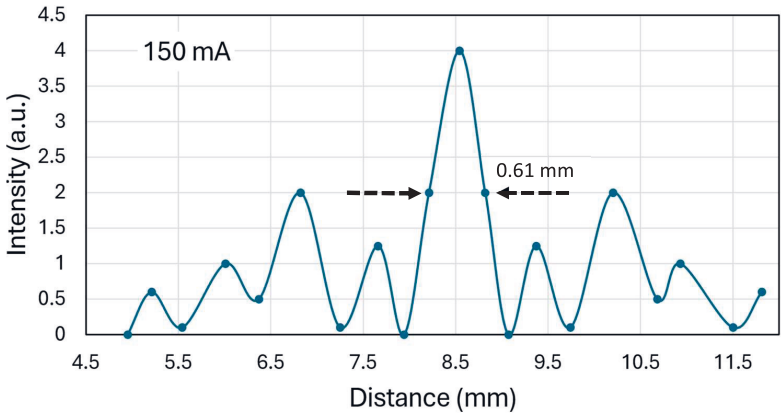


Fig. 5. Coherence measurements obtained from the interferometer setup with the SLD biased at 150 mA with the thermoelectric cooler maintaining the device at 20°C (RT).

are suppressed, yielding smoother backgrounds and sharper outlines of the engraved features, confirming improved lateral fidelity of the scanning system.

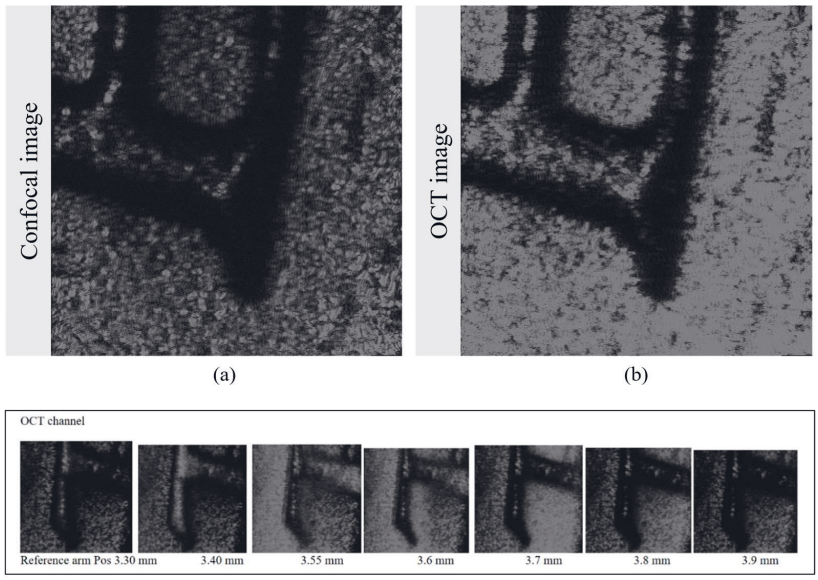


Fig. 6. *En-face* imaging of a five pence British coin by using (a) confocal and (b) OCT modalities. Each image covers an area of 2 mm x 2 mm. (c) *En-face* OCT images from OCT channels at various reference arm positions.

Optics EXPRESS

The confocal image in Fig. 6(a) represents an *en-face* reflection map at the objective's focal plane, where the spatial filtering of the single-mode fiber acts as a pinhole to exclude out-of-focus light. Conversely, the OCT image in Fig. 6(b) is acquired by low-coherence interferometry, wherein the short coherence length of the GaSb SLD facilitates coherence gating: solely backscattered photons that return within the coherence length of the reference beam contribute to the interference signal. This process allows the selective detection of reflections from certain depths, generating cross-sectional pictures with micrometer-scale axial resolution. To ensure a controlled performance comparison, both the OCT and confocal imaging data were acquired using the same optical setup. Consequently, optical parameters such as the numerical aperture (~0.05) and lateral resolution (~26 µm) are identical for both modalities, thereby minimizing hardware-related differences. The primary methodological distinction lies in the signal processing used to form the images. To generate the confocal image from the same system, depth discrimination was removed by extracting the envelope of the interference pattern and integrating the signal across all depths. The comparison of confocal and OCT images confirms optical alignment and lateral resolution, while highlighting OCT's distinct advantage in revealing subsurface microstructures that conventional confocal imaging cannot resolve. Figure 6(c) illustrates the *en-face* OCT images for various reference arm positions, showing how the system can reconstruct topography of the coin surface.

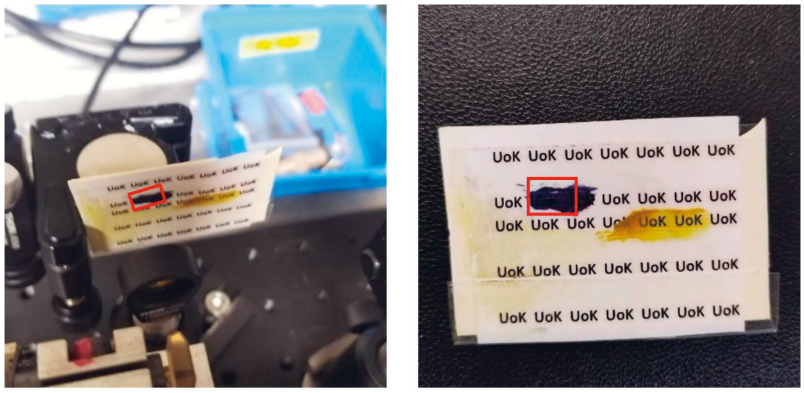
4.4. TD-OCT imaging

As a structured test object, we used a printed paper card (see Fig. 7) with the repeated text "UoK," onto which a thin paint coating was applied. The printed pattern provided a high-contrast lateral reference, while the paint introduced scattering and absorption representative of real-world non-biological coatings. The sample was mounted in the dedicated sample arm of the TD-OCT interferometer, positioned on a translation stage to allow controlled alignment and focusing. The probing beam from the fiber collimator was directed onto the card surface (marked with red rectangle) through the microscope objective, ensuring that both the printed features and the overlaying paint were within the optical field of view. This configuration enabled simultaneous evaluation of the system's lateral resolution by imaging the text and its axial sectioning capability by resolving subsurface structures beneath the paint. By combining a structured target with an artificial scattering layer or coatings, the setup offered a controlled yet realistic scenario to benchmark OCT performance before testing on more complex materials.

The sample, as described above, is a printed card ("UoK" pattern) overlaid with a thin paint film (Edding 750 permanent marker) and imaged with a fiber-based TD-OCT using a broadband GaSb SLD centered at ~2.05 µm. *En-face* OCT slices in Fig. 8(a) and (b) were obtained by fixing reference delay at two different depths and performing lateral raster-scanning. Figure 8(a) corresponds to a plane within paint layer, while Fig. 8(b) corresponds to a plane near the printed text (ink-substrate interface). In Fig. 8(b), the buried printed text appears as bright, high-contrast features against the white paper substrate background due to local refractive-index and absorption differences at the ink–substrate interface. The mottled texture and spatial non-uniformity along the letter strokes arise from multiple scattering within the pigment coating and small-scale surface roughness introduced during paint application. The 2 µm SLD source reduces scattering relative to shorter near-infrared bands, resulting in improved penetration through the paint coating and enabling clear visualization of the buried print.

Figure 8(c) is a representative B-scan acquired across the same region (see red dashed line in Fig. 8(b)) by assembling a volume of 200 *en-face* images recorded at successive depths. Axial scanning of the sample is performed using a translation stage with corresponding adjustment of the reference arm. Two dominant interfaces are evident – a strong reflection from the air/paint surfaces and a deeper band from the paint/substrate boundary. Lateral variations in the spacing between these interfaces indicate non-uniform paint thickness across the scanned area. Below the

Optics EXPRESS



(a) (b)

Fig. 7. Photographs of the test sample used for OCT imaging. (a) A printed card with repeated "UoK" text partially covered by a thin paint layer and positioned in the sample arm of the interferometer. (b) Front-view photograph of the same sample card. The red rectangles in both panels indicate the OCT scanning area.

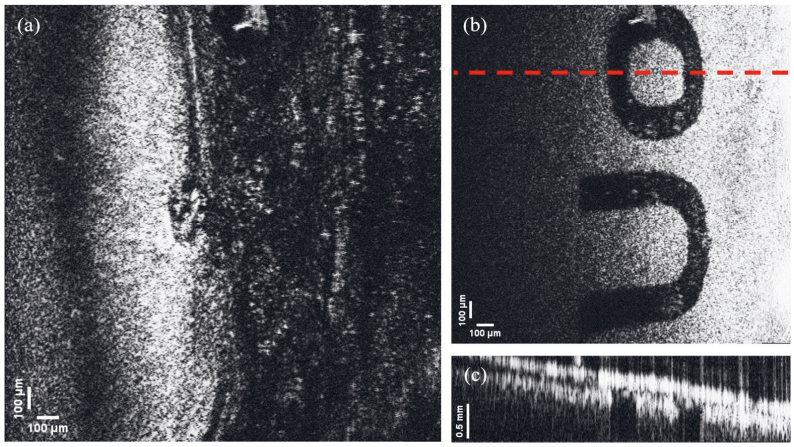


Fig. 8. Imaging of "text under paint" with the fiber-based TD-OCT using a ~2.05 µm GaSb SLD source. *En-face* slices at (a) a plane within the paint coating and (b) a plane near the buried print, revealing the "UoK" lettering as bright features beneath the paint (see Visualization 1). (c) Corresponding B-scan (along the red dashed line in (b)) reveals the air/paint surface and the paint/substrate interface; their varying separation indicates non-uniform paint thickness. Coherence gating cleanly separates surface reflections from the subsurface print.

Optics EXPRESS

surface, signal amplitude decays with depth due to combined scattering and material absorption, while shadowing beneath the inked regions further attenuates the backscattered signals. Taken together, the *en-face* slices and reconstructed B-scan demonstrate the complementary strengths of TD-OCT at 2 µm – coherence gating isolates reflections from a selected depth to reveal the buried text, while the B-scan provides a geometric readout of the layered structure (surface, paint coating, and substrate) and associated thickness variations.

5. Discussion

The TD-OCT experiment revealed a discrepancy between the axial resolution anticipated from the source spectrum and that recorded from the coherence envelope at drive currents under 150 mA. The bandwidth-derived estimate assumes a broad spectrum at the interferometer input, whereas the spectrum delivered by the fiber-coupled SLD module exhibits a reduced effective bandwidth together with spectral modulation. These spectral non-idealities broaden the measured coherence envelope relative to the Gaussian-limited case and introduce weak side-lobe structure in the axial PSF [38,39], which limits the experimentally achievable axial resolution indicating the axial performance depends on the spectral smoothness in addition to the spectral width. In the present measurements, the ripple depth is approximately 20% at drive current up to 150 mA and increases to nearly 50% at 400 mA; thereby, the axial resolution does not scale directly with the increased FWHM bandwidth at higher current, despite the broader emission spectrum.

Conventional OCT systems operating in the 1.3–1.5 µm spectral range typically achieve axial resolutions of ~5–15 µm [37,40], while ultrahigh-resolution techniques, such as optical coherence microscopy, can reach a few micrometers or below [41]. From theoretical perspective, maintaining comparable axial resolution at longer wavelength requires proportionally broader optical bandwidth; for example, doubling the central wavelength requires approximately four times larger bandwidth. In comparison, the present 2 µm TD-OCT system provides lower axial resolution but targets a different operating regime, where longer-wavelengths OCT offers advantages for deeper probing of scattering or optically dense materials, which is the primary motivation of this work. Moreover, unlike the well-established 1.3–1.5 µm SLD technology, the GaSb-based 2 µm SLD platform involves a more challenging trade-off between bandwidth, continuous-wave output power, and spectral ripple suppression, which currently limits the effective coherence performance. Further optimization toward broader and spectrally smoother emission is therefore expected to improve the achievable axial resolution.

Future enhancements may be achieved through the utilization of mid-infrared-optimized single-mode fibers (such as fluoride or chalcogenide fibers) in the interferometer's fiber arms, the implementation of optimized anti-reflection coatings at the SLD facets to decrease cavity effects, the incorporation of dispersion compensating elements within the interferometer, or the application of active alignment techniques to further reduce coupling losses.

Regarding the OCT imaging, for a standard paint film with a refractive index of around 1.5–1.6, an air-calibrated resolution of ~29 µm (100 mA, 65 nm FWHM) corresponds to ~19 µm within the material, with further possibility for enhancement to ~15 µm for the wider 83 nm spectrum (400 mA). Despite the fact that these ideal values were not fully attained under the present fiber-coupled implementation at drive currents below 150 mA, the depth-resolved imaging results nonetheless demonstrate the coherence gating operation at 2 µm, where reduced scattering supports penetration through paint coatings and enables reliable distinction between surface and subsurface interfaces for thickness mapping.

With this understanding, future work will aim imaging advanced artificial samples (e.g. etched glass or microfabricated features under a 2 µm-transparent medium) which would be a valuable validation of the system's 3D imaging performance. In addition to non-destructive testing applications, operation near 2 µm may also be relevant for the investigation of biomaterials under *ex vivo* conditions. While strong water absorption at this wavelength limits *in vivo*

Optics EXPRESS

imaging depth in biological tissues, *ex vivo* samples or low-water-content biomaterials can still benefit from reduced scattering at longer wavelengths. This may enable improved subsurface visualization in applications such as tissue engineering, processed biological samples, or biomaterial characterization.

Although Fourier-domain OCT (FD-OCT) techniques, including SD- and swept-source (SS) implementations, offer higher sensitivity and imaging speed than TD- modality, the present work intentionally employs a TD-OCT configuration as a proof-of-principle platform to directly evaluate the coherence properties of the 2 µm GaSb-based SLD, rather than to push scanning speed. Implementation of FD-OCT at this wavelength remains challenging due to the limited availability of high-performance detector arrays beyond 1.7 µm, where extended-InGaAs sensors typically exhibit higher noise and reduced sensitivity. Additionally, operation of such SLD device in a SS- configuration would require more research into producing an improved device, with larger gain in one optical path and reduced facet reflectivity. Nevertheless, the demonstrated GaSb-based gain platform is compatible with external-cavity or amplifier-based architectures and could enable future SS-OCT systems operating in this spectral region. Once TD-OCT operation has been demonstrated at 2 µm, it establishes the feasibility of low-coherence interferometric detection at this wavelength and supports the expectation that spectrometer-based OCT implementations can also be realized, provided suitable detector and spectrometer technologies are available.

6. Conclusion

A TD-OCT system at 2 µm regime was demonstrated using broadband ASE from a compact GaSb-based SLD. To the best of our knowledge, this represents the first demonstration of a fiber-based TD-OCT system operating at 2 µm exploiting GaSb SLDs. The results highlight the viability of GaSb SLDs as practical sources for such compact OCT systems in the mid-IR region, with potential for cost-effective implementation through wafer-scale semiconductor fabrication and simplified optical architectures. Operation at this wavelength enabled probing of a scattering and absorbing paint coatings compared to shorter-wavelength OCT. More broadly, such 2 µm OCT configuration shows promise for extending penetration depth in other low-water-content, strongly scattering materials. The broadband ASE spectrum supported axial resolutions of approximately ~29 µm in air, while broader coherence envelopes on the order of 300 µm was observed under the present fiber-coupled implementation, sufficient to reliably resolve layered subsurface structures in scattering layer. However, the current system performance is limited by spectral ripples and effective bandwidth reduction introduced by the fiber-coupled packaging, which broadens the coherence envelope relative to the theoretical limit. In addition, the thermal and spectral stability of the source under CW operation ensured repeatability, an important requirement for industrial and scientific applications. With further system-level improvements, for example related to the spectral ripple reduction and use of mid-IR fibers, the GaSb SLDs can become a good candidate in the armamentarium of optical source to serve the OCT community and expand the role of OCT beyond biomedical imaging to precision metrology and materials diagnostics.

Funding. Horizon 2020 Framework Programme project NETLAS (860807); HORIZON EUROPE Framework Program project PhotonMed (101139777-2); Research Council of Finland (320168); Business Finland (8294/31/2023); Ministerio de Ciencia, Innovación y Universidades (BG24/00089); NIHR Moorfields Biomedical Research Centre (BRC4-05-RB413-302).

Acknowledgment. The authors acknowledge support from the European Commission under the Horizon 2020 program through the project Next Generation of Tunable Lasers for Optical Coherence Tomography (NETLAS, Grant Agreement No. 860807, H2020-MSCA-ITN-2019). Additional support was provided by the HORIZON EUROPE Framework Program project PhotonMed (Grant Agreement No. 101139777-2, HORIZON-KDT-JU-2023-2-RIA), Business Finland (8294/31/2023) and the Research Council of Finland Flagship Programme PREIN (Decision No. 320168). Alejandro Martinez Jimenez also acknowledges support for a Beatriz Galindo junior fellowship (BG24/00089) from the Spanish Ministry of Science, Innovation and Universities and from the University of Castilla La-Mancha.

Optics EXPRESS

Ramona Cernat, Adrian Fernandez Uceda and Adrian Podoleanu were supported by NIHR MOORFIELDS BRC, BRC3 and in part by NIHR under Grant BRC4-05-RB413-302, at UCL Institute of Ophthalmology and Moorfields Eye Hospital. The authors wish to thank Alexander Chamorovskiy and SUPERLUM (https://superlum.ie/) for collaborating in making fiber coupled butterfly module. The authors also wish to thank Pete Verrall for making custom balanced photodetector for OCT setup.

Disclosures. The authors declare no conflicts of interest.

Data availability. Data underlying the results presented in this paper are not publicly available at this time but may be obtained from the authors upon reasonable request.

References

1. D. Huang, E. A. Swanson, C. P. Lin, *et al.*, "Optical Coherence Tomography," Science **254**(5035), 1178–1181 (1991).
2. A. Alex, B. Považay, B. Hofer, *et al.*, "Multispectral in vivo three-dimensional optical coherence tomography of human skin," J. Biomed. Opt. **15**(2), 026025 (2010).
3. W. Drexler and J. Fujimoto, "State-of-the-art retinal optical coherence tomography," Prog. Retinal Eye Res. **27**(1), 45–88 (2008).
4. M.-Y. Fu, Z.-H. Yin, X.-Y. Yao, *et al.*, "The Progress of Optical Coherence Tomography in Industry Applications," Adv Devices Instrum. **5**, 0053 (2024).
5. S. L. Jacques, "Optical properties of biological tissues: a review," Phys. Med. Biol. **58**(11), R37–R61 (2013).
6. B. E. Bouma, J. F. de Boer, D. Huang, *et al.*, "Optical coherence tomography," Nature Reviews Methods Primers **2**(1), 79 (2022).
7. J. Gocławski, E. Korzeniewska, J. Sekulska-Nalewajko, *et al.*, "Extraction of the Polyurethane Layer in Textile Composites for Textronics Applications Using Optical Coherence Tomography," Polymers **10**(5), 469 (2018).
8. A. Nazari, A. Sadr, M. A. Saghiri, *et al.*, "Non-destructive characterization of voids in six flowable composites using swept-source optical coherence tomography," Dent. Mater. **29**(3), 278–286 (2013).
9. P. Ekberg, R. Su, E. W. Chang, *et al.*, "Fast and accurate metrology of multi-layered ceramic materials by an automated boundary detection algorithm developed for optical coherence tomography data," J. Opt. Soc. Am. A **31**(2), 217 (2014).
10. M. Wolfgang, A. Peter, P. Wahl, *et al.*, "At-line validation of optical coherence tomography as in-line/at-line coating thickness measurement method," Int. J. Pharm. **572**, 118766 (2019).
11. A. I. Koponen and S. Haavisto, "Analysis of Industry-Related Flows by Optical Coherence Tomography—A Review," KONA **37**(0), 42–63 (2020).
12. M. J. Marques, R. Green, R. King, *et al.*, "Sub-surface characterisation of latest-generation identification documents using optical coherence tomography," Sci. Justice **61**(2), 119–129 (2021).
13. C. S. Cheung, J. M. O. Daniel, M. Tokurakawa, *et al.*, "Optical coherence tomography in the 2-µm wavelength regime for paint and other high opacity materials," Opt. Lett. **39**(22), 6509 (2014).
14. S. Skruszewicz, S. Fuchs, J. J. Abel, *et al.*, "Coherence tomography with broad bandwidth extreme ultraviolet and soft X-ray radiation," Appl. Phys. B **127**(4), 55 (2021).
15. A. J. Arikkatt, Ł. Węgrzyński, A. Bartnik, *et al.*, "Laboratory system for optical coherence tomography (OCT) using a laser plasma source of soft x-rays and extreme ultraviolet and focusing ellipsoidal optics," Opt. Express **30**(8), 13491–13509 (2022).
16. H. Liang, R. Lange, B. Peric, *et al.*, "Optimum spectral window for imaging of art with optical coherence tomography," Appl. Phys. B **111**(4), 589–602 (2013).
17. M. Read, C. S. Cheung, H. Liang, *et al.*, "A Non-invasive Investigation of Egyptian Faience Using Long Wavelength Optical Coherence Tomography (OCT) at 2 µm," Stud. Conserv. **67**(3), 168–175 (2022).
18. T. H. Ko, D. C. Adler, J. G. Fujimoto, *et al.*, "Ultrahigh resolution optical coherence tomography imaging with a broadband superluminescent diode light source," Opt. Express **12**(10), 2112 (2004).
19. V. R. Shidlovski, "Superluminescent Diode Light Sources for OCT," In: W. Drexler and J. G. Fujimoto, (eds.) *Optical Coherence Tomography*. pp. 505–526. Springer International Publishing, Cham (2015).
20. H. Lu, O. Alkhazragi, Y. Wang, *et al.*, "Low-coherence semiconductor light sources: devices and applications," npj Nanophoton. **1**(1), 9 (2024).
21. G. A. Alphonse, "Design of high-power superluminescent diodes with low spectral modulation," Presented at the Proc.SPIE April 4648, 125–138 (2002).
22. A. Vizbaras, E. Dvinelis, M. Greibus, *et al.*, "High-performance single-spatial mode GaSb type-I laser diodes around 2.1 µm," Presented at the SPIE OPTO December 18 (2013).
23. K. Vizbaras, E. Dvinelis, I. Šimonytė, *et al.*, "High power continuous-wave GaSb-based superluminescent diodes as gain chips for widely tunable laser spectroscopy in the 1.95–2.45 µm wavelength range," Appl. Phys. Lett. **107**(1), 011103 (2015).
24. N. Zia, J. Viheriälä, E. Koivusalo, *et al.*, "High-power single mode GaSb-based 2 µm superluminescent diode with double-pass gain," Appl. Phys. Lett. **115**(23), 231106 (2019).
25. I. K. Alam Bhuiyan, J. Hilska, M. Peil, *et al.*, "Broadband continuous-wave GaSb-based superluminescent diodes emitting at 2.1 µm," AIP Adv. **15**(8), 085015 (2025).

Optics EXPRESS

26. S. Ojanen, J. Viheriälä, N. Zia, *et al.*, "Discretely Tunable (2594, 2629, 2670 nm) GaSb/Si3N4 Hybrid Laser for Multiwavelength Spectroscopy," Laser Photonics Rev. **17**(12), 2300492 (2023).
27. S. Ojanen, J. Viheriälä, N. Zia, *et al.*, "Widely Tunable (2.47–2.64 µm) Hybrid Laser Based on GaSb/GaInAsSb Quantum-Wells and a Low-Loss Si3N4 Photonic Integrated Circuit," Laser Photonics Rev. **17**(7), 2201028 (2023).
28. J. M. Schmitt, "Optical coherence tomography (OCT): a review," IEEE J. Select. Topics Quantum Electron. **5**(4), 1205–1215 (1999).
29. J. G. Fujimoto, C. Pitris, S. A. Boppart, *et al.*, "Optical Coherence Tomography: An Emerging Technology for Biomedical Imaging and Optical Biopsy," Neoplasia **2**(1-2), 9–25 (2000).
30. P. H. Tomlins and R. K. Wang, "Theory, developments and applications of optical coherence tomography," J. Phys. D: Appl. Phys. **38**(15), 2519–2535 (2005).
31. T. Latychevskaia, "Lateral and axial resolution criteria in incoherent and coherent optics and holography, near- and far-field regimes," Appl. Opt. **58**(13), 3597–3603 (2019).
32. A. Hon, "The Relation of Aperture and Power in the Microscope," J. R. Microsc. Soc. **2**(3), 300–309 (1882).
33. M. Cherchi, S. Ylinen, M. Harjanne, *et al.*, "Dramatic size reduction of waveguide bends on a micron-scale silicon photonic platform," Opt. Express **21**(15), 17814–17823 (2013).
34. I. K. A. Bhuiyan, J. Hilska, M. Peil, *et al.*, "Broadband 2-µm superluminescent diodes with GaSb-based variable-thickness quantum wells," Appl. Phys. Lett. **127**(16), 163307 (2025).
35. I. K. A. Bhuiyan, J. Hilska, M. Peil, *et al.*, "Design of broadband optical gain in GaSb-based heterostructures with asymmetric quantum wells," Opt. Express **33**(26), 54154–54165 (2025).
36. A. G. Podoleanu, "Unbalanced versus balanced operation in an optical coherence tomography system," Appl. Opt. **39**(1), 173–182 (2000).
37. A. F. Fercher, W. Drexler, C. K. Hitzenberger, *et al.*, "Optical coherence tomography - principles and applications," Rep. Prog. Phys. **66**(2), 239–303 (2003).
38. R. Tripathi, N. Nassif, J. S. Nelson, *et al.*, "Spectral shaping for non-Gaussian source spectra in optical coherence tomography," Opt. Lett. **27**(6), 406–408 (2002).
39. D. L. Marks, P. S. Carney, and S. A. Boppart, "Adaptive spectral apodization for sidelobe reduction in optical coherence tomography images," J. Biomed. Opt. **9**(6), 1281–1287 (2004).
40. B. E. Bouma, L. E. Nelson, G. J. Tearney, *et al.*, "Optical coherence tomographic imaging of human tissue at 1.55 um and 1.8 um using Er- and Tm-doped fiber sources," J. Biomed. Opt. **3**(1), 76–79 (1998).
41. A. Cogliati, C. Canavesi, A. Hayes, *et al.*, "MEMS-based handheld scanning probe with pre-shaped input signals for distortion-free images in Gabor-domain optical coherence microscopy," Opt. Express **24**(12), 13365–13374 (2016).